RICE UNIVERSITY

HIGH LATITUDE FIELD ALIGNED CURRENTS

by

JANICE LEE KARTY

A THESIS SUBMITTED
IN PARTIAL FULFILLMENT OF THE
REQUIREMENTS FOR THE DEGREE

DOCTOR OF PHILOSOPHY

APPROVED, THESIS COMMITTEE:

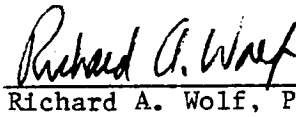

Richard A. Wolf, Professor of
Space Physics and Astronomy
and of Physics
Chairman

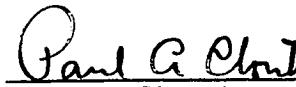

Paul A. Cloutier, Professor of
Space Physics and Astronomy

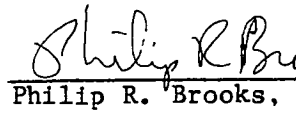

Philip R. Brooks, Professor of
Chemistry

HOUSTON, TEXAS

April, 1983

HIGH LATITUDE FIELD ALIGNED CURRENTS

by

Janice Lee Karty

ABSTRACT

Horizontal ionospheric conduction currents are driven by magnetic field-aligned currents generated in the Earth's magnetosphere. Traditional ideas about field-aligned currents imply that most of the higher latitude set of field-aligned (region-1 Birkeland) current flows on field lines that connect to antisunward-flowing magnetospheric plasma. This conclusion disagrees with recent satellite data, and that disagreement provides a major motivation for this thesis.

This research includes a stability analysis that is based on current conservation, which implies that field-aligned current is balanced by the divergence of ionospheric current. This stability analysis demonstrates that there may be a sector, within the plasma sheet in the nightside magnetosphere, where plasma pressures are reduced relative to the surrounding regions.

In order to simulate this depleted region, several "computer experiments" have been performed, enforcing gradients in plasma content at the tailward boundary of the calculation. These "com-

puter experiments" use an adapted form of the Rice Convection Model which has previously been used to calculate Birkeland currents (as well as other magnetospheric currents) in the inner magnetosphere by utilizing time dependent data from specific geophysical events. The present work extends the model further out in the magnetosphere.

Results of these "computer experiments" applied to the 19 September 1976, substorm event show that it is possible to generate high latitude magnetic field-aligned currents (region-1) connecting to regions of sunward plasma motion in the magnetosphere, indicating a significant departure from classical notions. The new model agrees better with observations than the earlier Rice model, with regard to the latitudinal distribution of the lower latitude (region-2 Birkeland) field-aligned currents, with a general increase in latitudinal extent. The peak magnitudes of the generated currents relative to region-2 current strength are ~50% on the dusk side, and ~100% on the dawn side. However, approximately 50% of the current may exist outside the modeling region. This generating mechanism may very well be the most important region-1 current source in the regions of ~18:00 LT to 21:00 LT and ~3:00 LT to 6:00 LT which causes flow of region-1 current on sunward convecting flux tubes.

ACKNOWLEDGMENTS

I am grateful to my thesis advisor, Professor Richard A. Wolf, for his careful guidance during my years as a graduate student. He made many helpful comments on the manuscript.

My sincere thanks go to Dr. Robert W. Spiro who assisted with the computer plotting, and to Dr. Hannes Voigt for the use of his magnetic field models.

I would like also to acknowledge the help of Jerry P. Mays for his skill at typing the dissertation. The drafting expertise of Chris Dunning is also appreciated. Her talents are evident in several of the figures.

The help of my husband's parents, Emanuel and Helene Baskir, is also acknowledged here. They have provided nourishment and interesting conversations at weekend dinners at their home.

Many thanks also go to my husband, Bruce Matathias Baskir, who weathered Internal Medicine and Surgery rotations and a wife preparing a doctoral thesis at the same time. He has been a genuine comfort as well as a patient listener throughout the final preparation of this thesis.

Lastly, I thank my parents, Frances and Daniel Karty. My mom is now pursuing her own doctoral studies. She taught me to value the acquisition of knowledge, and to logically approach a problem, investigating all the consequences. This thesis is dedicated to my parents, whose love and constant encouragement made the completion of this thesis project a reality.

"...and a time to every purpose under the heaven."

TABLE OF CONTENTS

I. INTRODUCTION

A. Background

1) The Magnetosphere and Magnetospheric Convection

The magnetosphere is an area in space which surrounds the Earth where the geomagnetic field dominates the physics of various phenomena. In the last fifty years, much progress has been made in understanding magnetospheric processes and a cohesive picture has emerged. Figure 1 shows a schematic view of the Earth's magnetosphere, illustrating major regions. A very brief discussion of some of these features provides a necessary short introduction to magnetospheric physics.

The bow shock (see Figure 1) is formed as a result of the supersonic solar wind encountering the magnetosphere. Inside the bow shock there is turbulent magnetosheath plasma, which is bounded on the earthside by the outermost boundary of the magnetosphere (i.e., the magnetopause). The plasmasphere is a region of comparatively dense plasma which is contained in the near Earth "dipolar" region of the magnetosphere. The corotating plasma in this region is apparently of ionospheric origin. The plasma sheet is outside the plasmapause (i.e., the outermost boundary of the plasmasphere), and is a region which is mainly distinguished by the average particle energy $\gtrsim$ 1 keV. The plasma sheet (see Figure 1) includes the neutral sheet, which divides the magnetotail into two regions, above which the field is mostly sunward (in an ideal-

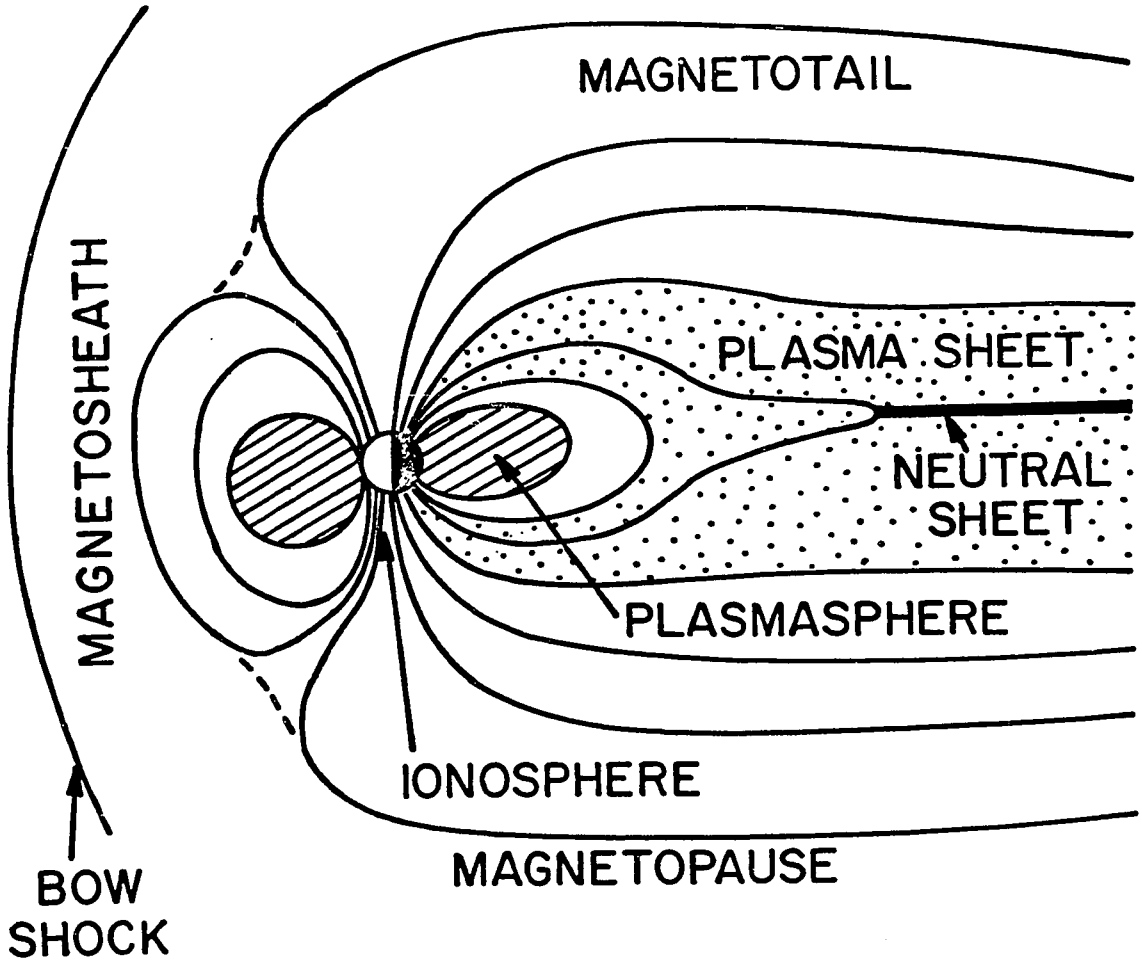

Figure 1. The present concept of the magnetosphere (shown here in a noon-midnight meridian plane view). Adapted from NASA 'OPEN' publication.

ized view) and below which the field is, for the most part, oppositely directed.

Axford and Hines (1961) and Dungey (1961) provided the essential physical idea of magnetospheric convection, namely, the idea of a systematic circulation of plasma through the magnetosphere. The general magnetospheric convection pattern is also discussed by Cole (1961) and Axford (1969). The "open" model of the magnetosphere, which is depicted schematically in Figure 2, is adapted from the picture originally proposed by Dungey (1961). In the "open" model, field lines (see region II of Figure 2) from the Earth's northern and southern polar caps eventually thread into regions outside the magnetosphere. That is, some magnetic field lines inside the magnetosphere can be directly connected with the interplanetary magnetic field (IMF). Field lines that extend to large geocentric distance map to the high latitude ionosphere. In Figure 2, the large arrow in the sunward portion of region I is a representation of the flow velocity of highly conducting solar wind plasma. With this high conductivity, the electric field in a reference frame moving with the plasma should be virtually zero. Taking the solar wind velocity to be $\underset{\sim}{v}_S$ (with respect to the earth's magnetosphere), and referring to the IMF as $\underset{\sim}{B}_I$, then $\underset{\sim}{E}_I = -\underset{\sim}{v}_S \times \underset{\sim}{B}_I$, where $|\underset{\sim}{E}_I|$ is the magnitude of an electric field of interplanetary origin. This electric field can be communicated to the magnetosphere via field lines connected with those in interplanetary space. Thus, there is a "dawn to dusk" electric field in the magnetosphere which is driven by the solar

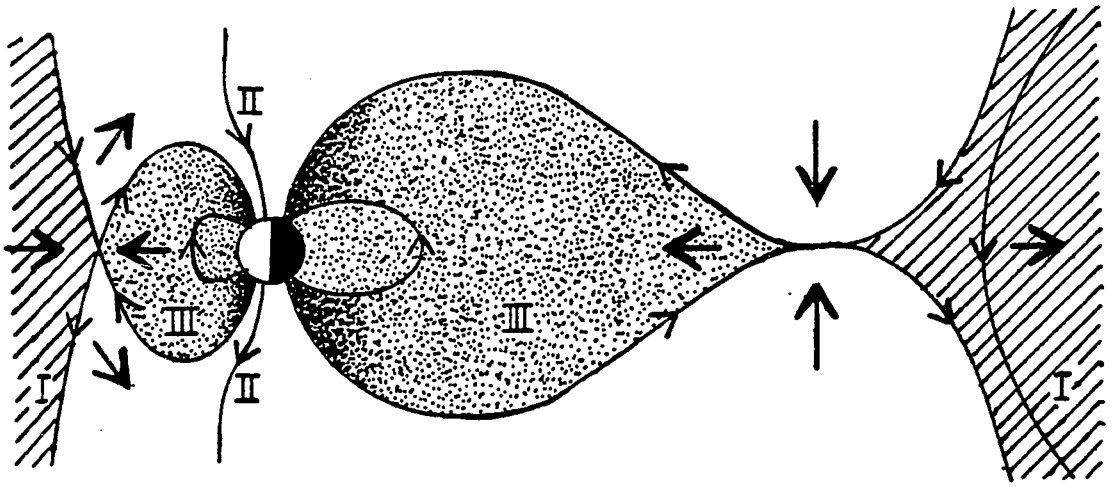

Figure 2. Topology of the magnetic field and direction of the plasma flow in the noon-midnight section of the open magnetosphere, according to Dungey (1961). The small arrows indicate the direction of magnetic field. Larger arrows indicate the direction of plasma flow. Within the closed field line region, the "domain" of auroral particles is heavily stippled. Adapted from Fig. 18 of Nishida (1978), and Fig. 61 of Rishbeth and Garriott (1969). This picture assumes southward IMF.

wind. The interaction of the dawn to dusk electric field ($\underset{\sim}{E}$) and the geomagnetic field ($\underset{\sim}{B}$) leads to plasma convection, with the velocity of convected plasma given by $\underset{\sim}{v}_{conv} = (\underset{\sim}{E} \times \underset{\sim}{B})/B^2$. The flow of plasma is antisunward in outer regions of the magnetosphere, and sunward in the inner regions. Good review articles treating magnetospheric convection include those by Axford (1969) and Stern (1977).

As convected plasma nears the earth, gradient and curvature drift begin to dominate over $\underset{\sim}{E} \times \underset{\sim}{B}$ drift. Gradient and curvature drift are comparable in magnitude and in the same direction in the region of the ring current and inner edge of the plasma sheet. In the night sector, positively charged particles drift toward the dusk side, and negatively charged particles drift toward dawn (see Figure 3).

Physical processes in the inner magnetospheric regions are well enough understood so that a detailed, self-consistent modeling of the magnetosphere and ionosphere can be done. The Rice Convection Model is an algorithm for computer simulation of the inner portions of the magnetosphere which has been developed at Rice University over the past several years. This model is discussed in section I.B.

2) Magnetosphere-Ionosphere Coupling and Birkeland Currents

The plasma convection pattern in the polar ionosphere is qualitatively shown in Figure 4. The closed loops represent convection above the ionosphere (at approximately 200 km to 300 km alti-

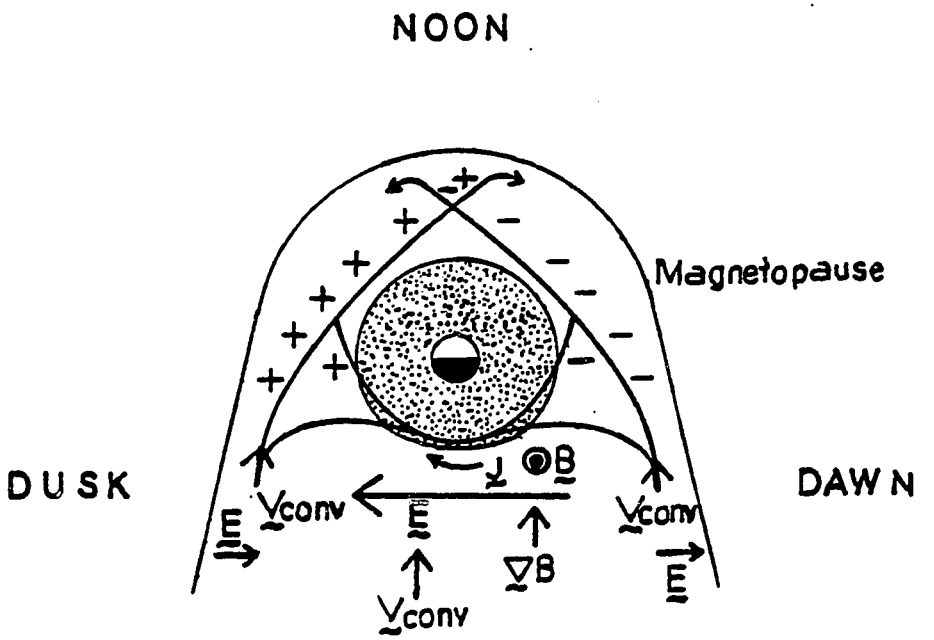

Figure 3. Schematic diagram of equatorial plane. $\underset{\sim}{J}$ is ring current; $\underset{\sim}{v}_{conv}$ is velocity of convected plasma. The dotted region represents the plasmasphere.

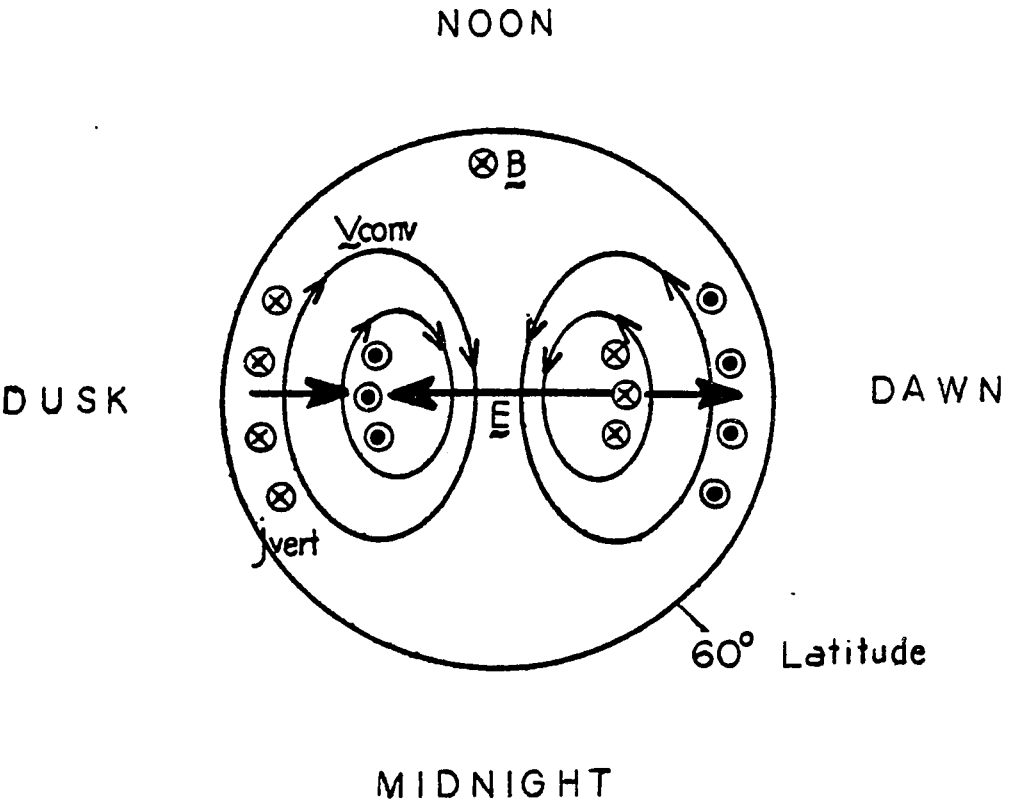

Figure 4. Polar view of ionosphere, with schematic diagram of convected plasma loops, and placement of Birkeland current (j_{vert}). Except where indicated, crosses and dots represent field-aligned current ingoing and outgoing from the ionosphere, respectively.

tude), with the direction of the convected plasma given by $\underset{\sim}{v}_{conv}$. The electric field reversal in the ionosphere marks the boundary between sunward and antisunward convecting plasma. (See Smiddy et al., 1980; Heelis et al., 1980; Bythrow et al., 1981; Doyle et al., 1981. Earlier papers include Heppner, 1972; Gurnett and Frank, 1973. Two of the original discovery papers are Frank and Gurnett, 1971; and Gurnett, 1970.)

Birkeland currents are magnetic field-aligned currents (FAC). Kristian Birkeland (1908) was the first to link high latitude magnetic perturbations with a horizontal ionospheric current system supplied by FAC from above (see Figure 5). Boström (1968) discussed the nature of Birkeland currents and early direct observational evidence for them. While ground magnetometers are useful indicators of horizontal Hall current, magnetic effects of Birkeland current are best identified by in-situ measurements. This is because ground magnetic disturbances from Birkeland and horizontal Pedersen currents approximately cancel each other (Fukushima, 1969).

Zmuda et al. (1966) first observed transverse magnetic disturbances at 1100 km in the auroral region. The observed transverse perturbations were highly localized in latitude, and they were interpreted as resulting from currents flowing along magnetospheric field lines.

There are two types of Birkeland currents. Small scale currents connect to individual arcs and were first observed and studied by means of rockets (see, e.g., Cloutier and Anderson,

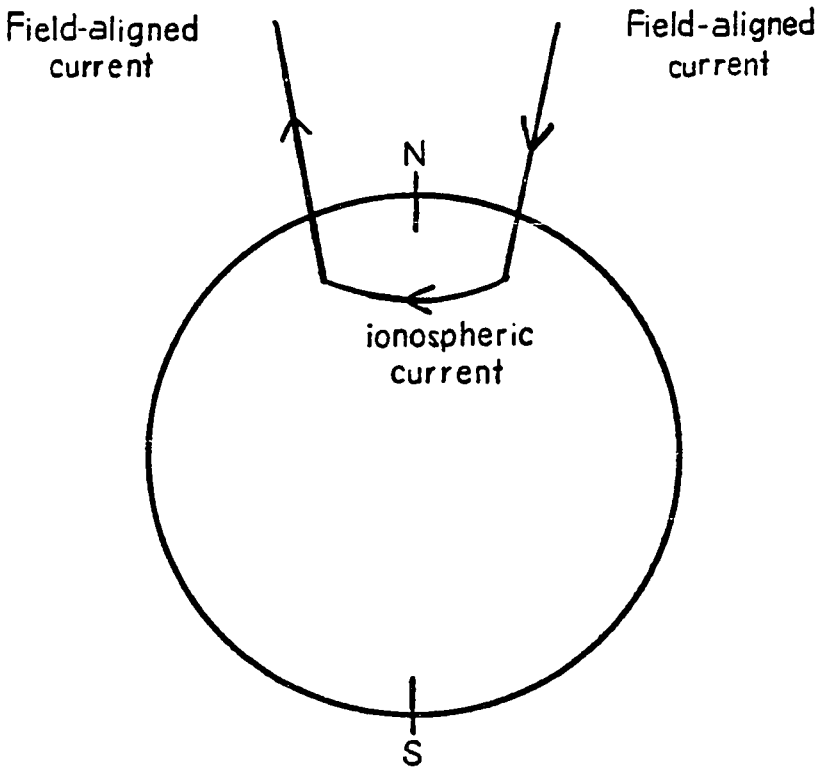

Figure 5. Schematic of system proposed by Birkeland (1908).

1975; Anderson and Vondrak, 1975). The large structures were first observed by Zmuda and Armstrong (1974a, b) using satellites. This dissertation focuses on aspects of the larger scale structure.

Recent experimental data indicate a large scale current distribution as in Figure 6, which is adapted from Iijima and Potemra (1978). Here, two regions of Birkeland currents are identified. The generally accepted view is that the higher latitude (region-1) FAC are somehow linked (details not understood) to the outermost magnetosphere and solar wind, while the lower latitude (region-2) FAC are linked to the ring current and plasma sheet (see Figures 1 and 7).

The classical idea for the source of region-2 FAC is as follows. A partial ring current flows from dawn to dusk as a result of the "charge separation" by gradient and curvature drifts. The region-2 current flows in order to complete the circuit that also includes ionospheric currents and the partial ring current (see Figure 7). The magnetospheric partial ring current maps along magnetic field lines to a region near the low-latitude edge of the auroral ionosphere, equatorward of the electric field reversal, implying that region-2 current flows on sunward convecting flux tubes. This explanation for the source of region-2 current is substantiated by the Rice computer simulations (Harel et al., 1981a, b).

Different magnetospheric models lead to different ideas about the source of region-1 currents. In the open model (see Figure

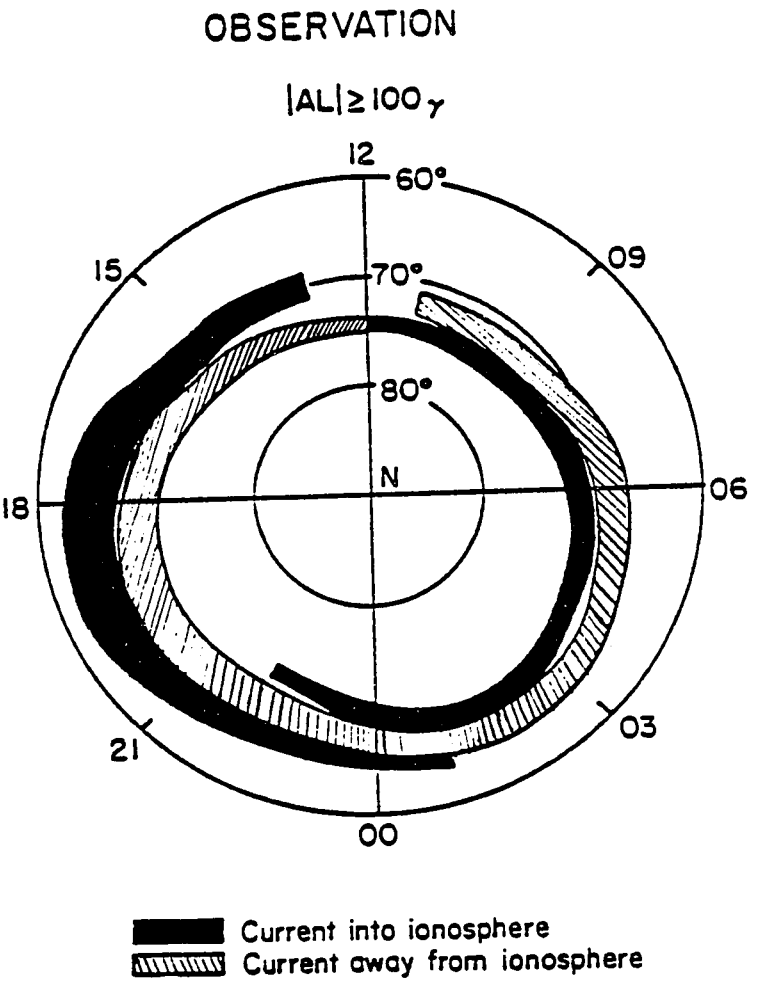

Figure 6. Distribution and flow directions of large scale field-aligned currents from data obtained by satellite from Iijima and Potemra (1978).

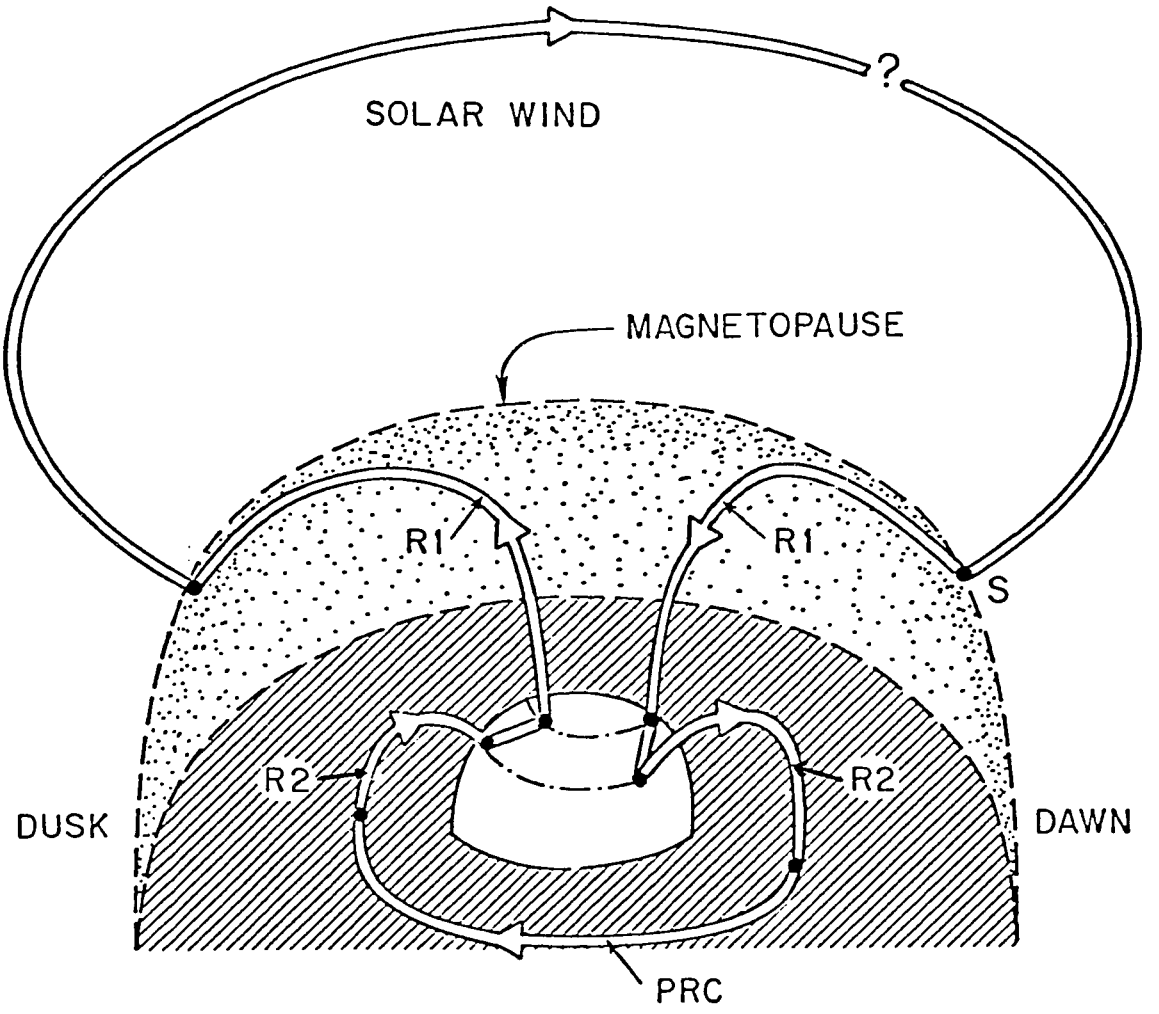

Figure 7. Schematic diagram of the basic magnetospheric-convection current system. The view is from behind (antisunward of) the Earth, and above the equatorial plane. The lined region is the equatorial plane; the dotted region, the dayside magnetopause. The notations "R1", "R2", and "PRC" mean "Region-1 Birkeland Current", "Region-2 Birkeland Current", and "Partial Ring Current". From Harel et al. (1981b).

8a), open field lines flow antisunward with the solar wind, in response to the dawn to dusk electric field. Closed field lines, which are not connected with solar wind, flow slowly sunward. In the portion of the auroral ionosphere equatorward of the electric field reversal, Pedersen currents flow equatorward on the dawn side and poleward on the dusk side. Thus, region-1 Birkeland currents must flow down into the ionosphere on the dawn side and up out of the ionosphere on the dusk side. The simplest open model thus implies that most region-1 current flows at the electric field reversal.

In the closed model (Figure 8b), friction with the solar wind causes a viscous-type boundary layer of closed field lines just inside the magnetopause. (Plasma just inside the magnetosphere presumably flows at a speed less than, but comparable to, the solar wind flow speed [typically ~400 km/sec]. Plasma at the earthward edge of the boundary layer flows slowly sunward at an inner-magnetospheric convection velocity [~20 km/sec].) Region-1 Birkeland current flows along these boundary-layer field lines. In the "pure" closed model, then, region-1 Birkeland current connects mostly to <u>antisunward</u> convecting flux tubes.

Nature may have chosen a hybrid magnetosphere. Recent observations suggest that the magnetosphere is open, but also possesses an antisunward-flowing boundary layer of closed field lines (Heelis et al., 1980). In the closed field line boundary layer, velocities are $\gtrsim$ 100 km/sec (antisunward) at the last closed field line to ~20 km/sec (sunward) at the earthward edge of the boundary

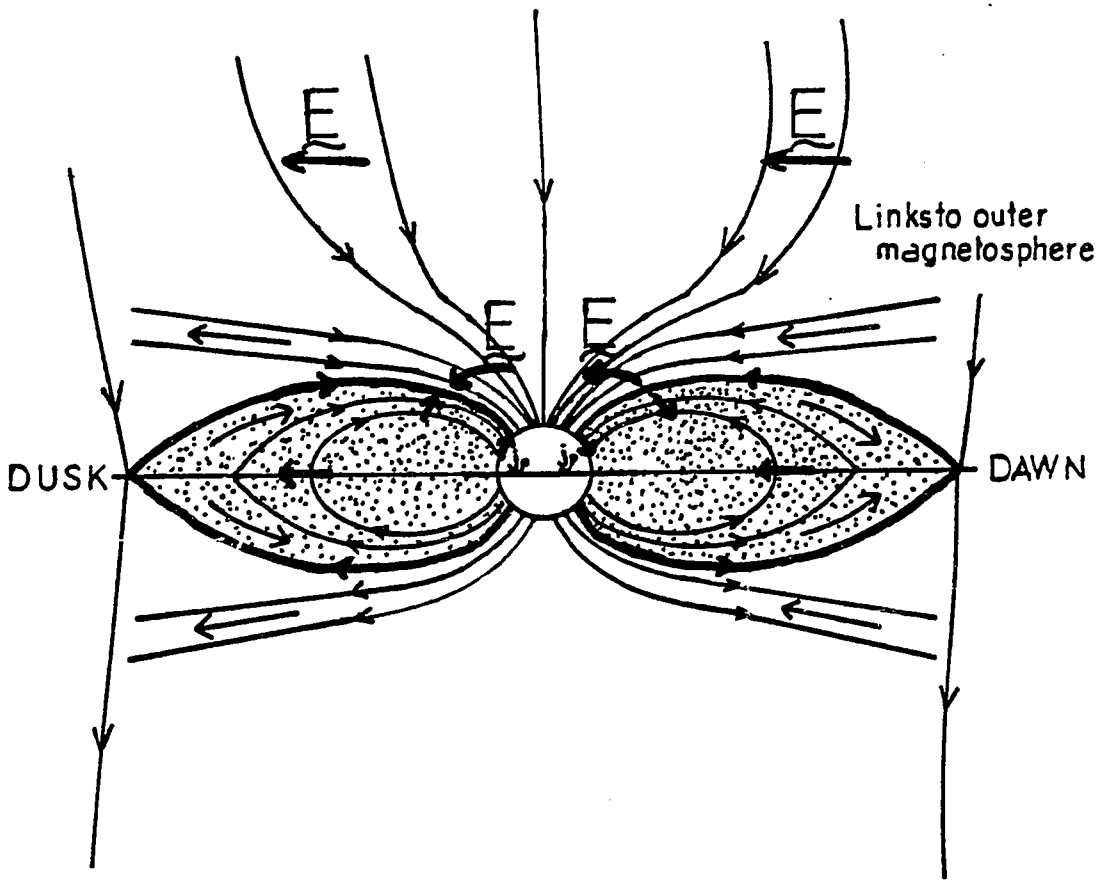

Figure 8(a). Open model, schematic. View looking to the sun, diagramming field-aligned current system linkage. Arrows in "tubes" indicate direction of current flow. Arrows on lines indicate magnetic field line directions. Heaviest arrows indicate Pedersen current, $\underset{\sim}{j}_p$, and electric field, $\underset{\sim}{E}$. Stippled region indicates the closed field line area. The heavy field lines represent the last closed field lines. (Southward IMF assumed).

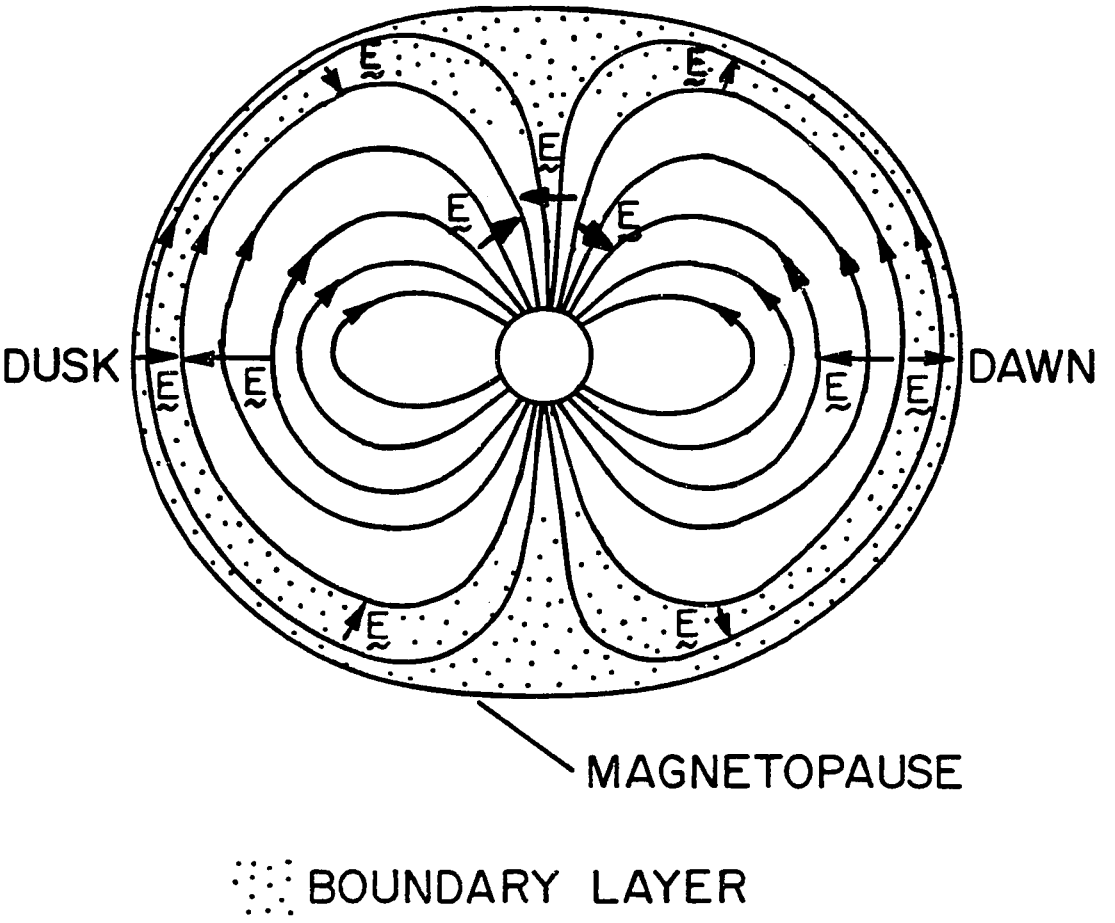

Figure 8(b). Closed model-schematic. View looking to the sun, diagramming field-aligned current system linkage. Arrows on lines indicate magnetic field line directions.

layer. (References on magnetospheric observations of plasma flow include Eastman et al., 1976; Hones et al., 1972; Hones et al., 1976.) In the hybrid model, the source of region-1 day side FAC includes a boundary layer phenomenon (Sonnerup, 1980). Region-1 Birkeland currents supposedly flow on all the boundary layer field lines. (Recently, however, Stern [1982] discounted the boundary layer as a source for Birkeland current, because he estimates that it could not produce currents as strong as those observed.) Within this viewpoint, the reversal is thought to occur within the flow of region-1 current, so that region-1 current flows predominantly on closed-field-line antisunward (boundary-layer) convecting flux tubes, and region-2 current flows solely on closed-field-line sunward convecting flux tubes. In this view, some region-1 currents connect along the "first" open field line to antisunward-flowing solar wind. Other region-1 currents connect to currents that flow in the boundary layer, which is in contact with the solar wind. Thus, it is again expected that region-1 currents flow mainly on antisunward-flowing field lines.

These classical thoughts for region-1 current are wrong, as evidenced by recent S3-2 data (see section I.B.3), which frequently show <u>most of the region-1 current flowing on regions of sunward convection</u>, so that all of region-2 current and most of region-1 current are equatorward of the electric field reversal. Figure 9 shows a pass over the north polar region from S3-2 data. The dusk portion shows a clear discrepancy with classical expectations.

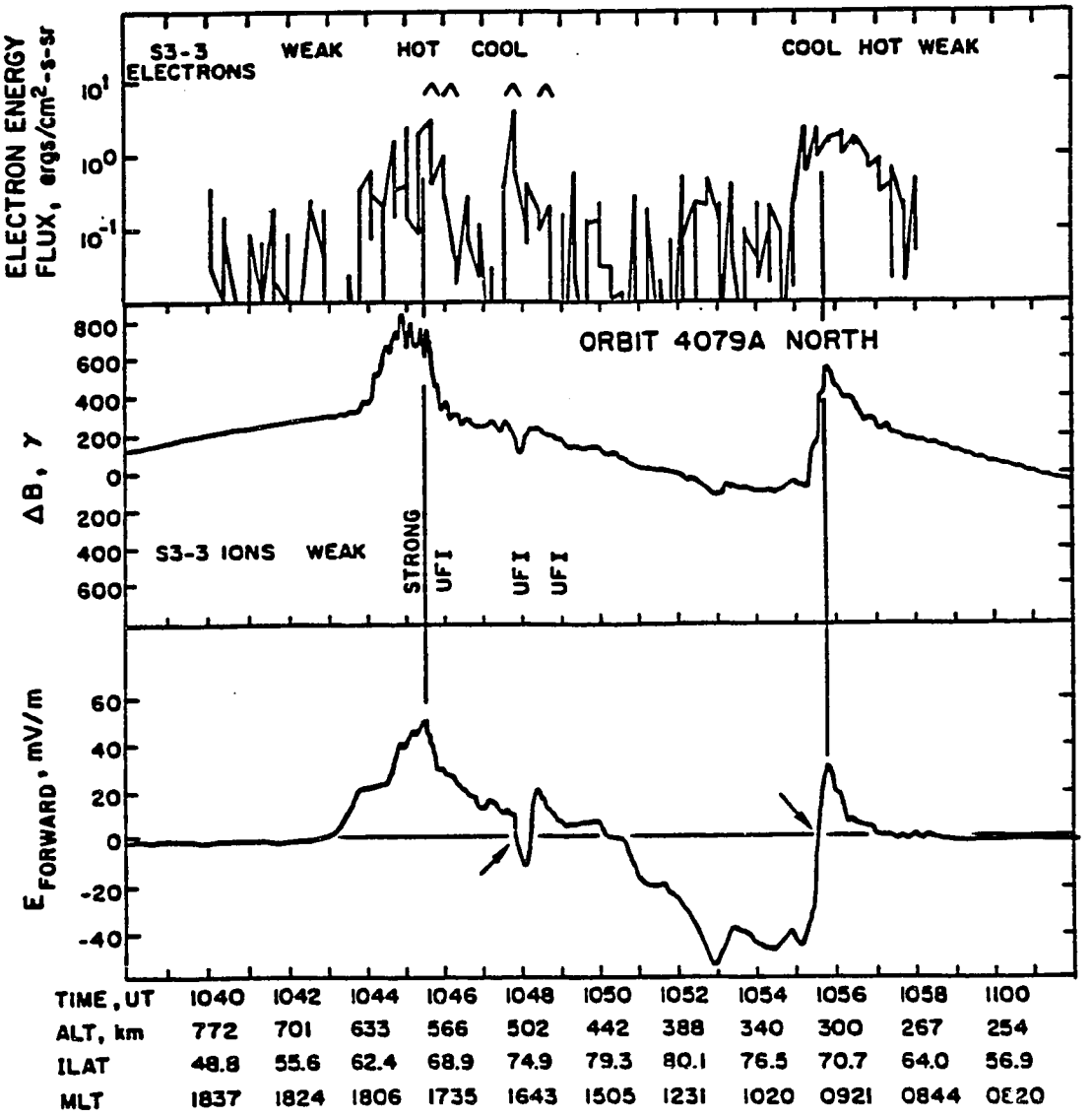

Figure 9. Precipitating electron energy flux, east-west magnetic perturbations, Δ B, and forward component of electric field for orbit 4079A, Northern hemisphere (S3-2 satellite data). Arrows in bottom panel point to the most equatorward electric field reversal; vertical lines are at equatorward edge of region-1 currents. From Harel et al., 1981a.

Measurements from the S3-3 satellite (Mozer et al., 1979, 1980; Cattell et al., 1979) are shown in Figures 10a and 10b. A dawn pass is displayed in Figure 10a and a dusk pass is displayed in Figure 10b. (Birkeland current is basically given by the latitudinal derivative of ΔB, so that the latitudinal extent of the current is given by the extent of magnetic field perturbation.) In the dawn S3-3 pass, about half of the region-1 current flows on sunward convecting flux tubes. (This could be in agreement with classical expectations for the "pure" open field line magnetospheric model.) However, in the dusk side S3-3 pass all of the region 1 current is in an area of sunward convection. Figures 11a and 11b display statistical summaries of S3-3 data, indicating that the relative positions of FAC and the electric field reversal seen in Figures 10a and 10b are representative of the analyzed passes. The dusk S3-3 passes again show a clear discrepancy with any classical expectations.

This discrepancy between the classical view of region-1 currents and data is a major motivation for this thesis, which focuses on the "non-classical" region-1 current flowing on regions of sunward convecting flux tubes. Stern (1982) hypothesizes that the plasma sheet may provide the source for region-1 Birkeland currents. (On the day-side, Stern suggests open field lines near noon as the source for cusp currents.)

The basic reason why region-1 field-aligned current flows is clear if the system is viewed as analogous to an electrical circuit. The magnetosphere acts as a generator, while the ionosphere

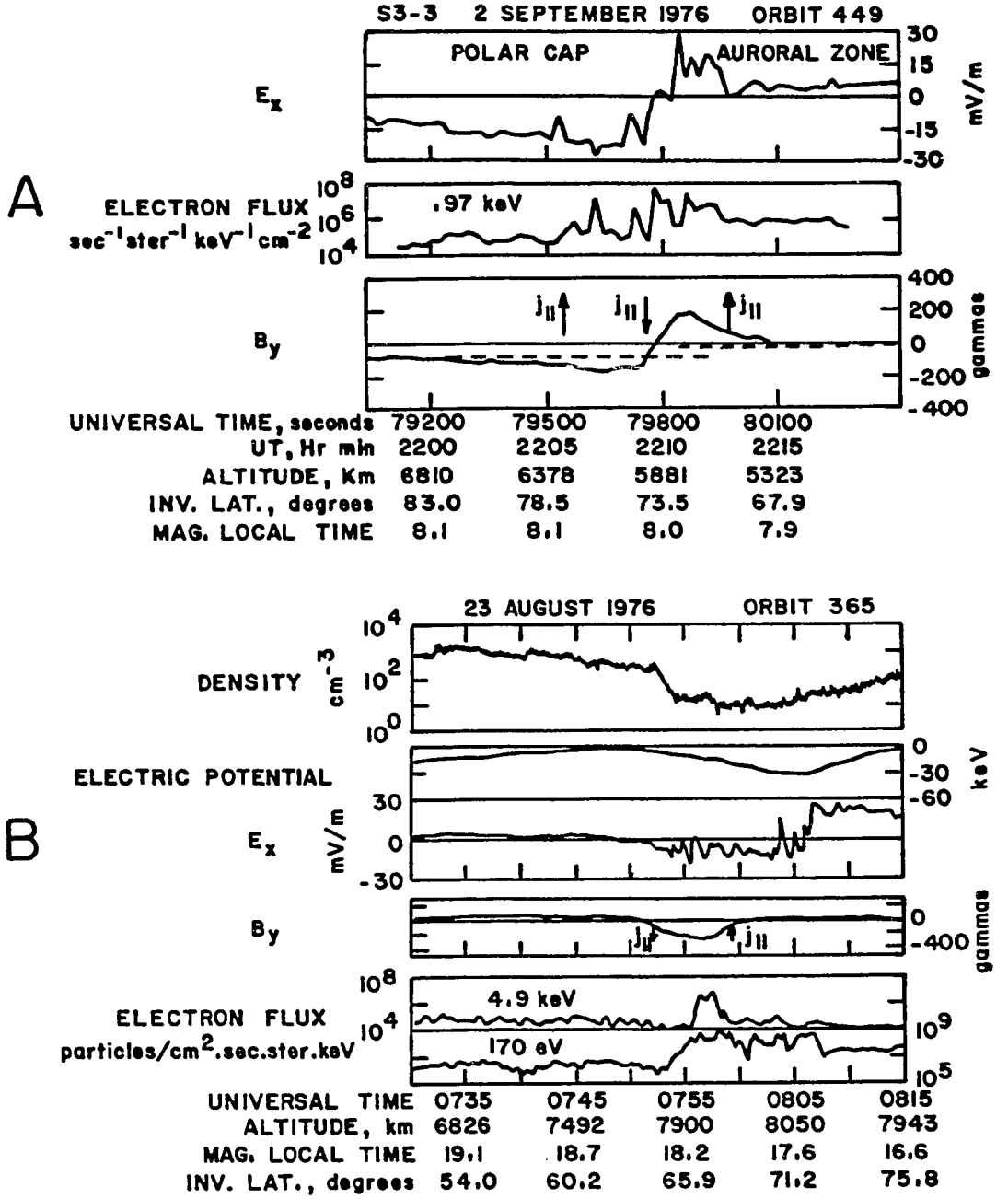

Figure 10(a). The x-component of the large scale electric field, the downward electric flux, and the field-aligned current observed in the morning auroral zone. From Mozer et al., 1980.

(b). Measurements of plasma density, field-aligned currents, the dc electric fields, and electron flux during a passage from the plasmasphere to the polar cap near local dusk. From Mozer et al., 1979.

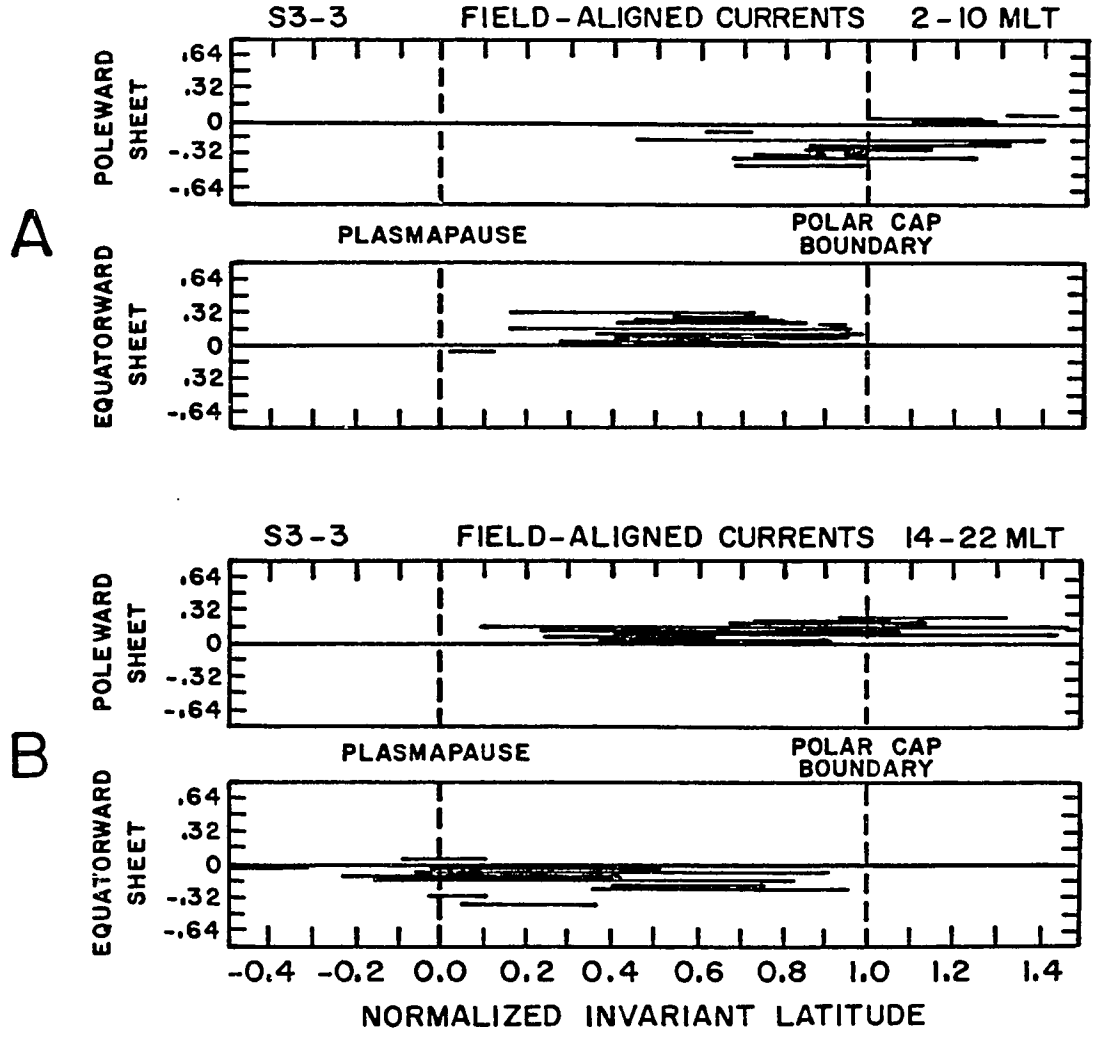

Figure 11 The locations and magnitudes of field-aligned current (positive is upward, negative is downward) relative to plasmapause and polar cap boundaries. These field-aligned currents are in units of A/m.

(a). For data obtained between 02:00 and 10:00 magnetic local time. From Mozer et al., 1980.

(b). For data obtained between 14:00 and 22:00 magnetic local time. From Mozer et al., 1980.

acts as a resistor. In this analogy, the resistor (i.e., the ionosphere) needs a current supply, and FAC fulfill the need. The highest latitude Birkeland currents connect the ionosphere to the magnetosphere (i.e., the generator) with flow down into the higher potential region of the ionosphere and up from low potential regions. FAC flow in order to maintain currents in the ionosphere. The magnetosphere serves as a type of "buffer" between the solar wind and the ionosphere.

3) Substorms and Unanswered Questions

An active sun produces variable solar wind which in turn causes magnetospheric disturbances. A magnetic storm is an intense magnetospheric disturbance. The first indication at the magnetosphere of a classical magnetic storm is the sudden compression of the magnetosphere, because of the passage of an interplanetary shock wave carried by the solar wind. (Frequently, the passage of a tangential discontinuity also compresses the magnetosphere.) In a classic storm, the compression is then followed by explosive processes (i.e., substorms) within the magnetosphere, each lasting from about one to three hours. During an individual storm, there may be as many as ten substorms. Generally, the substorm reaches a peak in an interval of fifteen minutes to half an hour. During growth and decay of the substorm, auroral activity increases and decreases accordingly (see Akasofu, 1968, for a review of substorms). A storm is defined by the development of a "ring current," which is a buildup of 3-300 keV particles on

trapped orbits in the inner magnetosphere. This results in a noticeable decrease in the geomagnetic field, as seen in ground magnetometer data obtained at low latitudes.

In a magnetospheric substorm, a substantial amount of energy is explosively released into the polar ionosphere. From the earth, a substorm is seen as a disruption of normal ionospheric electrodynamics. A substorm is usually identified by growth, expansion and recovery phases in ground magnetometer data, and enhanced auroral precipitation.

A substorm growth (or development) phase could begin when the interplanetary magnetic field shifts southward and encounters the magnetosphere. Shortly thereafter, the magnetopause moves earthward due to erosion of magnetic flux. Flux is added to the lobe of the tail from the day-side by the solar wind. The lobe magnetic energy density increases and the plasma sheet thins (in the region ~ 8 to 30 R_E) as tail current moves earthward. The plasma sheet thins in north-south extent, shrinking toward the equatorial plane. In the region from ~ 10 to 30 R_E, the tail magnetic field increases.

At the onset of the expansive phase of a substorm, there is a release of magnetic energy which was stored during the growth phase. The magnetic field lines near the tail change from tail-like to dipolar form. The tail magnetic field decreases. The growth and expansion phases may be indicative of the same phenomena, but with different intensities (Aubry, 1972; McCormac, 1972). The recovery phase begins when tail lobe is exhausted.

One of the proposed causes of a substorm is magnetosphere-ionosphere coupling and current control by precipitation resulting in a feedback system. According to Atkinson (1979), the most likely cause of the onset is an increase in the electric field due to an increase in the cross tail potential drop or a decrease in the width of the auroral oval (a region of large frequency of occurrence of aurora). An alternative view is the tail current-interruption model discussed in Chapter IV.

A substorm may occur periodically to deflate the magnetic field. That is, the substorm may be of internal origin, with enhancement of the substorm if the southward component of the IMF increases.

Technological developments in the last decade provide satellites with the ability to observe many of the phenomena necessary to describe the magnetosphere. However, several basic questions still remain unanswered. Among these are:

(1) What is the source mechanism for region-1 Birkeland current? That is, where in the outer magnetosphere do the region-1 currents connect, and what kinds of currents do they connect to?

(2) What is the cause of substorms?

   (a) What is the substorm triggering mechanism?

   (b) What causes the plasma sheet behavior (i.e., thinning and subsequent refilling)?

   (c) How is the recovery phase initiated?

(3) Is the magnetosphere open or closed?

(4) How is energy transferred from the solar wind to the magnetosphere?

The first of these questions provides the direct impetus for this thesis. The other abovementioned questions are related topics.

B. Rice Convection Model

1) General Method

The Rice Convection Model (RCM) self-consistently calculates ionospheric, Birkeland, and ring currents (Jaggi and Wolf, 1973; Harel and Wolf, 1976; Harel et al., 1981a; Wolf et al., 1982). The approach is to utilize time dependent input data (as available) along with the solution of differential equations. The large scale motions of plasmas in the magnetosphere-ionosphere system are described by the differential equations that are solved. The model applies to the region of the magnetosphere where magnetic field lines are closed.

Traditionally, this model has not provided a mechanism for region-1 type current generation. Before discussing an extension of the Rice Convection Model further out into the magnetosphere, a brief review of the model is presented, since a working RCM was necessary before any of this present work could be carried out. Within the backdrop of the RCM, the higher latitude field-aligned currents are investigated in the present work. (The RCM is described thoroughly by Harel et al. [1981a].) Figure 12 shows the overall logic of the RCM. The starting place in Figure 12 is

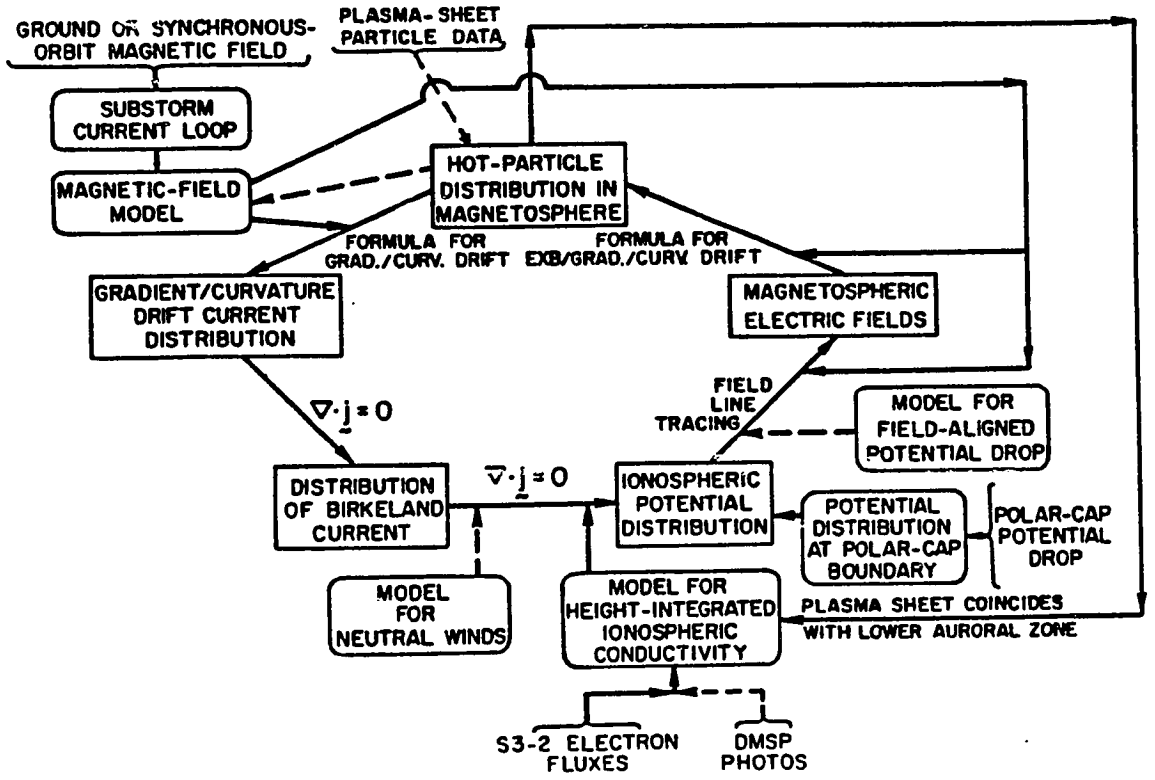

Figure 12. Overall logic diagram of Rice Convection Model. Arrows indicate flow of information in the program. (Dashed lines indicate features that will be incorporated in the program, but are not included yet.) The rectangles at the corners of the central pentagon represent basic parameters computed. Input models are indicated by rectangles with round corners; input data are indicated by curly brackets. The program cycles through the entire main program (including all the rectangular boxes) every time step. From Harel et al., 1981a.

at the top of the pentagon, with the plasma distribution at time t. The plasma distribution is taken to be isotropic. It is depicted in terms of 21 "species." For each species k, there is a charge q_k, an energy invariant, $\lambda_k = E_k[\int(ds/B)]^{2/3}$, and a number or density invariant, $\eta_k = n_k \int(ds/B)$. The quantity $\int(ds/B)$ is the volume of a flux tube per one unit of magnetic flux (e.g., per Weber). Respectively, E_k and n_k are the particle kinetic energy and number density for species k. The distribution of a species, k, is described in terms of an inner edge location to which particles penetrate.

Next, the gradient and curvature drift current densities are computed as shown in Figure 12 (moving counterclockwise from the top), with the assumed particle distribution and a magnetic field model. By balancing currents (i.e., current conservation), the Birkeland current distribution is obtained. From this, input boundary conditions and an input conductivity model, the ionospheric potential distribution can be calculated. Mapping the potential distribution back (along magnetic field lines) to the magnetosphere allows the magnetospheric electric field to be found. With the magnetospheric electric potential, the $\underset{\sim}{E} \times \underset{\sim}{B}$ velocity can be calculated. This $\underset{\sim}{E} \times \underset{\sim}{B}$ velocity is then added to the gradient and curvature drift velocity to give inner-edge particle drifts relative to the model grid system. With the drift velocity and a specified time interval, Δt, the inner edge locations are found. This same process, starting from an initial specified plasma distribution is repeated for each $t + \Delta t$.

The equations used in the above flowchart are discussed in section II.A. In this dissertation, different "computer experiments" were performed by choosing different input parameters in order to investigate the generation of some of the higher latitude (region-1) FAC. That is, a different input plasma distribution can be used in the program by initially choosing the appropriate energy invariants, number invariants, and inner edge locations for each of 21 species.

2) Rice Convection Model Applied to September 19, 1976, Substorm Event

With the Rice Convection Model, three geophysical events — the substorm-type event of September 19, 1976, the magnetic storm of July 29, 1977, and the magnetic storm of March 22, 1979 — have been computer simulated. Theory has been compared with observational data (Harel et al., 1981b; Spiro et al., 1981; Wolf et al., 1982). For the purposes of the "computer experiments" discussed in this dissertation, input data from the September 19, 1976, substorm event are used. The Rice Convection Model exists in two basic versions. Versions A and B were previously used for the September 19, 1976, substorm event and the July 29, 1977, storm, respectively. For this dissertation, version B was used for the September 19 event. Version B keeps track of the motion of individual inner edge particles. A point is added if two adjacent points drift too far apart. A point is deleted if two adjacent points drift too close together. This approach allows tracking

of complicated inner edge forms, specifically "tongues" of plasma or plasma "tails." Particle loss by precipitation is neglected. Versions A and B are described in detail by Harel et al. (1981a) and Wolf et al. (1982), respectively. (Inputs chosen for the "computer experiments" discussed in this dissertation are included in section II.C, and Chapter III.)

3) Inconsistencies Found as a Result of the RCM Applied to the Substorm Event

Results of application of the RCM to the September 19, 1976, event are summarized in Harel et al. (1981b) and Spiro et al. (1981). As previously mentioned, S3-2 satellite data (see, e.g., Harel et al., 1981a) unexpectedly show that it is common for the high latitude electric field reversal to occur poleward of most of the region-1 current. That is, frequently most of the region-1 FAC flows on regions of sunward convecting flux tubes. This is a puzzling and important feature. One of the aims of this dissertation is to describe a mechanism by which some region-1 type FAC could flow from or to regions of sunward convecting plasma.

Data often show large changes in ΔB (implying region-2 FAC) poleward of model-predicted region-2 FAC (see, e.g., Figures 8, 11, and 12 of Harel et al., 1981b). Assuming that plasma sheet particles gradient, curvature, and $\underset{\sim}{E} \times \underset{\sim}{B}$ drift, they connect to FAC where there are gradients in η's. (This is seen with equation (5) in Section II.A.2.) Thus, observed changes in ΔB (i.e., Birkeland currents) imply that the η's must increase systemati-

cally with geocentric distance, far beyond the usual inner-edge region. However, the number invariant (η) in the traditional picture should be invariant along a drift trajectory for a particle drifting in from the tail without loss (as shown in Appendix 1 of Harel et al., 1981a). For the traditional convection picture, it is inconsistent to have η increase systematically with increasing radial distance, and still be constant along drift trajectories. This inconsistency between observed and theoretical region-2 FAC is suggestive of a problem with the usual picture of magnetospheric convection. One interpretation of the discrepancy is that there is loss of particles from plasma sheet flux tubes during some phase of a substorm (Erickson and Wolf, 1980). This interpretation leads to the notion of "variable flux tube content."

Chapter II discusses the concept of variable flux tube content, stability, and the application of an adapted form of the RCM. Chapter III details the "computer experiments" used to study the generation of region-1 FAC. Chapter IV is a discussion of a proposed magnetospheric current system and related topics. A summary and conclusion for the work is included in the last chapter.

II. VARIABLE FLUX-TUBE CONTENT

A. Feasibility Arguments

1) Pressure Considerations

Erickson and Wolf (1980) studied the possibility that steady, adiabatic convection could not exist in a closed magnetic field line region extending into a long magnetotail. Assuming that plasma sheet flux tubes have enough plasma pressure to balance lobe magnetic pressure at 60 R_E, then plasma pressure and magnetic pressure are unequal (by an order of magnitude) at 15 R_E. The inequality comes about as the result of adiabatic compression. Erickson and Wolf (1980) hypothesize that sunward convection must be time-dependent and that plasma may be released from plasma-sheet flux tubes during a substorm. Thus, the flux tubes in some local-time sector have their plasma content reduced. These flux tubes with reduced plasma content are "depleted." The supposition here is that "depleted" flux tubes are nearer to the earth, and "filled" flux tubes are further away. A gradient in the number invariant, η, leads to generated field-aligned currents. (See equations (5) and (6) of Harel et al., 1981a, and the following subsection.) Specifically, a decrease in plasma flux-tube content in a limited local time sector in the center of the tail results in FAC down into the ionosphere on the dawn side of the depleted section, and up from the ionosphere on the dusk side. These are in the direction of region-1 Birkeland currents.

In the next subsection, the necessary conservation equations are presented. Next, the motion of a bubble of underpopulated flux tubes (or of blobs of overpopulated tubes) is discussed. Following that discussion is an analysis of the stability of the variable flux tube content discussed here. Particularly, we address the question of whether or not a limited local time sector of depleted flux tubes is a stable configuration.

2) Conservation Equations

Before studying bubble motion, or stability of the system, general equations governing the coupling between ionospheric and magnetospheric currents should be reviewed. (Unless otherwise noted, this discussion follows the treatment of Wolf and Spiro, 1982.)

Assume magnetohydrodynamic plasma dynamics and isotropic plasma pressure. The momentum equation is

$$\rho \frac{D\underset{\sim}{v}}{Dt} = -\nabla p + \underset{\sim}{J} \times \underset{\sim}{B} \qquad \text{(II.A.2-1)}$$

where ρ is the mass density, $D\underset{\sim}{v}/Dt$ is the convective derivative for velocity, p is the pressure, $\underset{\sim}{J}$ is the current per unit area, and $\underset{\sim}{B}$ is the magnetic field. From equation (II.A.2-1), the component of $\underset{\sim}{J}$ perpendicular to $\underset{\sim}{B}$ is expressed as:

$$\underset{\sim}{J}_{\perp} = \frac{\underset{\sim}{B} \times \nabla p}{B^2} + \frac{\underset{\sim}{B} \times \left(\rho \frac{D\underset{\sim}{v}}{Dt}\right)}{B^2} \qquad \text{(II.A.2-2)}$$

The $\underset{\sim}{B} \times \nabla p$ term represents gradient drift, curvature drift, and magnetization currents. The $D\underset{\sim}{v}/Dt$ term is "acceleration drift" current, which is neglected for the inner magnetosphere. In Wolf (1983), the inertial term is shown to be smaller than the pressure-gradient $(\underset{\sim}{B} \times \nabla p)/B^2$ term by a factor of ~0.02. Thus,

$$\underset{\sim}{J}_{\perp} = \frac{\underset{\sim}{B} \times \nabla p}{B^2} \qquad \text{(II.A.2-3)}$$

After some manipulation, the gradient and curvature drift current can be found from equation (II.A.2-3) to be

$$\underset{\sim}{j}_e(\underset{\sim}{x}_e) = \lambda\eta\{\hat{z}_e \times \nabla_e[(\int \frac{ds}{B})^{-2/3}]\} \qquad \text{(II.A.2-4)}$$

where $\underset{\sim}{j}_e$ is the current per length in the equatorial plane. Balancing current in the equatorial plane with the Birkeland current, we get

$$j_{\parallel e} = -\nabla_e \cdot \underset{\sim}{j}_e = -\nabla_e(\lambda\eta) \cdot \{\hat{z}_e \times \nabla_e[(\int \frac{ds}{B})^{-2/3}]\} \qquad \text{(II.A.2-5)}$$

where $j_{\parallel e}$ is the Birkeland current per unit area away from the equatorial plane. (Here λ, and η have the previous definitions.)

The ionospheric current conservation equation (see Karty et al., 1982) is

$$\nabla_h \cdot [\underset{\approx}{\Sigma} \cdot (-\nabla_h V)] = j_{\parallel i} \qquad \text{(II.A.2-6)}$$

where ∇_h is a horizontal gradient operator in the ionosphere, $\underset{\sim}{\Sigma}$ is the tensor representing height-integrated conductivity, $j_{\parallel i}$ is the positive current per unit area down into the ionosphere, and V is the electric potential. The quantity $j_{\parallel i}$ is given by

$$j_{\parallel i} = (B_i/B_e) j_{\parallel e} \qquad \text{(II.A.2-7)}$$

where B_i is the magnetic field at the ionosphere, and B_e is the magnetic field in the equatorial plane. Thus, from equations (II.A.2-5) and (II.A.2-7)

$$j_{\parallel i} = -\left(\frac{B_i}{B_e}\right) \nabla_e \lambda\eta \cdot \{\hat{z}_e \times \nabla_e [(\int ds/B)^{-2/3}]\}. \qquad \text{(II.A.2-7a)}$$

However, since pressure and flux-tube volume are constant along a given field line, and magnetic fluxes in the ionosphere and magnetosphere are equal, we can write

$$j_{\parallel i} = -\nabla_i \eta\lambda \cdot \{\hat{z}_i \times \nabla_i [(\int ds/B)^{-2/3}]\} \qquad \text{(II.A.2-7b)}$$

(Here, we have assumed that the dip angle is $\pi/2$, since we are using $\hat{z}_i$ instead of using a unit vector along $\underset{\sim}{B}$.)

3) Bubble Motion

In this section, we discuss the motion of a "bubble" of underpopulated flux tubes. By "ionospheric bubble" in this section, we refer to a region where the plasma content is less than

that of its surroundings. We calculate the motion of an ionospheric bubble to see if this "depleted" region will naturally move toward local midnight. We are interested in finding if, given the condition of having several bubbles, a depleted section would form in the midnight region. This is an important first step in considering the stability of a depleted region in the center of the magnetotail.

We assume a flattened two-dimensional polar coordinate system, centered on the middle of a circular ionospheric bubble. We take the flux tube volume to have a constant large scale gradient, as shown in Figure 13. (Although the obvious gradient in flux tube volume is radially away from the Earth, we take the gradient in flux tube volume to be away from the center of the magnetotail as a preliminary exercise for more elaborate stability calculations.)

We assume that

$$\eta = \begin{cases} \eta_1, & \rho < b \\ \eta_2, & \rho > b \end{cases} \qquad \text{(II.A.3-1)}$$

where b is the radius of the bubble. The quantity $\nabla_i \eta$ is nonzero only on the surface boundary, so that according to equation (II.A.2-7b), Birkeland current is generated only at $\rho = b$.

We start the analysis of bubble motion by examining the expression for $j_{\parallel i}$, Birkeland current per unit area down into the ionosphere. Equation (II.A.2-7b) can be written

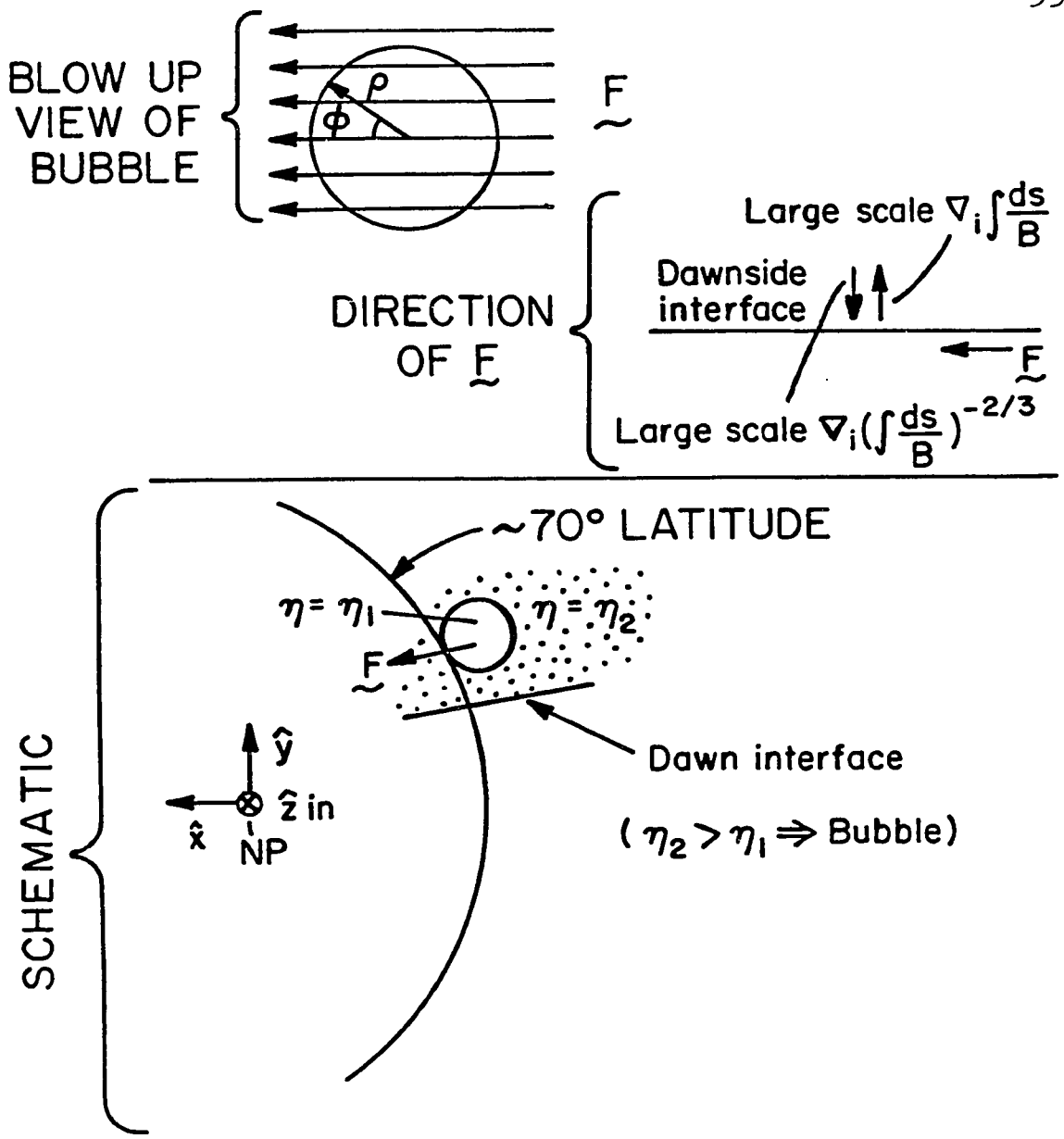

Figure 13. Flattened ionospheric coordinate system (ρ, and ϕ are bubble centered coordinates). See equation II.A.3-2 for a definition of $\underset{\sim}{F}$.

$$j_{\parallel i} = -(\eta_2 - \eta_1)\lambda|\underset{\sim}{F}| \cos \phi \ \delta(\rho - b) \qquad \text{(II.A.3-2)}$$

where

$$\underset{\sim}{F} = \{\hat{z}_i \times \nabla_i[(\int \frac{ds}{B})^{-2/3}]\}$$

The quantity, ϕ, is the angle between the vectors $\underset{\sim}{F}$ and $\nabla_i \eta\lambda$. (Refer to Figure 13.)

The conductivity is given by the tensor form:

$$\underset{\approx}{\Sigma} = \begin{pmatrix} \Sigma_P & \Sigma_H \\ -\Sigma_H & \Sigma_P \end{pmatrix},$$

where Σ_P is the Pedersen conductivity, and Σ_H is the Hall conductivity. (Both conductivities are height integrated.) Taking uniform conductivity, equation (II.A.2-6) is rewritten

$$\Sigma_P \nabla_h^2 V = -j_{\parallel i} \qquad \text{(II.A.3-3)}$$

With equations (II.A.3-2) and (II.A.3-3), we have

$$\nabla_h^2 V = \frac{(\eta_2 - \eta_1)\lambda|\underset{\sim}{F}|}{\Sigma_P} \cos \phi \ \delta(\rho - b) \qquad \text{(II.A.3-4)}$$

which is equivalent to

$$\nabla_h^2 V = \frac{a}{\Sigma_P} \cos \phi \ \delta(\rho - b) \qquad \text{(II.A.3-5)}$$

where a is a constant. Here, we have set

$$a = (\eta_2 - \eta_1)\lambda|\underset{\sim}{F}| \qquad \text{(II.A.3-6)}$$

for convenience. Using separation of variables, a solution to $\nabla_h^2 V = 0$ in polar coordinates is found to be of the form

$$V(\rho,\phi) = (A\rho + B\rho^{-1}) \cos \phi + (D\rho + E\rho^{-1}) \sin \phi \qquad \text{(II.A.3-7)}$$

The solution to the inhomogeneous equation (II.A.3-5) is

$$V(\rho,\phi) = \begin{cases} A\rho \cos \phi, & \rho < b \\ B\rho^{-1} \cos \phi, & \rho > b \end{cases} \qquad \text{(II.A.3-8)}$$

There is no sin ϕ appearing in equation (II.A.3-8), since it is not present in equation (II.A.3-5). For $\rho < b$, the ρ^{-1} term is zero since $\rho = 0$ is included in this region. For $\rho > b$, the ρ term is zero since it would represent a large scale convection electric field, not a field associated with bubble motion. That is, we are interested in calculating the velocity of a small bubble relative to its surroundings.

Matching the potential at $\rho = b$ gives

$$A = Bb^{-2} \qquad \text{(II.A.3-9)}$$

In order to evaluate A and B, a second condition is given by the discontinuity of $\partial V/\partial \rho$ at $\rho = b$. From equation (II.A.3-5), we

have

$$\frac{1}{\rho}\frac{\partial}{\partial\rho}\left(\rho\frac{\partial V}{\partial\rho}\right)+\frac{1}{\rho^2}\frac{\partial^2 V}{\partial\phi^2}=\frac{a}{\Sigma_P}\cos\phi\ \delta(\rho-b) \qquad \text{(II.A.3-10)}$$

Multiplying by ρ, and integrating from $\rho = b - \varepsilon$ to $\rho = b + \varepsilon$, we get

$$\left[\rho\frac{\partial V}{\partial\rho}\right]_{b-\varepsilon}^{b+\varepsilon}=b\frac{a}{\Sigma_P}\cos\phi \qquad \text{(II.A.3-11)}$$

Upon integration, the second term in equation (II.A.3-10) is negligible, since we are integrating over such a small interval in ρ. Using equation (II.A.3-8) and assuming $\varepsilon/b \ll 1$, this becomes

$$-Bb^{-2}-A=\frac{a}{\Sigma_P} \qquad \text{(II.A.3-12)}$$

We now have two relations (equations (II.A.3-9) and (II.A.3-12)) for A and B. The first was obtained by matching the potential at $\rho = b$, and the second was obtained by matching the discontinuity in slope of the potential at $\rho = b$. Solution of the system of equations (II.A.3-9) and (II.A.3-12) gives

$$\left\{\ A=-\frac{a}{2\Sigma_P}\ \text{and}\ B=-b^2\frac{a}{2\Sigma_P}\ \right\} \qquad \text{(II.A.3-13)}$$

so that (with equation (II.A.3-8))

$$V(\rho,\phi) = \begin{cases} -\frac{a}{2\Sigma_P}\,\rho\,\cos\,\phi, & \rho < b \\ -b^2\,\frac{a}{2\Sigma_P}\,\rho^{-1}\,\cos\,\phi, & \rho > b \end{cases} \qquad \text{(II.A.3-14)}$$

Now that the potential is known, the drift velocity of a bubble can be found by using:

$$\underset{\sim}{v}_{conv} = \frac{\underset{\sim}{E} \times \underset{\sim}{B}_i}{B_i^2} \qquad \text{(II.A.3-15)}$$

with $\underset{\sim}{E} = -\nabla_i V$, and $\underset{\sim}{B}_i = B_i \hat{z}_i$. We have:

$$\underset{\sim}{v}_{conv} = \frac{1}{B_i}\left(-\frac{\partial V}{\partial \phi}\,\frac{1}{\rho}\,\hat{\rho} + \frac{\partial V}{\partial \rho}\,\hat{\phi}\right) \qquad \text{(II.A.3-16)}$$

The expression for the convective drift velocity is found to be:

$$\underset{\sim}{v}_{conv} = \begin{cases} \frac{1}{B_i}\left(-\frac{a}{2\Sigma_P}\,\sin\,\phi\,\hat{\rho} - \frac{a}{2\Sigma_P}\,\cos\,\phi\,\hat{\phi}\right), & \rho < b \\ \frac{1}{B_i}\left(-\frac{b^2 a}{2\Sigma_P}\,\rho^{-2}\,\sin\,\phi\,\hat{\rho} + \frac{b^2 a}{2\Sigma_P}\,\rho^{-2}\,\cos\,\phi\,\hat{\phi}\right), & \rho > b \end{cases}$$

(II.A.3-17)

where a is positive for bubble motion ($\eta_2 > \eta_1$), and a is negative for blob motion ($\eta_2 < \eta_1$).

The left portion of Figure 14 illustrates that for a bubble of underpopulated flux tubes, a small scale electric field builds up inside the bubble that moves toward the midnight region. The right side of Figure 14 shows that for a blob of overpopulated

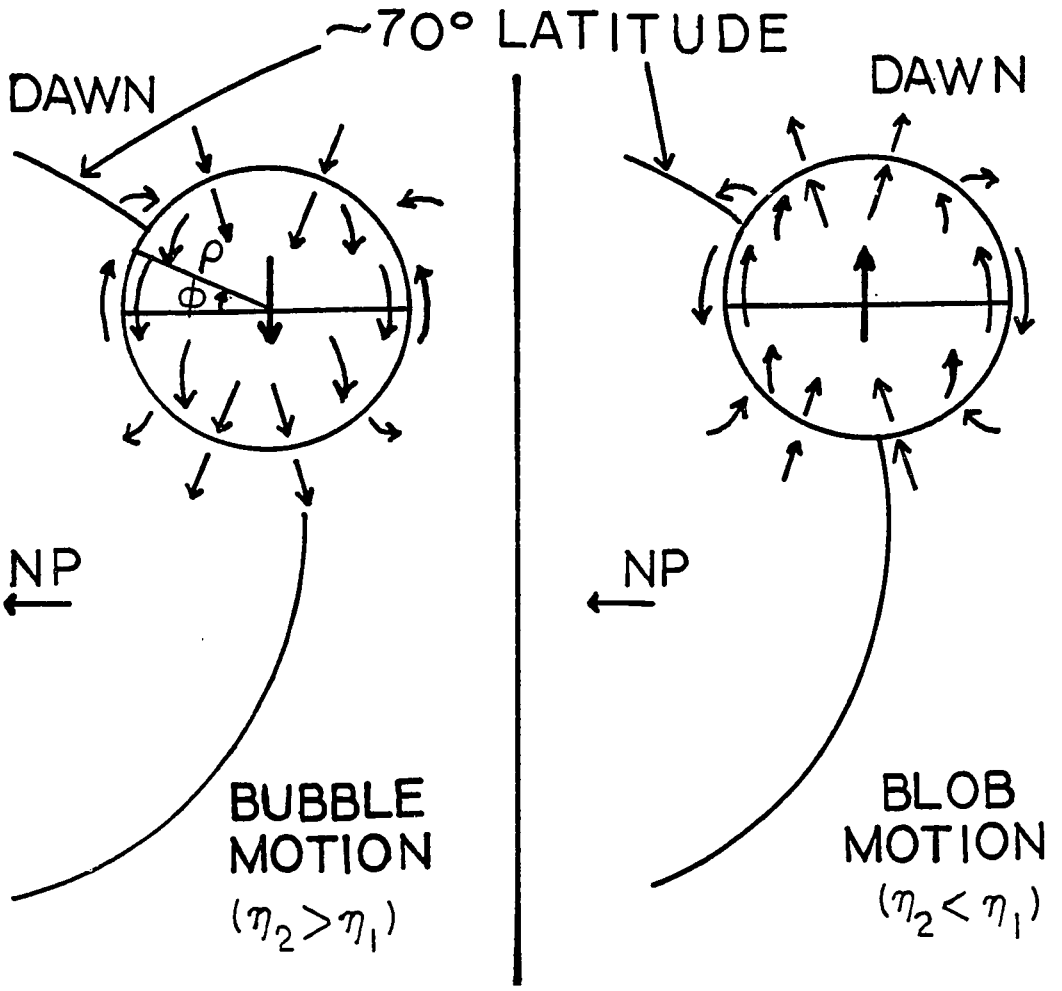

Figure 14. Schematic of flow pattern in the ionosphere. View is looking down on the North Pole. (Bubble and blob are greatly enlarged.)

flux tubes, a small scale electric field builds up inside the blob that moves it out away from the midnight region. Motion toward the midnight region in the ionosphere corresponds to motion toward the axis of the magnetotail. Thus, we can use this result to discuss motion in the magnetosphere. To summarize, we can write that:

$$\begin{cases} \underset{\sim}{v}_{conv} \parallel -\nabla \int ds/B & \text{if } \eta_2 > \eta_1 \\ \underset{\sim}{v}_{conv} \parallel \nabla \int ds/B & \text{if } \eta_2 < \eta_1 \end{cases}.$$

We could have obtained this result for two cases: (i) $\nabla \int ds/B$ is radially outward and (ii) $\nabla \int ds/B$ is azimuthal, away from the magnetotail axis. We have applied this result to the second case where $\nabla \int ds/B$ is away from the tail axis. Again, it should be mentioned that we took the gradient in flux tube volume to be away from the center of the magnetotail as a preliminary calculation.

Given that bubbles of less populated flux tubes move toward the axis of the magnetotail in this analysis, the next step is to consider the stability of less populated flux tubes closer toward the axis of the magnetotail.

4) Stability Analysis

This subsection is divided as follows. First, the energy principle is used for a general stability analysis of a static (nonflowing) system. Then, stability calculations using the conservation equations discussed in section II.A.2 are presented for the stability of plane interface geometry with flow.

The energy principle (Krall and Trivelpiece, 1973) states that a static system in equilibrium is unstable if a change in the system produces a decrease in potential energy. It does not apply if the unperturbed plasma has flow velocity. The energy principle is used in this section of the thesis with an interchange instability in order to investigate the notion that less occupied flux tubes ought to end up closer to earth in a region of high magnetic field. We treat the plasma as an ideal gas. See Figure 15 for a schematic of the situation. For an ideal gas:

$$pV = (\gamma - 1)W_p \qquad \text{(II.A.4-1)}$$

where $\gamma = (5 + f)/(3 + f)$. Here p is the pressure, V is the volume, and W_p is the internal energy of plasma, and f is the number of non-translational degrees of freedom. The adiabatic expansion of an ideal gas gives us PV^γ = constant. Now consider the change in plasma energy (ΔW_p) as a result of an interchange. We are interchanging tubes of equal magnetic flux, so that the magnetic energy does not change. We have a nonzero ΔW_p because of volume changes of the two interchanged tubes. Before the interchange, the initial volumes of the flux tubes to be interchanged are V_I and V_{II}. The initial pressures are P_{Ii} and P_{IIi}, respectively. (Refer to Figure 15.) After the interchange, the plasma that was occupying V_{II} with p_{IIi} now occupies V_I with p_{IIa}. Also, after the interchange, the plasma that was occupying V_I with P_{Ii} now occupies V_{II} with p_{Ia}. Then, with equation (II.A.4-1) and PV^γ =

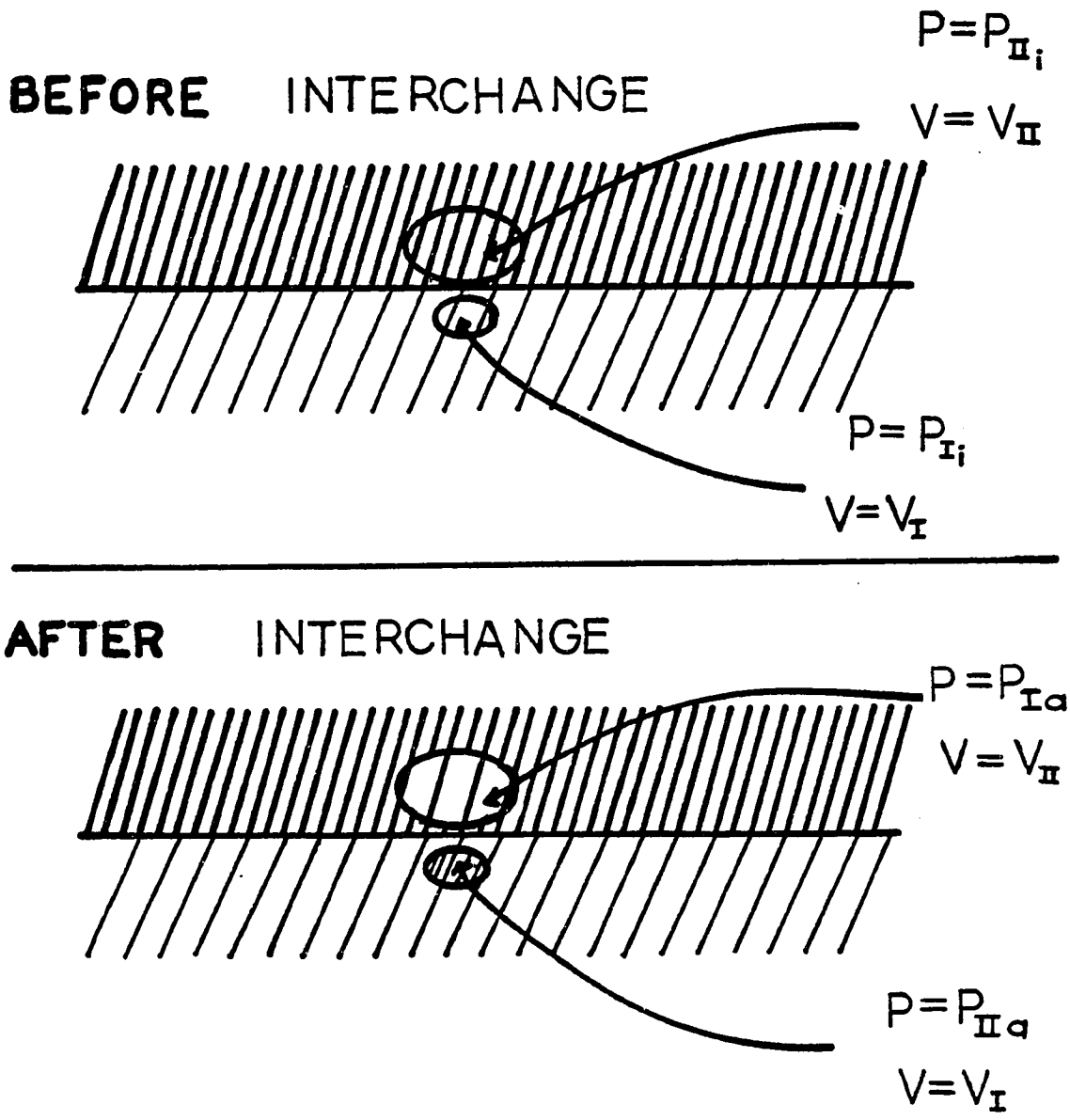

Figure 15. Schematic of situation to be investigated for stability analysis. (p is pressure, V is volume.)

constant, we can write:

$$\Delta W_p = \frac{1}{\gamma - 1} \left\{ \left(\frac{p_{Ii} V_I^{\gamma}}{V_{II}^{\gamma}} \right) V_{II} + \left(\frac{p_{IIi} V_{II}^{\gamma}}{V_I^{\gamma}} \right) V_I - p_{Ii} V_I - p_{IIi} V_{II} \right\} \tag{II.A.4-2}$$

We assume that p_{Ii} and p_{IIi} differ by a small amount, and also that V_I and V_{II} differ by a small amount, so that we write:

$$\left\{ \begin{array}{l} p_{IIi} = p_{Ii} + \delta p \\ V_{II} = V_I + \delta V \end{array} \right\} \tag{II.A.4-3}$$

Then, putting equation (II.A.4-3) into (II.A.4-2), expanding by using the binomial theorem, $(1 + x)^n = 1 + nx + ([n(n - 1)]/2)x^2 + \ldots$, and keeping terms to second order, we obtain

$$\Delta W_p = \delta p \delta V + \gamma p_{Ii} \frac{(\delta V)^2}{V_I} \tag{II.A.4-4}$$

The system is unstable if $\Delta W_p < 0$. According to equation (II.A.4-4), the condition for <u>instability</u> can be written:

$$\frac{\delta p}{p_{Ii}} < -\gamma \frac{\delta V}{V_I} \tag{II.A.4-5}$$

(We will define $\delta V > 0$ in Equation (II.A.4-3).) For $\delta V > 0$, the system is unstable if the pressure decreases faster than adiabatic as the volume increases. (No instability occurs if both $\delta V > 0$ and $\delta p > 0$.)

We can apply this result to the magnetosphere. The obvious gradient in flux tube volume is radially away from the Earth, not away from the center of the magnetotail. We take the gradient in flux tube volume in the $\hat{y}$-direction in order to investigate the simplest case. With this preface, we assume that the interface shown in Figure 15 is toward the dawn side of the magnetotail in the equatorial plane. (The Earth is to the left.) The portion above the interface in Figure 15, then, is analogous to the outer portion of the magnetotail and the portion below the interface is analogous to the center of the magnetotail. We also assume that there is a large scale constant gradient in flux tube volume, such that flux tube volumes increase with distance away from the center of the magnetotail. If we have pressure decreasing fast enough with distance away from the center of the magnetotail, we have an instability, according to equation (II.A.4-5).

The stability of the system can also be investigated by installing a boundary ripple in a plane interface geometry. We are assuming a two-dimensional rectangular coordinate system. From analogy to the bubble motion analysis, we can write the non-homogeneous equation to be solved as

$$\nabla_h^2 V = \frac{(\eta_2 - \eta_1)\lambda \; |\hat{z}_i \times \nabla_i [(\int ds/B)^{-2/3}]|}{\Sigma_P} \cos \xi_i \; \delta(y_i - y_{0i}) \tag{II.A.4-6}$$

where ξ_i is the angle between $\{\hat{z}_i \times \nabla_i \; [(\int(ds/B))^{-2/3}]\}$ and $\nabla_i \eta\lambda$.

Here y_{0i} represents the position of the interface in the ionosphere. (Coordinates given with a subscript "i" refer to the ionosphere.)

There is a large scale increase in flux tube volume (as viewed in the equatorial plane) in the radial direction. For a flux tube volume gradient which increases radially out in the tail region, there are components of the flux tube volume gradient which are perpendicular and parallel to the interface (see Figure 16).

We now consider $\nabla_i[(\int ds/B)^{-2/3}]$ to have both a parallel and perpendicular component. We can then solve the conservation equation considering each component separately and then add the solutions. First, we consider the perpendicular component and then the parallel component of gradient in flux tube volume.

Taking the component of flux tube volume that increases in the positive $\hat{y}_i$- direction (see Figure 17), then the vector quantity $\{\hat{z}_i \times \nabla_i [(\int ds/B))^{-2/3}]\}$ is in the positive $\hat{x}_i$-direction. If we take $\nabla_i \eta$ to be in the positive $\hat{y}_i$- direction (i.e., $\eta_2 > \eta_1$), or the negative $\hat{y}_i$-direction (i.e., $\eta_2 < \eta_1$), then $j_{\parallel i}$ is zero, so that we have $\nabla_h{}^2 V = 0$. If a ripple forms in the interface between low and high η regions, then $\nabla_i \eta$ is slightly offset ($\xi_i \sim 90°$, $\cos \xi_i \ll 1$) from the $\hat{y}_i$- direction, so that a small Birkeland current is generated. Thus, $\nabla_h{}^2 V = 0$, except on the rippled boundary, where $\nabla_h{}^2 V = j_{vert}/\Sigma_P$, with j_{vert} equal to generated vertical Birkeland current.

We take the ripple to be expressed as

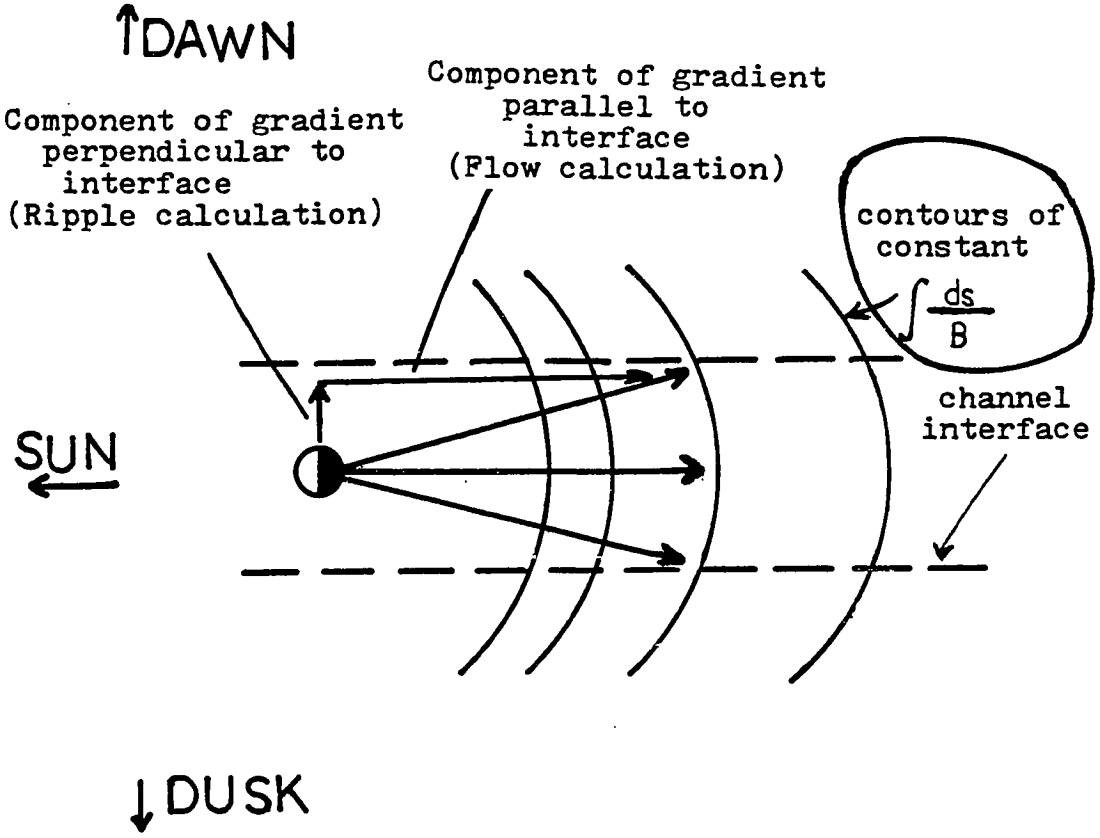

Figure 16. Schematic for consideration of perpendicular and parallel components of gradient in flux tube volume. Equatorial plane view - not to scale.

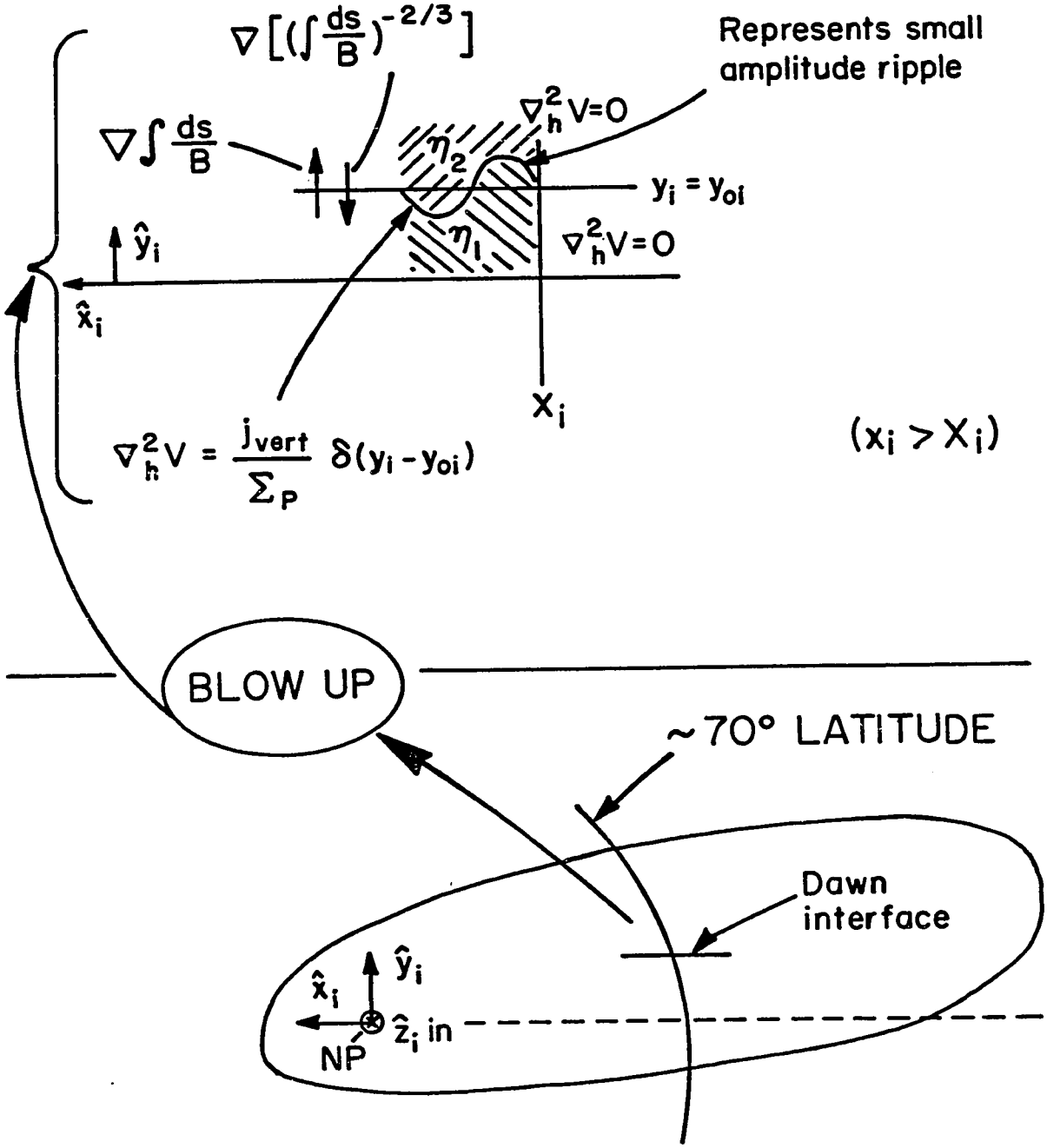

Figure 17. Ionospheric view of coordinate system for stability calculations.

$$(y_{1i} - y_{0i}) = c_i(t) \sin k_i(x_i - X_i)$$

in the ionosphere. We are assuming $k_i > 0$. We want to find $\cos \xi_i$ in terms of a function of x_i. Referring to Figure 18, we see that:

$$\cos \xi_i \sim - \gamma_i \cos k_i(x_i - X_i) \qquad \text{(II.A.4-7)}$$

This assumes $\gamma_i |\cos k_i (x_i - X_i)| << 1$, since we consider a small ripple. (We have let $\gamma_i = c_i k_i$.) So, we can express equation (II.A.4-6) as

$$\nabla_h^2 V = - \frac{a}{\Sigma_P} \gamma \cos k(x - X) \delta(y - y_0) \qquad \text{(II.A.4-8)}$$

where $\gamma = c_i k$. (We have dropped the "i" subscript for the rest of the derivation, except where needed for explicit clarification.) Here $a = (n_2 - n_1)\lambda \, |\hat{z}_i \times \nabla_i [(\int ds/B)^{-2/3}]|$.

The homogeneous equation $\nabla_h^2 V = 0$ is written as

$$\frac{\partial^2 V}{\partial x^2} + \frac{\partial^2 V}{\partial y^2} = 0 \qquad \text{(II.A.4-9)}$$

for this coordinate system. Using separation of variables, a solution is found to be

$$V(x,y) = A \left(\cos k(x - X)\right)e^{-k|y|} + B\left(\sin k(x - X)\right)e^{-k|y|} \qquad \text{(II.A.4-10)}$$

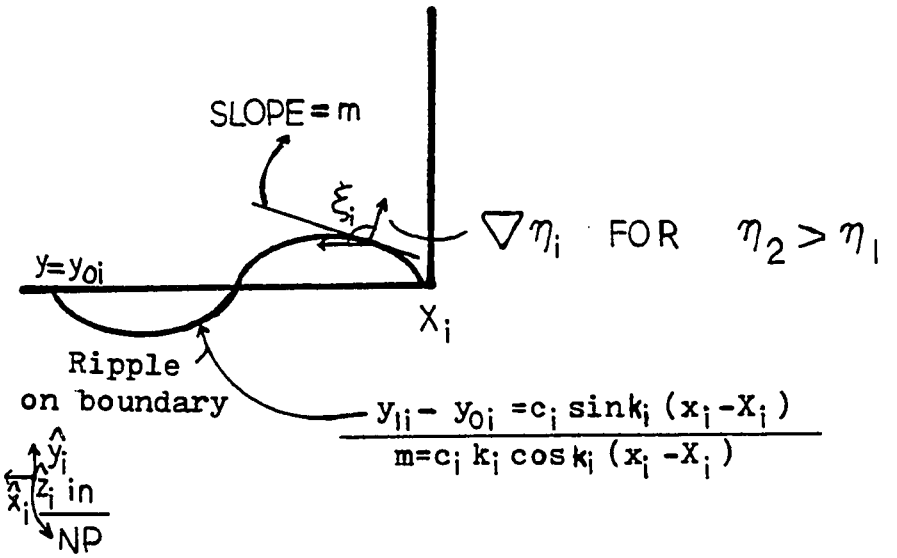

$$\cos\xi_i = \frac{-\text{sign}(\cos k_i (x_i - X_i))}{\sqrt{1 + \frac{1}{m^2}}}$$

Figure 18. Schematic for calculation of angle ξ_i.

where the $e^{+k|y|}$ solutions have been ignored since we are only concerned with decaying solutions ($e^{-k|y|}$) here. The solution to the inhomogeneous equation (II.A.4-8) for this situation is

$$V(x,y) = \begin{cases} A_U e^{-k(y-y_0)} \cos k(x - X), & y > y_0 \\ A_L e^{+k(y-y_0)} \cos k(x - X), & y < y_0 \end{cases} \qquad \text{(II.A.4-11)}$$

There is no sin k(x - X) appearing in equation (II.A.4-11), since it is not present in equation (II.A.4-8). Matching the potential at $y = y_0$ gives

$$A_U = A_L \qquad \text{(II.A.4-12)}$$

In order to solve for this constant, another expression relating A_U and A_L is needed. This second condition is given by the discontinuity of $\partial V/\partial y$ at $y = y_0$. From equation (II.A.4-8), we have

$$\frac{\partial^2 V}{\partial x^2} + \frac{\partial^2 V}{\partial y^2} = -\frac{a}{\Sigma_p} \gamma \cos k(x - X)\, \delta(y - y_0) \qquad \text{(II.A.4-13)}$$

Integrating from $y = y_0 - \varepsilon$ to $y = y_0 + \varepsilon$, we get

$$\left[\frac{\partial V}{\partial y}\right]_{y_0-\varepsilon}^{y_0+\varepsilon} = -\frac{a}{\Sigma_p} \gamma \cos k(x - X) \qquad \text{(II.A.4-14)}$$

Upon integration, the first term in equation (II.A.4-13) is negligible since we are integrating over such a small interval in y. Using equation (II.A.4-11), and assuming $k\varepsilon \ll 1$, this becomes

$$A_U + A_L = \frac{\gamma}{k} \frac{a}{\Sigma_P} \qquad \text{(II.A.4-15)}$$

We now have two relations (equations (II.A.4-12) and (II.A.4-15)) for A_L and A_U. The first was obtained by matching the potential at $y = y_0$ and the second was obtained by matching the discontinuity in slope of the potential at $y = y_0$. Solution of the system of equations (II.A.4-12) and (II.A.4-15) gives

$$\left\{ A_U = \frac{\gamma}{2k} \frac{a}{\Sigma_P} \text{ and } A_L = \frac{\gamma}{2k} \frac{a}{\Sigma_P} \right\} \qquad \text{(II.A.4-16)}$$

so that (using equation (II.A.4-11))

$$V(x,y) = \left\{ \begin{array}{l} \frac{\gamma}{2k} \frac{a}{\Sigma_P} e^{-k(y-y_0)} \cos k(x - X), \; y > y_0 \\ \frac{\gamma}{2k} \frac{a}{\Sigma_P} e^{k(y-y_0)} \cos k(x - X), \; y < y_0 \end{array} \right\} \qquad \text{(II.A.4-17)}$$

Now we can find the drift velocity of plasma in the ionosphere near the interface:

$$\underset{\sim}{v}_{conv} = \frac{1}{B_i} \left[\hat{x} \left(- \frac{\partial V}{\partial y} \right) + \hat{y} \left(\frac{\partial V}{\partial x} \right) \right] \qquad \text{(II.A.4-18)}$$

This is (with $\gamma_i = c_i k_i$),

$$\underset{\sim}{v}_{conv} = \begin{cases} \frac{1}{B_i}\left[\hat{x}\left(\frac{1}{2}\frac{a}{\Sigma_P} c_i k e^{-k(y-y_0)} \cos k(x - X)\right)\right. \\ \left. + \hat{y}\left(-\frac{1}{2}\frac{a}{\Sigma_P} c_i k e^{-k(y-y_0)} \sin k(x - X)\right)\right], \; y > y_0 \\ \frac{1}{B_i}\left[\hat{x}\left(-\frac{1}{2}\frac{a}{\Sigma_P} c_i k e^{+k(y-y_0)} \cos k(x - X)\right)\right. \\ \left. + \hat{y}\left(-\frac{1}{2}\frac{a}{\Sigma_P} c_i k e^{+k(y-y_0)} \sin k(x - X)\right)\right], \; y < y_0 \end{cases} \qquad \text{(II.A.4-19)}$$

We have

$$v_{conv_y}(y = y_0) = -\frac{1}{B_i}\frac{1}{2}\frac{a}{\Sigma_P} c_i k \sin k(x - X) \qquad \text{(II.A.4-20)}$$

We take (for example) the ripple to be above $y = y_0$ (that is, $\sin k(x - X) > 0$). We consider $n_2 > n_1$ here, so that we take $a > 0$ in equation (II.A.4-20). Thus, $v_{conv_y} < 0$ which means that the ripple moves toward the boundary (see Figure 19). That is, the ripple damps out. For $n_2 < n_1$, the sign reverses so that the ripple grows.

Now, we want to find the growth or decay rate of the ripple. For this, we set v_{conv_y} equal to dy_1/dt, which is the boundary ripple velocity. Thus,

$$\frac{dc_i}{dt} = -\frac{1}{B_i}\frac{1}{2}\frac{a}{\Sigma_P} c_i k$$

implying that

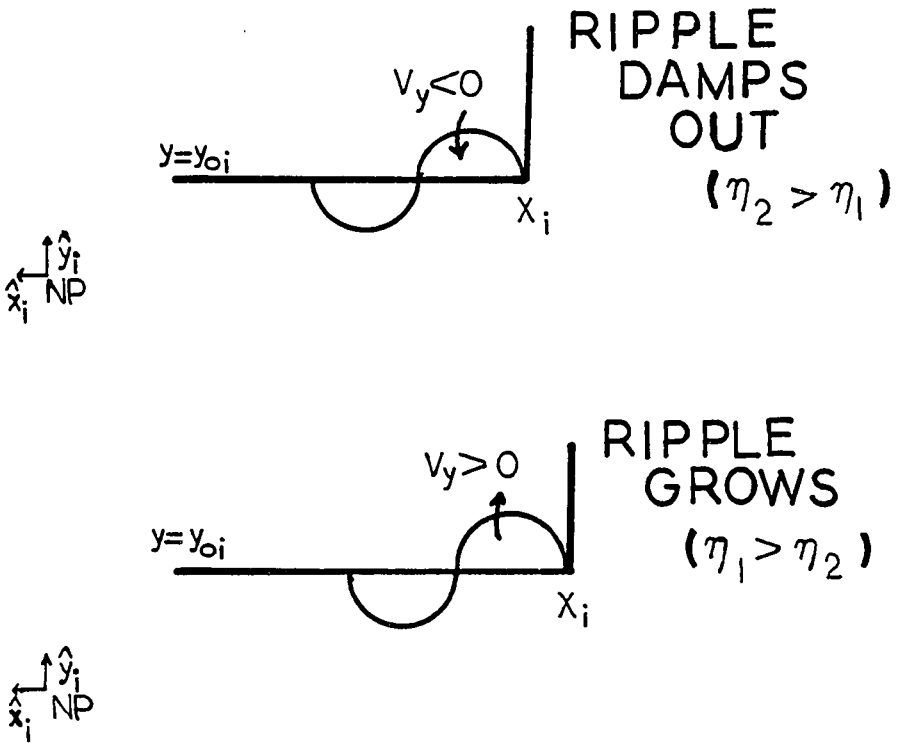

Figure 19. Diagram for stability considerations.

$$c_i = c_{0i} e^{-\frac{1}{B_i}\frac{1}{2}\frac{ak}{\Sigma_P}t} \qquad \text{(II.A.4-21)}$$

where a is positive for $\eta_2 > \eta_1$, and a is negative for $\eta_2 < \eta_1$. Since k is greater than zero, we see that we get ripple growth for higher density plasma further in ($\eta_2 < \eta_1$), but we get a damped ripple (i.e., stability) for low density plasma closer in to the center of the magnetotail ($\eta_2 > \eta_1$).

In summary, in considering the component of the uniform large scale gradient in flux tube volume that exists in the $\hat{y}_e$-direction (that is, in the direction away from the center of the magnetotail), then for a stable configuration, higher density plasma must be further away from the center of the magnetotail, and low density plasma must be closer in toward the center.

We have found equivalent results for stability analysis using either the energy principle or the movement of a boundary ripple in a plane interface geometry.

Interchange instabilities in the inner magnetosphere have been previously investigated (e.g., Richmond, 1973; Swift, 1967). However, it has been the stability of the plasmapause and ring current region which has been of concern, so that a very different geometry has been considered. For the plasmapause region, it is appropriate to take a flux-tube volume gradient which is radially outward. In this thesis, we have so far been concerned with effects of an azimuthal component in the flux tube volume gradient for the magnetotail region.

We have found that for a stable configuration, low density plasma must be close in toward the center of the magnetotail and high density plasma must be further out, assuming smaller flux tube volumes near the center of the magnetotail. Next, we investigate considerations of the parallel component of the gradient in flux tube volume. Here, we will look at the interface toward dawn (although there is another interface toward the dusk side).

For a large scale gradient in flux tube volume which is solely perpendicular to the interface, we cannot model unperturbed flow, since the vector $\underset{\sim}{F}$ is in the $\hat{x}_i$-direction and $\nabla_i \eta$ is in the $\hat{y}_i$-direction. The dot product $(\underset{\sim}{\nabla}_i \eta \cdot \underset{\sim}{F})$ is zero, and (without an installed ripple on the interface) we have no generation of field-aligned current. When we take flux tube volumes to increase with distance down the channel we are investigating the consequences of flow. The effect of flow is important in studying the channel problem. In a channel-like depleted region in the middle of the magnetotail, a high electric field develops by virtue of the lower density. Since the large scale convective velocity is dependent on electric field ($\underset{\sim}{v} \propto \underset{\sim}{E} \times \underset{\sim}{B}$), the flow will be greater in this channel-like region. We take the flow velocity equal to zero in the "out of channel" region ($\eta = \eta_2$), and the flow velocity equal to $\underset{\sim}{v}_{flow}$ in the channel-like depleted region ($\eta = \eta_1$).

From previous discussions, we have:

$$\nabla_h^2 V = \frac{1}{\Sigma_P} |(\eta_2 - \eta_1)\lambda| \; |\underset{\sim}{G}| \cos \phi \; \delta(y - y_0) \qquad \text{(II.A.4-22)}$$

where $\underset{\sim}{G} = \{\hat{z}_i \times \nabla_i [(\int(ds/B))^{-2/3}]\}$, and ϕ is the angle between the vectors $\underset{\sim}{G}$ and $\nabla_i \eta\lambda$. (Refer to equation (II.A.3-4).) We use $\underset{\sim}{G}$ here to designate a vector arising from the component of large scale gradient in flux tube volume which is parallel to the interface. Previously $\underset{\sim}{F}$ was used to designate a vector arising from the perpendicular component of gradient in flux tube volume. Assuming, however, that flux tube volumes will increase with distance down the channel (i.e., away from the Earth in the $+\hat{x}_e$-direction), then $\underset{\sim}{G}$ is in the negative $\hat{y}_i$-direction. (See Figure 20 for the coordinate system.) So, we have $\cos\phi = -(\text{sign}\ (\eta_2 - \eta_1)\lambda)\cdot 1$. (We consider only positive λ here.) Then equation (II.A.4-22) is rewritten as:

$$\nabla_h^2 V = -\beta(x)\ \delta(y - y_0) \qquad \text{(II.A.4-23)}$$

with

$$\beta = \frac{1}{\Sigma_P}(\eta_2 - \eta_1)\ \lambda\ |\underset{\sim}{G}| \qquad \text{(II.A.4-24)}$$

(We solve this equation in the ionosphere.) Integrating equation (II.A.4-23) from $y = y_0 - \varepsilon$ to $y = y_0 + \varepsilon$ as was similarly done in the ripple case, we obtain

$$\left[\frac{\partial V}{\partial y}\right]_{y_0-\varepsilon}^{y_0+\varepsilon} = -\beta \qquad \text{(II.A.4-25a)}$$

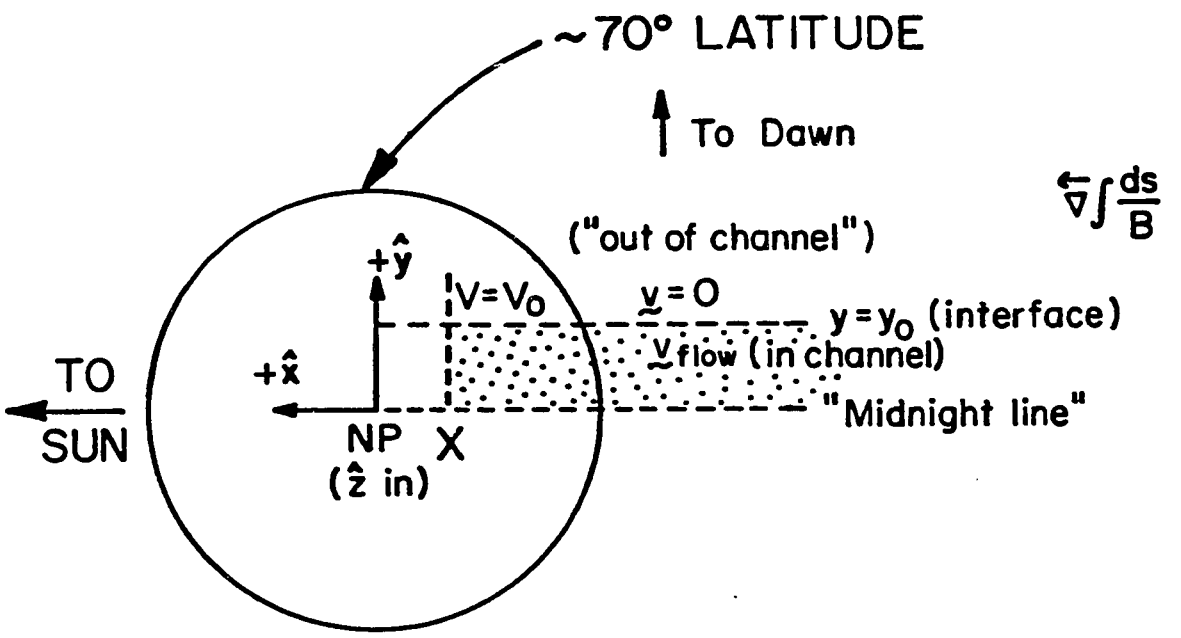

SCHEMATIC - IONOSPHERIC VIEW

Figure 20. Shaded region is the area of interest. (Only dawn portion is shown with $y < y_0$ and $X > x$.) Not drawn to scale.

The solution to equation (II.A.4-25a) with $V(y > y_0) = V_0$ (constant since there is no flow in the upper region) is:

$$V = \frac{V_0}{y_0}(y) \qquad (y < y_0) \qquad \text{(II.A.4-25b)}$$

where $\beta = V_0/y_0$. With equation (II.A.4-18), we can calculate flow velocity as:

$$\underset{\sim}{v}_{flow} = -\frac{1}{B_i}\left(\frac{V_0}{y_0}\right)\hat{x} \qquad \text{(II.A.4-26)}$$

This solution arises from considering a flux tube volume gradient which is parallel to the interface.

Now, we consider the addition of these two solutions. This is equivalent to looking at the case of a rippled boundary when flow is present. Considering the dawn interface, we have zero flow in the upper "out of the channel" region and non-zero flow velocity in the lower channel-like depleted region. However, it is convenient to look at this problem in a reference frame from which would be observed $\underset{\sim}{v} = [(1/2)|v_{flow}|]\,\hat{x}$ in the upper region and $\underset{\sim}{v} = [(-1/2)|v_{flow}|]\,\hat{x}$ in the in the lower region, with v_{flow} given by equation (II.A.4-26). We can write the ripple velocity as:

$$\left(\frac{d\delta y}{dt}\right)_{\text{with flow}} = \left(\frac{\partial \delta y}{\partial t}\right) + (v_x)\frac{\partial \delta y}{\partial x} \qquad \text{(II.A.4-27)}$$

using the convective derivative, where the interface is assumed

to be described by $y(x,t) = y_0 + \delta y(x,t)$. For a particle on the boundary, $v_x = [(1/2)|v_{flow}|]_{upper} + [(-1/2)|v_{flow}|]_{lower} = 0$, so that we have $(d\delta y/dt)_{with\ flow} = (\partial \delta y/\partial t)$. The ripple is described by $\delta y = c_i(t)e^{ikx}$. Therefore, $(d\delta y/dt)_{with\ flow} = (dc_i/dt)\ e^{ikx}$. We also have $(\partial \delta y/\partial t) = v_{perb\ y}$, with $v_{perb\ y}$ given by equation (II.A.4-19). Thus,

$$\frac{dc_i}{dt} = \frac{1}{\Sigma_P}\frac{1}{B_i}\, a\, (-\frac{1}{2}\, c_i)\, k$$

where a is given by equation (II.A.3-6). The solution to this is

$$c_i = c_{0i}e^{-i\omega t} \qquad \text{(II.A.4-28)}$$

where

$$\omega = -\frac{a}{\Sigma_P}\frac{1}{B_i}\, k\, (\frac{i}{2}). \qquad \text{(II.A.4-29)}$$

Now, we can let $e^{\delta t}$ represent the time dependence of the ripple and the real part of δ will give the growth or decay rate:

$$R_e(\delta) = -\frac{a}{2\Sigma_P}\frac{k}{B_i} \qquad \text{(II.A.4-30)}$$

Note that the ripple decays for $a > 0$ and grows for $a < 0$. This is a prediction of ripple growth if the density invariant of low volume flux tubes is larger than the density invariant of high volume flux tubes. This is equivalent to the previous result

obtained just considering the perpendicular component of flux tube volume (see equation (II.A.4-21)).

We now summarize what was shown in this section. We first supposed that a depleted channel of plasma formed in the center region of the magnetotail with low density and small flux tube volumes in this channel region. On either side of the channel, higher densities and large flux tube volumes were assumed. In the subsection on bubble motion, it was shown that a bubble of underpopulated flux tubes moves in toward the axis of the magnetotail, and a blob of overpopulated flux tubes moves out away from the axis of the magnetotail. Then, using both the energy principle and conservation equations applied to a rippled interface, it was found that a large scale gradient in flux tube volume outward from the center of the magnetotail was a stable configuration, for higher density plasma also further away from the center of the tail. Adding a gradient in flux tube volume down the channel does not affect stability.

In the next section (II.B), we consider specific consequences of the existence of the channel-like region in the magnetotail.

B. Hypothesis

1) Contours of Constant η

In the previous section on feasibility, it was argued that higher density plasma sheet flux tubes stay further away from the center of the magnetotail. That is, a channel-like region of depleted flux tubes exists in limited local time extent. This is

also substantiated by observational data indicating stronger earthward flows in the center of the magnetotail (Hones et al., 1981). Figure 21 is a schematic illustration of the flow pattern in the magnetotail as suggested by Hones et al. (1981).

With η no longer constant along the back boundary of the RCM, some idea of the contours of constant η is useful before attempting to model the situation. Figure 22 is a suggested schematic of contours of constant η. Here, a 1.0 refers to the fullest flux tube, with 0.5, 0.8, 0.9 (for example) representing contours of constant partially filled flux tubes. In most of the computer simulations, it is arranged for the flux tube content in the center of the tail to be slightly less than half the contents at the flanks of the magnetotail. This is considered in greater detail in Chapter III, where an investigation of the effects of variable particle content in plasma-sheet flux tubes will be discussed using an adapted form of the Rice Convection Model.

2) Implications for Field-Aligned Current

The observation that most region-1 FAC flow on sunward convecting flux tube leads to an interesting hypothesis, when linked to the idea of a limited local time sector of depleted plasma (see sections I.B.3 and II.A.1). Using equation (II.A.2-5) we see how a gradient in number invariant leads to generated field-aligned current. Previously, this has only been used in the inner plasma sheet and ring current region, since it was believed that this was the only region where significant gradients in η existed. Further

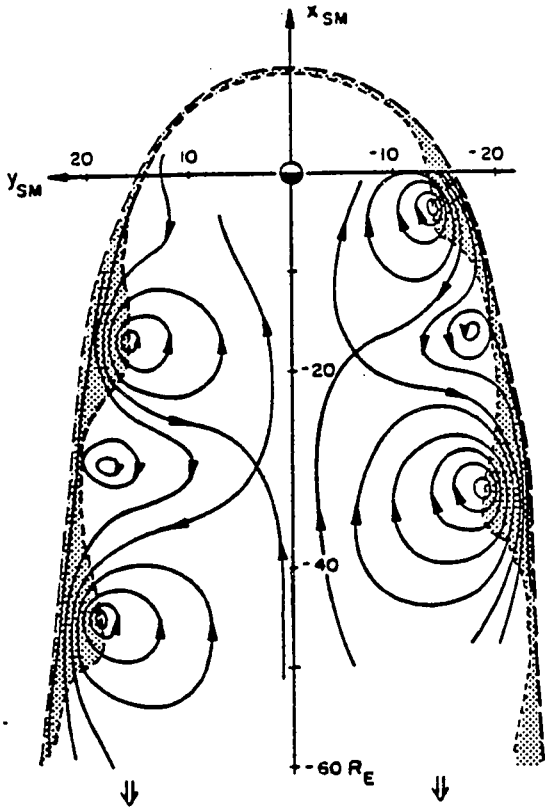

Figure 21. Schematic interpretation of the plasma vortex measurements. The shaded area is the boundary layer, its wavy inner edge indicated by the dotted line. The dashed line represents the magnetopause. The pattern of flow represented by the solid lines moves tailward through the magnetosphere (as indicated by white arrows at bottom) driven by Kelvin-Helmholtz instability at the boundary layer's inner edge. From Hones et al., 1981.

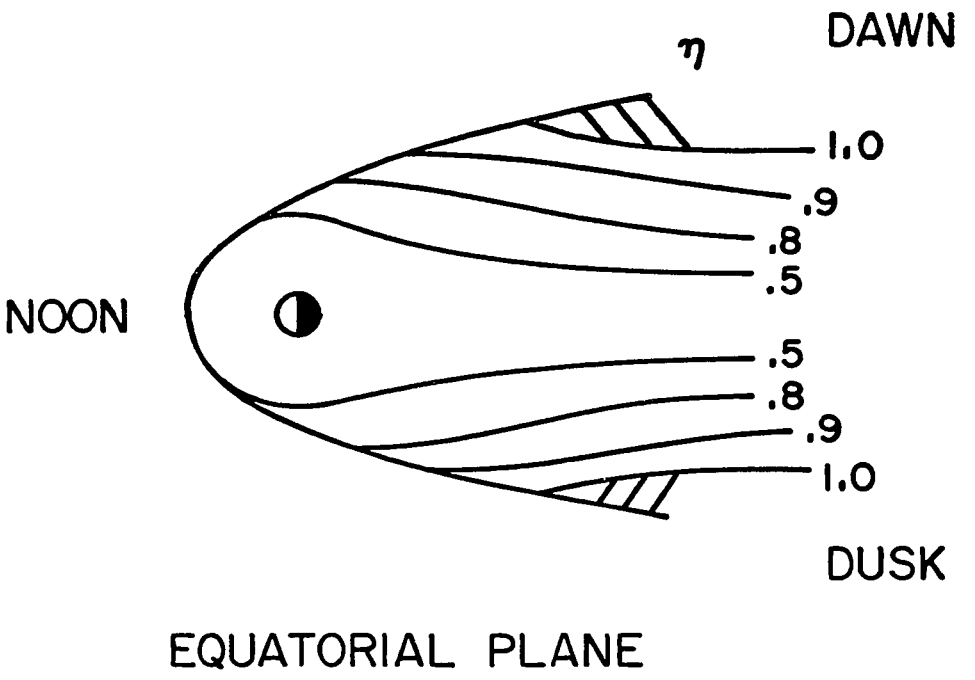

Figure 22. Schematic of contours of constant η in the equatorial plane.

out into the magnetotail (at ~ 20 R_E, for example) if there is a gradient in η directed outward toward the flank, then region-1 sense current is generated as shown in Figure 23. (Some of the region-1 current may still flow on antisunward-moving flux tubes, as has been traditionally proposed to be a boundary-layer generated phenomenon.)

The next section is a general discussion of the method used in the "computer experiments" to investigate the described hypothesis. Chapter III details the computer runs.

C. Method Used in Computer Experiments

1) Energy "Channels"

The RCM has been set up so that twenty-one species are tracked at once. For this adaptation of the RCM, seven of the species are to be assigned to be high energy ions, seven are low energy ions, and seven are electrons. We want to find appropriate energies for these channels.

In the following analysis, we first look at quiet time proton spectra at various distances out in the magnetotail. It is found that the spectra can be approximated by a Maxwellian distribution with the appropriately chosen value of kT_i. We then discuss which two energy channels should be used to approximate the single Maxwellian distribution for ions.

Energy spectra are available from a variety of sources (Hones et al., 1971; Gurnett and Frank, 1974; Akasofu et al., 1973; Hardy

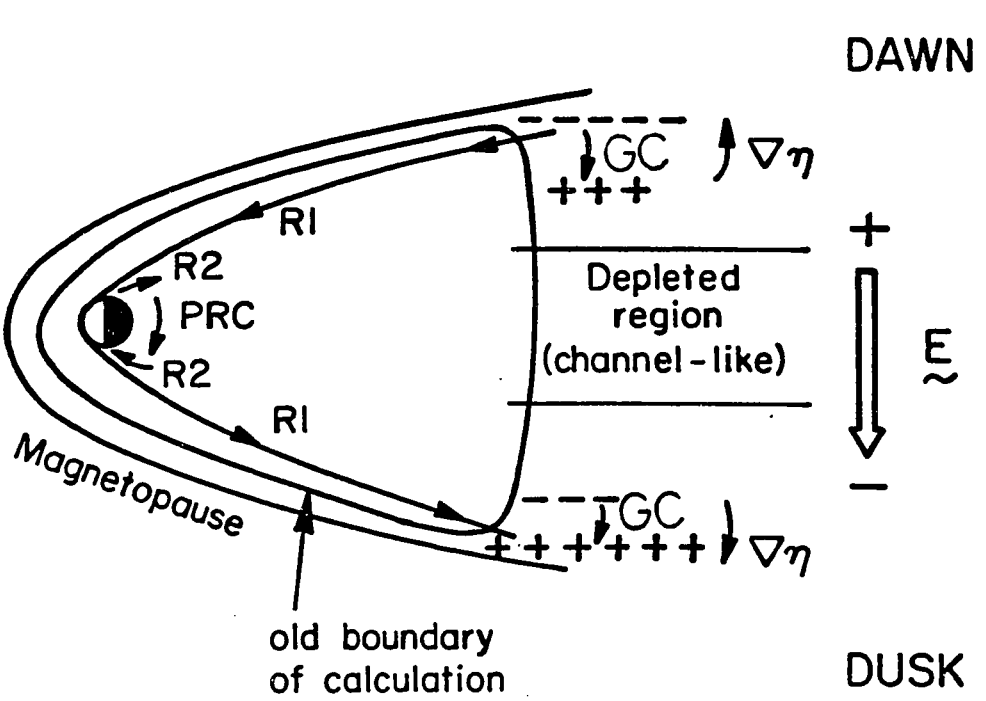

Figure 23. Schematic showing connection of Birkeland currents in the equatorial plane. "R1" means "Region-1 Birkeland Current"; "R2" indicates "Region-2 Birkeland Current"; "PRC" is "Partial Ring Current"; and "GC" represents extra gradient/curvature current through the high-η region on the flanks of the tail.

et al., 1979; Paschmann, private communication, 1982). However, Gurnett and Frank (1974) include plasma sheet proton spectra (energies of ~88 eV to 40 keV) from the Lepedea instrumentation in the IMP 6 spacecraft for quiet time conditions. The spectra included in Gurnett and Frank (1974) are reproduced here and fitted to Maxwellian differential spectrum in Figures 24a,b, and c. There is a Maxwellian-like distribution seen at L ~ 12, 14. The data at L ~ 12 have a much better fit to a Maxwellian than the others at L ~ 8 and 14. Proton energy spectra given by Hones et al. (1971) also display Maxwellian shapes in similar energy ranges. From the fitting analysis of the Gurnett and Frank (1974) data curves it is concluded that $kT_i \sim 2.5$ keV for a distance of ~20 R_E in the magnetotail. This is the approximate distance of the back boundary of the calculation, where an initial (quiet) plasma distribution is needed.

We determine the two ion energy channels by attributing equal energy density to each channel and requiring that the two delta function distributions agree with the Maxwellian with regard to three moments:

$$n_{1i} + n_{2i} = n_i \qquad \text{(II.C.1-1)}$$

$$n_{1i}E_{1i} = n_{2i}E_{2i} = n_i\bar{E}_i/2 \qquad \text{(II.C.1-2)}$$

$$n_{1i}E_{1i}^2 + n_{2i}E_{2i}^2 = n_i\overline{E_i^2} \qquad \text{(II.C.1-3)}$$

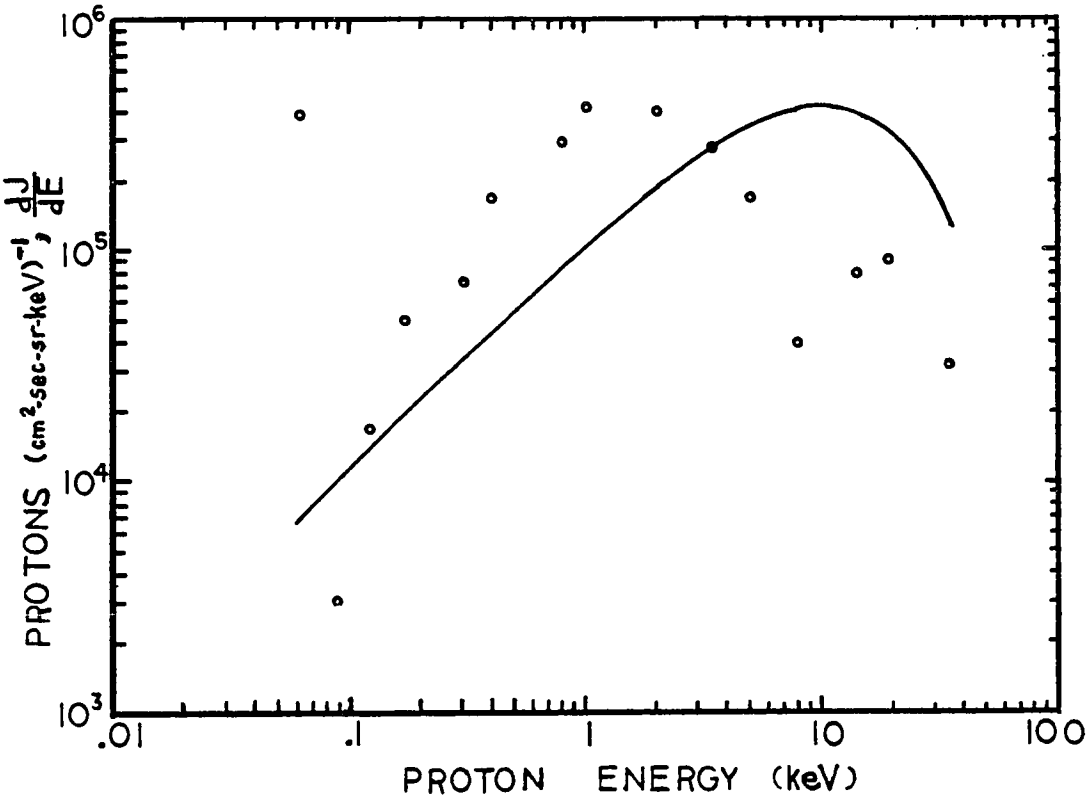

Figure 24(a). Fitting of Maxwellian (no symbols attached) to data (circles) from Gurnett and Frank (1974) for L~8. Theory curve is $\frac{dJ}{dE} \propto Ee^{-E/E_o}$ with E_o=10.0 and constant of proportionality equals 1.2×10^5 $1/cm^2 \cdot sec \cdot sr \cdot (keV)^2$.

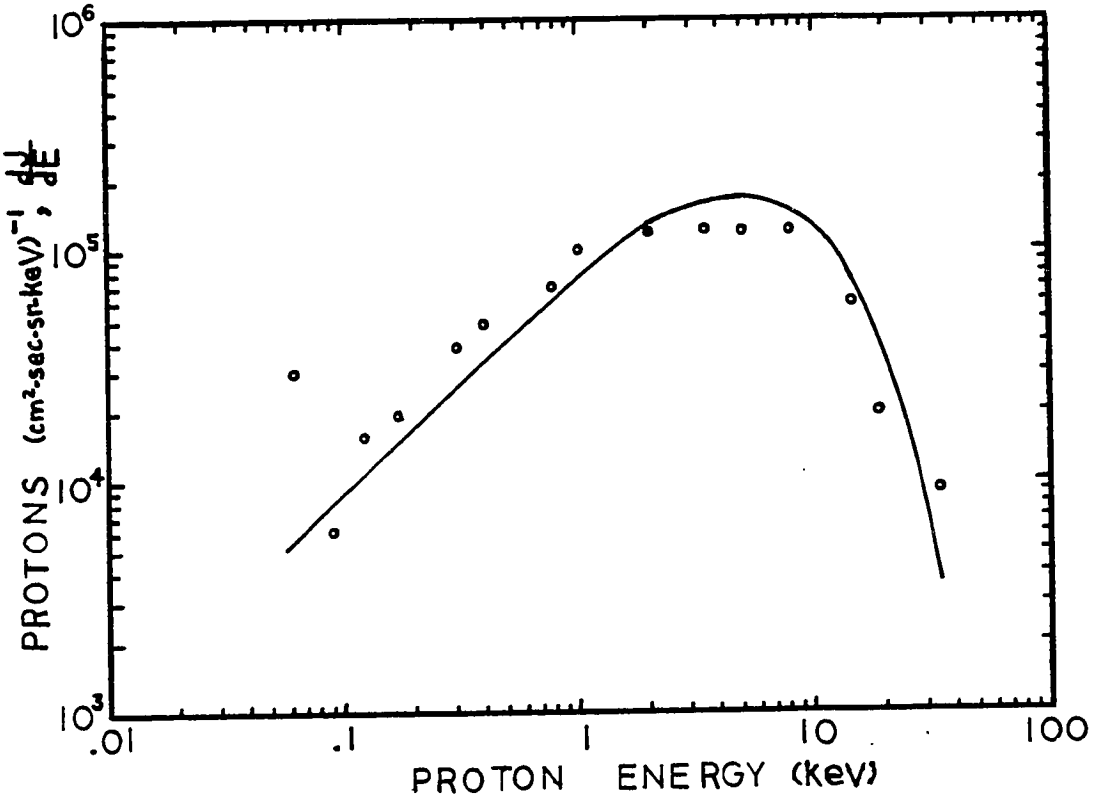

Figure 24(b). Same as Figure 24(a), for L ~12; theory curve is for E_o=5.0 and constant of proportionality equals 9.5×10^4 $1/cm^2 \cdot sec \cdot sr \cdot (keV)^2$.

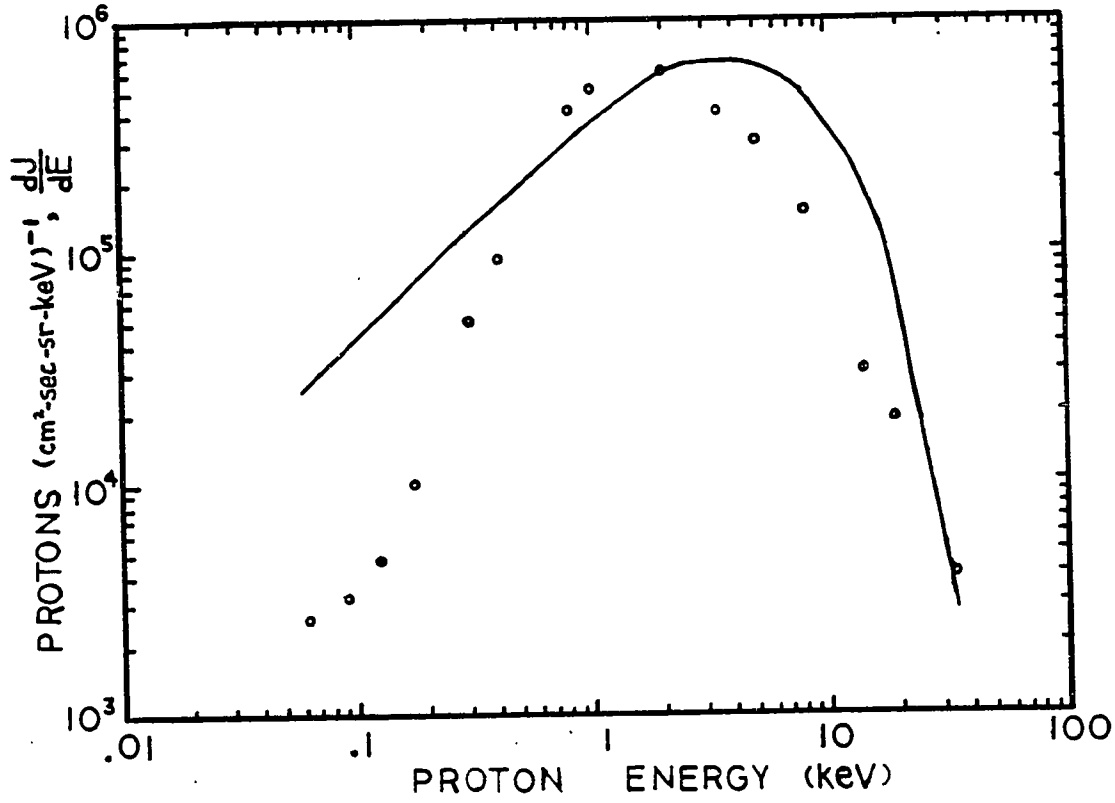

Figure 24(c). Same as Figure 24(a), for L ~ 14; theory curve is for E_o=4.0 and constant of proportionality equals 4.4×10^5 $1/cm^2 \cdot sec \cdot sr \cdot (keV)^2$.

where "i" refers to ions, 1 refers to the high energy ions and 2 refers to the low energy ions. The quantities n_{1i} and n_{2i} represent number of population number densities for the two different ion energy channels. Equation (II.C.1-2) is very different than equations (II.C.1-1) and (II.C.1-3). In this second equation, we assign half the energy content to each channel. We need to find $\overline{E}_i$ and $\overline{E_i^2}$ for the Maxwellian distribution:

$$f(v) = n_i \left(\frac{m_i}{2\pi kT_i}\right)^{3/2} e^{-mv^2/2kT_i}$$

(This is per volume in $\underset{\sim}{x}$-space and velocity-space.) The speed distribution is $g(v)dv = 4\pi v^2 dv f(\underset{\sim}{v})$. (This is now per $\underset{\sim}{x}$-space volume.) In terms of energy:

$$g(E_i)dE_i = (\text{constant})\ E_i^{1/2} dE_i e^{-E_i/kT_i}$$

To calculate $\overline{E}_i$, we evaluate

$$\overline{E}_i = \frac{\int_0^\infty E_i (E_i^{1/2})\ e^{-E_i/kT_i} dE_i}{\int_0^\infty E_i^{1/2}\ e^{-E_i/kT_i} dE_i}$$

obtaining:

$$\overline{E}_i = kT_i \frac{\Gamma(5/2)}{\Gamma(3/2)}$$

With $\Gamma(1/2) = \sqrt{\pi}$ and $\Gamma(z+1) = z\Gamma(z)$, this becomes $\overline{E}_i = (3/2)\ kT_i$, as expected. Using a similar approach for $\overline{E_i^2}$, we

obtain $\overline{E_i^2} = (15/4)k^2T_i^2$. Using equation (II.C.1-1), (II.C.1-2), and (II.C.1-3), we obtain:

$$E_{2i}^2 - \frac{2\overline{E_i^2}}{\overline{E}_i} E_{2i} + \overline{E_i^2} = 0$$

With $\overline{E_i^2} = (15/4)k^2T_i^2$, $\overline{E}_i = (3/2)kT_i$, and solutions of this quadratic, we obtain $E_{1i} = 4.08\ kT_i$, and $E_{2i} = .92\ kT_i$. In the Maxwellian fitting analysis of the Gurnett and Frank (1974) data curves, we obtained $kT_i \sim 2.5$ keV for $R \sim 20\ R_E$. Thus, we have for $R \sim 20\ R_E$, $E_{1i} = 10.2$ keV and $E_{2i} = 2.3$ keV. The paper by Hones et al. (1971) includes plasma sheet proton spectra (energies of ~100 eV to 18 keV) from the Vela satellite, which was at the approximate distance of interest ($R \sim 20\ R_E$) in the magnetotail for our back boundary input parameters. Figure 1 of Hones et al. (1971) is a spectrum for quiet time conditions, and is reproduced here as Figure 25. The two ion energy channels we picked are consistent with this spectrum.

In the spectrum of Figure 25, it is seen that the electron average energy is approximately 1/3 of the average energy of the ions. Various published spectra (see, e.g., Hones et al., 1971) generally exhibit the same behavior. Thus, the electrons are modeled with $\overline{E}_e = (1/3)\ \overline{E}_i = 1.25$ keV.

We have 2 ion energy channels and 1 electron channel; there are 21 species total:

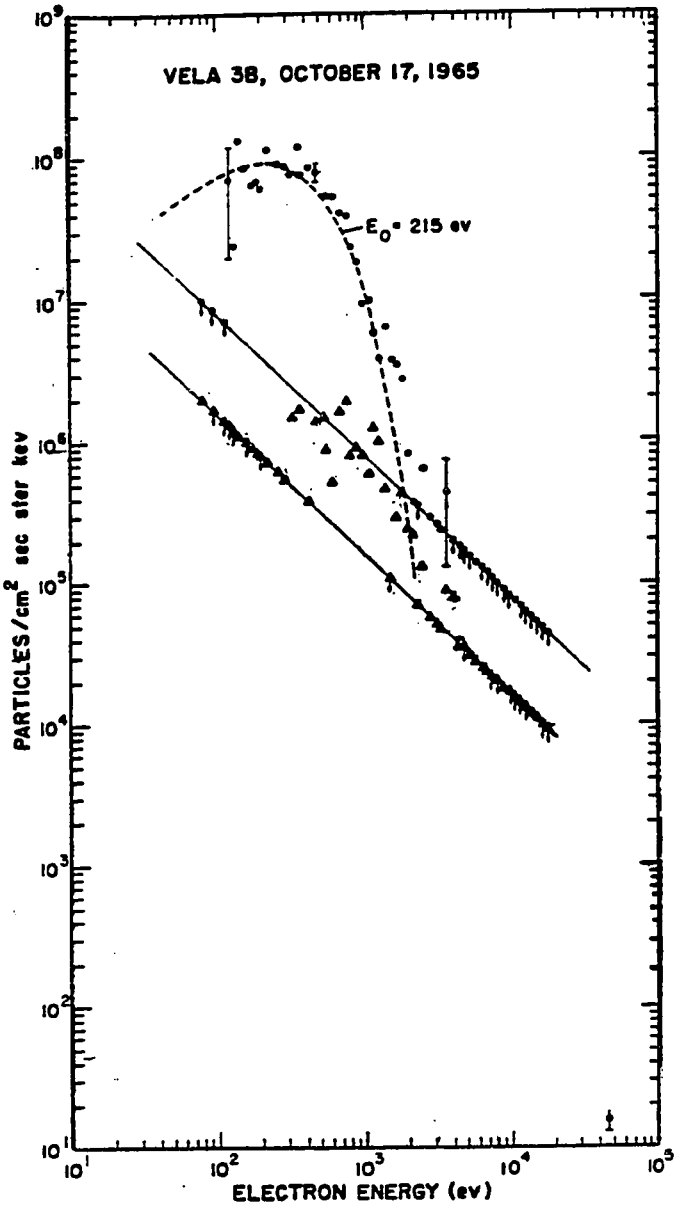

Figure 25. Plasma sheet electron (dots) and proton (triangles) spectra measured by Vela 3B on a very quiet day. From Hones et al., 1971.

$$E_{\text{high ion}},\ k = 1 \rightarrow 7$$

$$E_{\text{low ion}},\ k = 8 \rightarrow 14$$

$$E_{\text{electron}},\ k = 15 \rightarrow 21.$$

The energy invariant, λ, is actually put into the computer simulation. To convert "average energy" to λ, we use the relation $\lambda_k = E_k [\int(ds/B)]^{2/3}$ and a flux tube volume at ~20 R_E from a Voigt model (personal communication, 1982). The values used for energy are: E_{1i} = 10.2 keV, E_{2i} = 2.3 keV, and E_e = 1.25 keV at ~20 R_E, as discussed previously in this section. For flux tube volume we take: $(\int ds/B)^{-2/3} = 0.724\ R_E^{-2/3}\ \gamma^{2/3}$. For the ion temperature chosen, we then have

$$\lambda_1 = 14088$$

$$\lambda_2 = 3177$$

$$\lambda_3 = 1727$$

where 1 is for the high energy ion channel, 2 is for the low energy ion channel, and 3 is for the electron channel. (λ is in units of eV $R_E^{2/3}\ \gamma^{-2/3}$.)

2) Population Level "Channels"

We also have to choose how much plasma to assign to each species. We assume that we have the same total number of ions and electrons.

From equation (II.C.1-2), we obtain:

$$\frac{n_{1i}}{n_i} = \frac{\bar{E}_i}{2E_{1i}} \text{ and } \frac{n_{2i}}{n_i} = \frac{\bar{E}_i}{2E_{2i}}$$

We have $\bar{E}_i$, E_{1i}, and E_{2i} calculated in the previous subsection. From this, we have $n_{1i} = .18\ n_i$, and $n_{2i} = .82\ n_i$, where the total number of ions is calculated below. (For the electrons, $n_{electron} = n_3 = n_i = n$.) Here, we use η, the number invariant for the ions, or electrons (see Chapter I.B.1). We use η_{TOT} based on calculations at the back boundary, which is to be placed at $R \sim 20\ R_E$. We define η_{inner} to be the number invariant for the plasma that is closest to the Earth. These species are originally placed at $\sim 6\ R_E$.

The population levels are set up initially such that small-content flux-tubes are closer to the Earth and larger content flux-tubes are further out in the plasma sheet. We want the η chosen for the region of the plasmasphere at midnight (i.e., η_{inner}) to reflect the notion that the particle energy density is less (by a factor of 0.3) than the magnetic field energy density, since this is the region where the magnetic field lines are nearly dipolar. We therefore take $\beta = 0.3$ in the following calculation for $R \sim 6\ R_E$. For $R \sim 6\ R_E$, we calculate η_{inner} based on $\beta = 0.3$ as follows:

$$\beta = \frac{\text{Particle pressure}}{\text{Magnetic field "pressure"}} = \frac{p}{B^2/2\mu_0}$$

But, $p = nkT/V$, $kT = (2/3)\ \bar{E}$, and $\bar{E}_i + \bar{E}_e = (4/3)\ \bar{E}_i$, so that:

$$\beta = \left(\frac{\eta_{inner}}{\int \frac{ds}{B}} \left(\frac{2}{3} \times \frac{4}{3} \bar{E}_i\right)\right)/(B^2/2\mu_0).$$

Thus,

$$\eta_{inner} = (5.35 \times 10^{18} \text{ weber}^{-1}) \times \frac{B^2}{\bar{E}_i} \left(\int \frac{ds}{B}\right) \text{ for } R \sim 6 \ R_E \quad \text{(II.C.2-1)}$$

[B in γ, $\bar{E}_i$ in keV, $\int(ds/B)$ in R_E/γ]. Values for B, and $\int(ds/B)$ (flux tube volume) are from the chosen magnetic field model, and $\bar{E}_i$ is based on observations of energy spectra. More discussion of the chosen magnetic field, and flux tube volume is presented in the next chapter.

In the magnetotail region, the situation can be viewed as a simple one-dimensional force balance between equatorial particle pressure and tail-lobe magnetic pressure. Therefore, for $R \sim 20 \ R_E$, we take the equatorial particle pressure and the tail lobe magnetic energy density to be equal. With this, we get

$$\eta_{TOT} = (1.79 \times 10^{19} \text{ weber}^{-1}) \frac{B^2}{\bar{E}_i} \left(\int \frac{ds}{B}\right) \text{ for } R \sim 20 \ R_E \quad \text{(II.C.2-2)}$$

[B in γ, $\bar{E}_i$ in keV, $\int(ds/B)$ in R_E/γ]. Again, values for the magnetic field, and flux tube volume are discussed in the next chapter.

With η_{TOT}, and η_{inner} calculated, we need to assign the initial amount of plasma to each step in between. This is done by the following formulation. Here, we are concerned with the

general method of assigning the η_k's. In the next chapter, the actual values used in the computer runs are discussed.

We define f_k to be the fraction of η_{TOT} for each species k (see section I.B.1). We already have assigned an energy invariant, λ_k, for each species, so that there are three energy "channels" (previous section). We now need to assign number invariants, η_k. For the innermost k species, $f_k = \eta_{inner}/\eta_{TOT}$ (see Figure 26). Let this ratio, f_k, be equal to X. The plasma populations are assigned in terms of increments here, with $\sum_{\ell=k+1}^{7} \eta_\ell$ equal to the amount of plasma between the location of the inner edges of the k and (k + 1)th species. An example of the procedure: the plasma population increments are set up for the high energy ion channel so that $f_7 = X$; $f_7 - f_6$, $f_6 - f_5$, $f_5 - f_4 = Y/3$; $f_4 - f_3$, $f_3 - f_2$, $f_2 - f_1 = Z/3$ (see Figure 26). By knowing f_7, and η_{inner}, (and choosing Y or Z) the other 6 η's ($\eta_1 \rightarrow \eta_6$) can be assigned according to the f's ($f_1 \rightarrow f_6$). (Values chosen for X, Y, Z are given in the next chapter. Note that X + Y + Z = 1.0.)

3) Inner Edge Locations

We also need to include initial locations of inner edges for each of the twenty-one species. The exact way in which one spaces the inner edges is not too crucial since they quickly move a substantial amount due to earthward convection. For simplicity, we assume that the high energy ions, low energy ions, and electrons

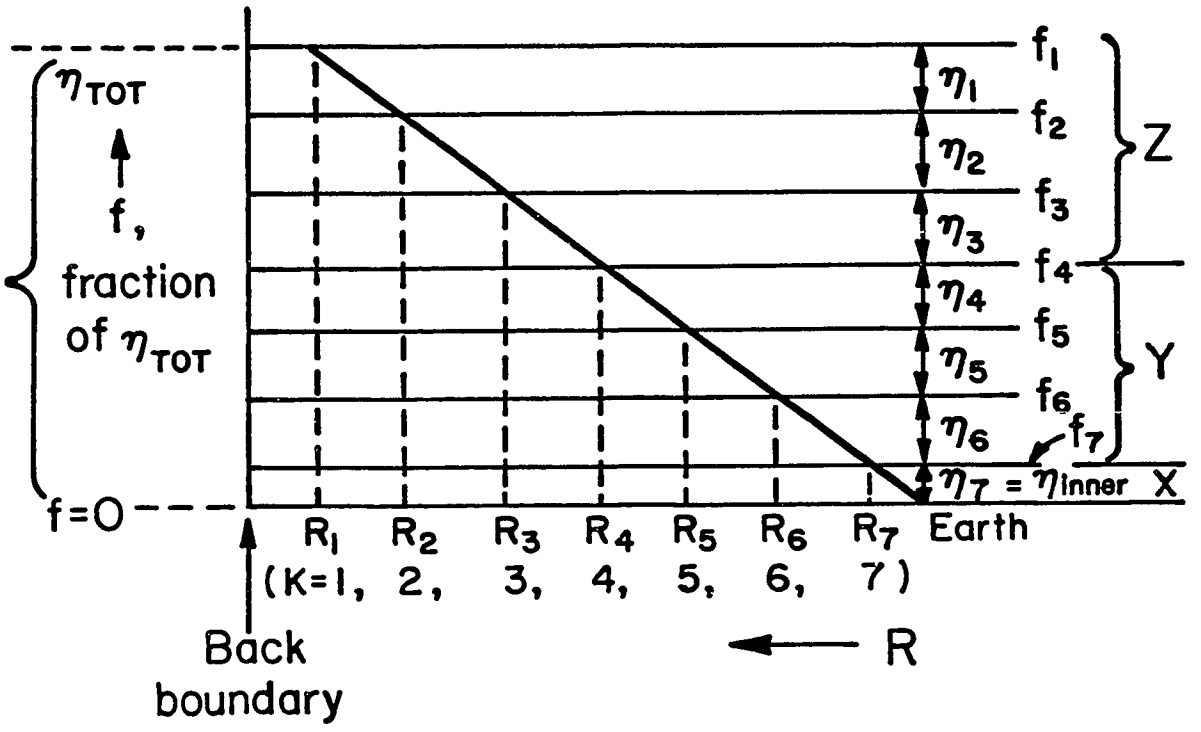

Figure 26. Schematic of setup of inner edges. "Steps" sketched for K=1 through K=7 species. (Illustrated for the high energy ion channel.)

start in the same location. The quantity I we use is the ionospheric grid index in the RCM. It is analagous to the "ρ" coordinate in a flattened polar coordinate system. The RCM grid stystem is discussed by Harel et al. (1981a). This quantity I ~ 1 at magnetospheric equatorial distance ~20 R_E and I ~ 6 at R ~ 6 R_E. Basically, I increases as R decreases. We approximate the curve in Figure 26 by

$$f = e^{-(I-1)/I_0} \text{ which is } I = 1 - I_0 \ln f \qquad \text{(II.C.3-1)}$$

I_0 is found by use of equation (II.C.3-1) with f and I for R ~ 6 R_E, which is the innermost initial inner edge location.

4) General Comments on Inputs to the RCM

As discussed above, initial energy channels, population level channels, and inner edge locations are needed as inputs to the RCM, so that the initial plasma distribution is given. These are varied as appropriate for the desired computer experiment.

Other inputs needed for the modified RCM are the polar boundary potential distribution, the conductivity model, and magnetic field model. The conductivity model and magnetic field model are discussed in the next chapter. The model for the potential is similar to that given in Appendix 2 of Harel et al. (1981a) except that there is more potential concentrated in the channel-like section of the tail (and the throat region [see Harel et al., 1981a] is slightly smaller). Before, 20 kV was distributed between dawn

(MLT ~ 6) and dusk (MLT ~ 18) to represent the quiet time cross-tail potential drop. Except where indicated, for the runs in this dissertation, the 20 kV potential drop is now distributed between Magnetic Local Times of ~ 21 and 3. This is consistent with greater flows (and lower plasma density) in the channel-like portion of the tail (see, e.g., Hones et al., 1981), since this assumes greater electric field in the limited local time sector. The chosen polar boundary potential distribution is discussed further in the next chapter.

III. COMPUTER SIMULATION

A. Specific Inputs

In section II.C, the general method to be used in the computer "experiments" was discussed. In the present section, we discuss the choice of specific population levels, and inner edge locations. Also discussed are the conductivity model and polar boundary potential distribution.

For the population levels, we have $\eta_{inner} = 9.33 \times 10^{19}$ $(weber)^{-1}$ from equation (II.C.2-1), with $B_e = 149\ \gamma$, and $\int ds/B = 2.34 \times 10^{14}\ m^3/weber$ from a magnetic field model discussed by Voigt (1981). We also have $\eta_{TOT} = 1.23 \times 10^{21}\ (weber)^{-1}$ from equation (II.C.2-2) with $B_{lobe} = 12.6\ \gamma$ and $\int ds/B = 1.04 \times 10^{16}$ $m^3/weber$. (Values for the magnetic field and flux tube volume from one form of the Voigt model are shown by Erickson and Wolf [1980].) From the discussion in section II.C.2, we obtain

$$\eta_7 = 1.68 \times 10^{19}\ (weber)^{-1}$$
$$\eta_6 = 3.06 \times 10^{19}\ (weber)^{-1}$$
$$\eta_5 = 3.06 \times 10^{19}\ (weber)^{-1}$$
$$\eta_4 = 3.06 \times 10^{19}\ (weber)^{-1}$$
$$\eta_3 = 3.76 \times 10^{19}\ (weber)^{-1}$$
$$\eta_2 = 3.76 \times 10^{19}\ (weber)^{-1}$$
$$\eta_1 = 3.76 \times 10^{19}\ (weber)^{-1}$$

(We chose X = 0.08, Y = 0.41, Z = 0.51.) Note that we have ~17% of the particles in the outermost step, and ~51% of the particles in the outermost three steps.

We get the initial inner edge locations from equation (II.C.3-1) as:

$$I(1) = 1.0 \qquad (R_1 \approx 19\ R_E)$$
$$I(2) = 1.4 \qquad (R_2 \approx 17\ R_E)$$
$$I(3) = 1.9 \qquad (R_3 \approx 14\ R_E)$$
$$I(4) = 2.5 \qquad (R_4 \approx 12\ R_E)$$
$$I(5) = 3.1 \qquad (R_5 \approx 10\ R_E)$$
$$I(6) = 4.1 \qquad (R_6 \approx 8\ R_E)$$
$$I(7) = 6.3 \qquad (R_7 \approx 6\ R_E)$$

Next, we need to discuss the conductivity and polar boundary potential distribution. The conductivity model is the same as the one previously used in the RCM and described in Harel et al. (1981a). It is briefly described below. The conductivity model includes the effects of photoionization by sunlight, as well as the effects of auroral electron precipitation. The sunlight effect is described by Harel et al. (1981a, p. 2234). Equations (9) and (10) of Harel et al. (1981a) were used in the RCM to infer auroral conductivity enhancements from electron fluxes and average energies measured by the S3-2 satellite. The total conductivity was obtained by summing the contributions from auroral enhancement, photoionization, and base-level night side values, according

to equations (A.20) and (A.21) of Harel et al. (1981a).

The boundary potential is similar to the one previously used in the RCM and described by Harel et al. (1981b). The boundary potential (V_b) used here is as follows:

$V_b = - V_0 \sin 2\psi$	Near Noon, $10 \lesssim$ MLT $\lesssim 14$
$V_b = - V_0$	Dusk, $15 \lesssim$ MLT $\lesssim 19$
$V_b = - V_0 \sin (\psi - 2\Delta\psi)$	Night time sector, $20 \lesssim$ MLT $\lesssim 22$
$V_b = - V_0 \sin (\psi - 3\Delta\psi)/2$	Near midnight (dusk), MLT $\sim$ 23
$V_b = 0$	Midnight, MLT $\sim$ 24
$V_b = - V_0 \sin (\psi + 3\Delta\psi)/2$	Near midnight (dawn), MLT $\sim$ 1
$V_b = - V_0 \sin (\psi + 2\Delta\psi)$	Night sector (dawn), $2 \lesssim$ MLT $\lesssim 4$
$V_b = + V_0$	Dawn, $5 \lesssim$ MLT $\lesssim 9$

where ψ is measured eastward from noon, $\Delta\psi = (2\pi/28)$ and V_0 is a constant which is estimated by using data concerning the cross-tail potential drop. (Specifically, V_0 is half the potential drop across the polar boundary.) In the simulation, V_0 starts at 10 kV and remains at this value until an hour before substorm onset, but then gradually increases to 28 kV just before onset (growth phase). In the hour after onset, the boundary potential continues to increase gradually until V_0 reaches 40 kV. The quantity V_0 remains at this value throughout the rest of the simulation (expansion and recovery stages).

Next, we discuss the possible time dependence for variable flux tube content.

B. When is Variable Flux-Tube Content Important?

One important point which has not yet been addressed is the following: should η be taken as variable at the back boundary (in the RCM) only when the substorm expansion phase is being modeled, or is it variable all the time? Observations indicate that region-1 FAC flows substantially equatorward of the electric field reversal both during substorms and in quiet times for dawn-dusk passes or night-time-sector observations (Heelis et al., 1980; Smiddy et al., 1980; Doyle et al., 1981; Shuman et al., 1981). Statistical studies (e.g., Mozer et al., 1980) normally include both quiet and active times. The best way to model this effect would be to monitor the relative positions of region-1 FAC and electric field reversal during the course of a specific substorm. Observations of the relative positions of region-1 FAC and electric field reversal during the course of one substorm would be difficult to monitor. The clearest signatures of FAC and electric field reversal patterns are available for periods during which there is a strong southward IMF. This is because the clearest region-1/region-2 Birkeland currents are observed during periods when IMF $B_z \lesssim 0$ and convection is strong. When there is a strongly northward IMF, complex Birkeland current patterns are observed (Smiddy et al., 1980). The plausibility arguments presented in section II.A. seem to imply that the depleted channel will exist most of the time, since it provides a stable configuration for the magnetosphere.

There have been no statistical studies of observations to determine whether this phenomenon of region-1 current generated on sunward convecting flux tubes occurs to a greater extent during the substorm expansion phase. (See the discussion in section V.B.) Therefore, the RCM was run for several different cases. Run 1 considers variable η at the boundary all the time and runs 2, 3, and 4 consider an even greater variation in η at the boundary after onset of the expansive phase.

Variation in η at the back boundary is simulated by "holding back" appropriate species of particles. For run 1, we hold back 17% of the particles. The flux tube content in the center of the tail is then ~83% of the content in the flanks. In run 1, this same "holding back" procedure is used all the time, and particles are held back by pinning the outermost species for each energy channel (K = 1, 8, 15) at the back boundary (I = 1, R $\approx$ 20 R_E) for a night time sector of MLT $\approx$ 22 to MLT $\approx$ 2. In runs 2 to 4, for an hour after onset, we hold back the K = 1, 2, 3, 8, 9, 10, 15, 16, 17 species, so that 51% of the particles are held back. For K = 1, 8, 15, these particles are held back in the night time sector of MLT $\approx$ 20 to 4. For K = 2, 9, 16, they are held back in the sector from MLT $\approx$ 21 to 3. For K = 3, 10, 17, these particles are held back in the sector of MLT $\approx$ 22 to 2. Before onset, runs 2 to 4 and run 1 are the same. In runs 2 to 4, after onset, we use the more complicated "hold back" procedure for an hour, but then use the original run 1 hold-back procedure for the last 2 hours.

C. Self Consistency of the Magnetic Field

It should be remarked that no completely self-consistent magnetospheric magnetic field model presently exists for a realistic three-dimensional situation. The aim of the following set of computer "experiments" was to assess the sensitivity of the results to the specific magnetic field models chosen.

During the expansive phase of the substorm, the magnetotail is known to become more dipolar in a sector near midnight (section I.A.3). To model this phenomenon, at the onset of the substorm (for runs 3 and 4), some experiments were performed with the magnetic field. Figures 27a and 27b show magnetic field models corresponding to "nominal" plasma population and "depleted" plasma population, respectively. These magnetic field models and displays are from Voigt (private communication, 1982). In runs 1 and 2, the nominal magnetic field was used throughout. In order to make the magnetic field model consistent with the channel configuration (i.e., "holding back" procedure), a hybrid magnetic field model was interpolated between the nominal and depleted models for runs 3 and 4. From MLT ~ 4:00 past noon to 20:00, the hybrid and nominal models are the same. For MLT ~ 20:00 and MLT ~ 4:00, the hybrid model is 80% of the nominal model and 20% of the depleted model. For MLT ~ 21:00 and MLT ~ 3:00, the hybrid model is 50% of the nominal model and 50% of the depleted model. For MLT ~ 22:00 and MLT ~ 2:00, the hybrid model is 20% of the nominal model and 80% of the depleted model. For MLT between 22:00 past midnight to

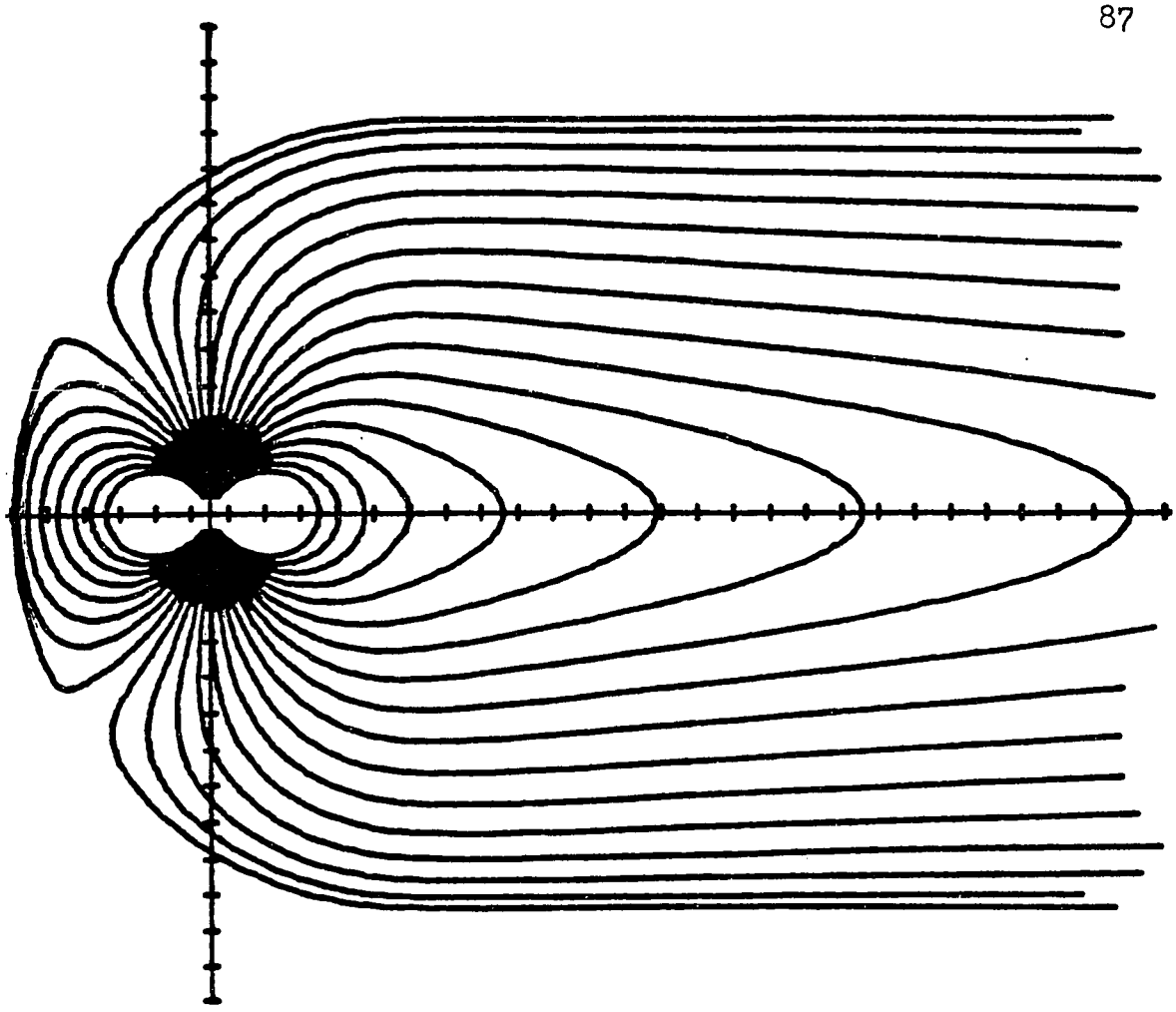

Figure 27(a). Nominal magnetic field model used for runs 1 and 2. Tick marks are at 1, 3, 5 R_E, etc. The field lines start at 66° latitude and there are 2° of difference in latitude for subsequent field lines. The sun is to the left in this noon-midnight meridian cross section. From Voigt (personal communication, 1982). See Table 1.

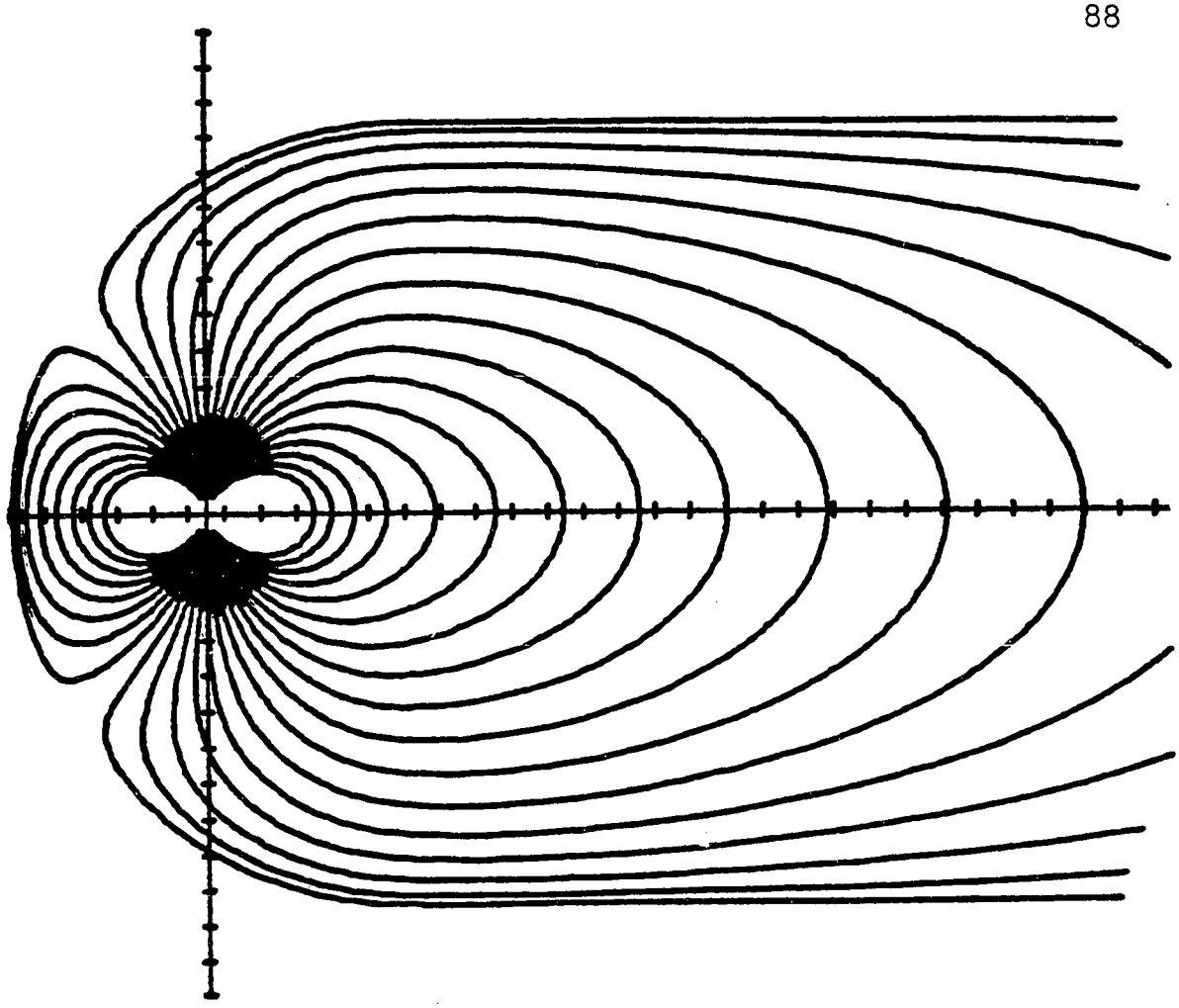

Figure 27(b). Depleted magnetic field model used for part of runs 3 and 4. See Figure 27(a) for format of figure. From Voigt (personal communication, 1982).

2:00, the hybrid and depleted models are the same. The interpolation was set up so that it would roughly coincide with the simulation of the channel region (i.e., "hold back" procedure) discussed in the previous section.

Three runs were performed for the period 1000 to 1300 UT, the three hours after substorm onset, in the situation where additional plasma was held back for the first hour after onset (see section III.B and Table 1). The first time (run 2), the nominal field was used. The second time (run 3), the hybrid magnetic field was used. The third time (run 4), the hybrid magnetic field was used for the first hour after onset, and the nominal field was used for the last two hours of the event. The basic results concerning the generation of region-1 Birkeland current are unaffected by the differences in the magnetic field models. (See the next section on results.)

D. Results

1) Overview

This subsection presents a general survey of the runs performed. According to the discussion in section III.B, four major runs were completed. Table 1 summarizes these runs.

In order to allow the system to come to equilibrium before the beginning of the growth phase (0900 UT), the simulation is started at 0500 UT. That is, the time development of the model from 0500 UT to 0900 UT represents the model coming to equili-

TABLE 1. Computer Simulation Runs

Computer Run	Percentage of plasma held back	Magnetic Field Model
1	17% throughout (Runs 1 to 4 are the same until 10:00 + ε, onset).	Nominal throughout.
2	51% from 10:00 + ε to 11:00 UT; 17% from 11:00:30 to 13:00 UT.	Nominal throughout.
3	Same as run 2.	Hybrid (takes depleted channel into account) for 10:00 + ε to 13:00 UT.
4	Same as run 2.	Hybrid for 10:00 + ε to 11:00 UT; Nominal for 11:00:30 to 13:00 UT.

brium, not the actual time variations of the magnetosphere in that period.

The next subsections show inner edge locations through the event along with equipotential plots, and Birkeland current plots. Birkeland current is displayed in three ways. First, a detailed display for a constant MLT, showing the latitudinal dependence of Birkeland current is presented. Second, global plots which can be compared to Iijima and Potemra plots are presented. Last, the local time dependence of Birkeland current strength is presented.

2) Inner Edge Locations through the Event

Figure 28 shows the initial assumed inner edge locations. The high energy ions, low energy ions and electrons were all assumed to start at the same locations for simplicity. Each of the seven different curves refers to a different population level for the same energy invariant. Note that the outer boundary is almost out to 20 R_E, which approximately doubles the distance of the tailward boundary previously used by the Rice Convection Model (see Harel et al., 1981a).

Figures 29a,b, 30, and 31a,b display the inner edge locations at 0800 UT, three hours after the start of the computer simulation. Inner edges that started at $L \gtrsim 10$ all drifted sunward from their original locations. The solid curve at ~15 R_E at dawn and dusk is the boundary of the calculation.

Figure 29a displays the high energy ions (λ = 14088), corresponding to an energy of 32.7 keV at ~10 R_E. As in Figure 28, each

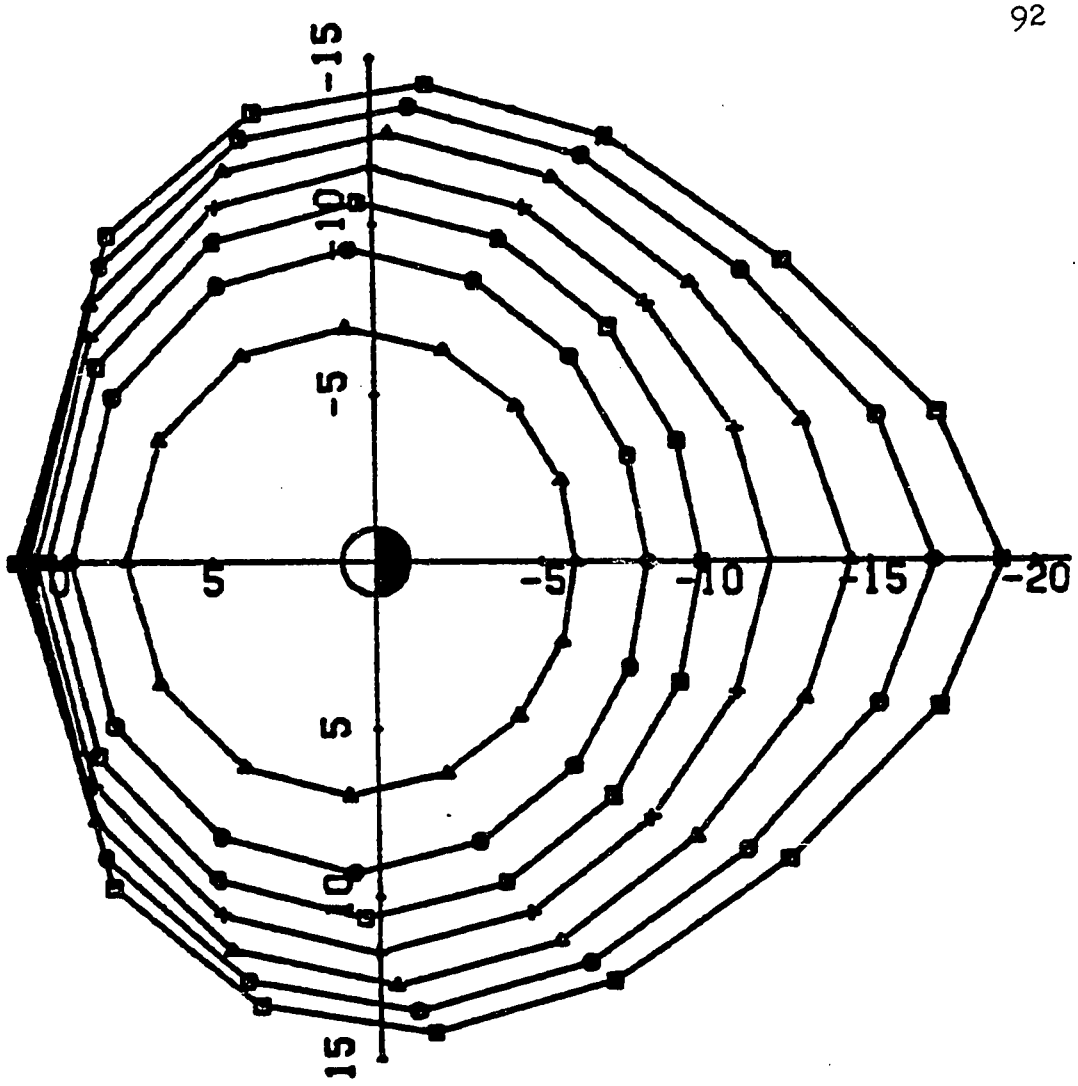

Figure 28. Initial plasma inner edge locations, in the equatorial plane. (The sun is to the left). UT = 5:00. K = 1 (or 8, or 15) is the outermost inner edge. K = 7 (or 14, or 21) is the innermost inner edge.

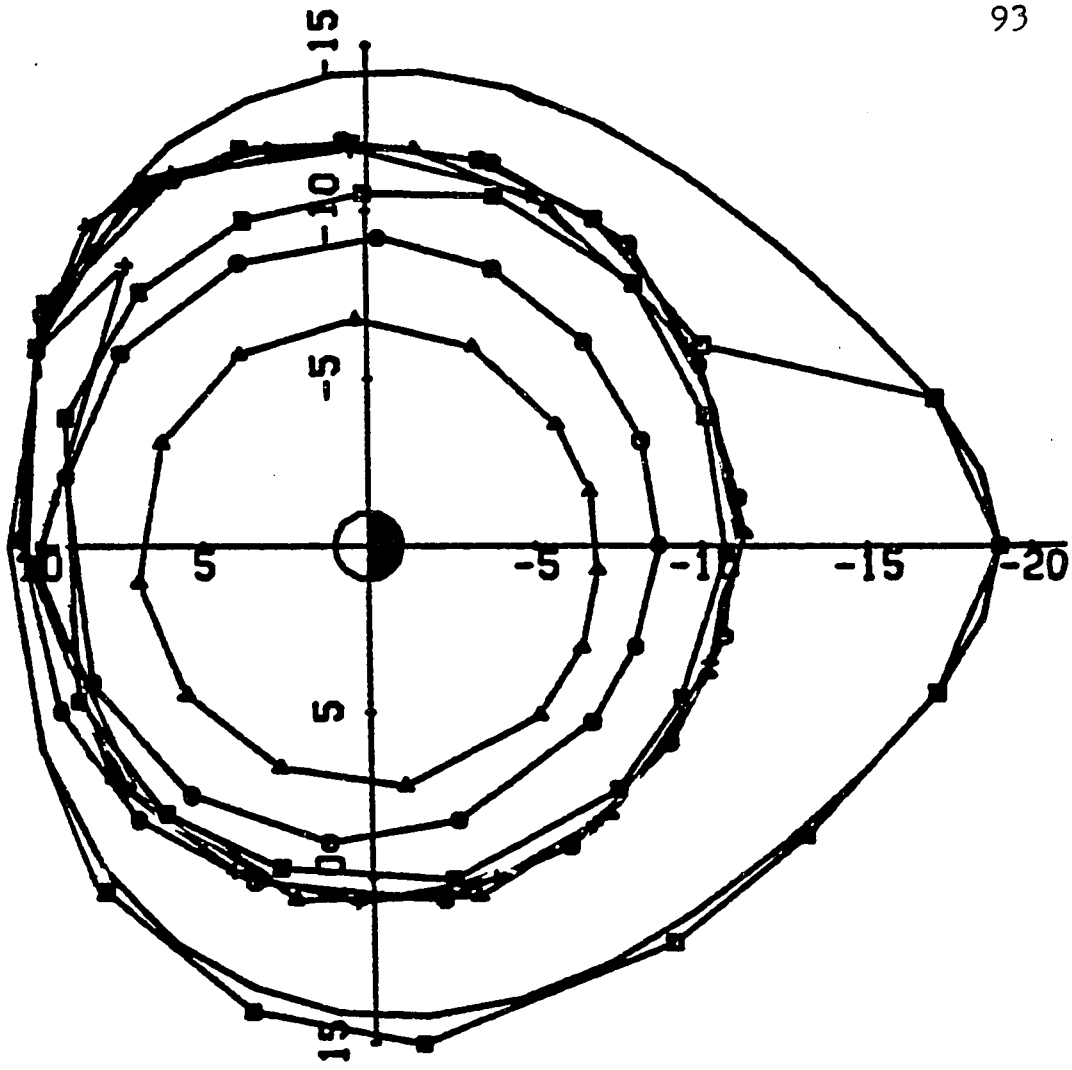

Figure 29(a). Location of inner edges computed three hours after the initial starting condition for the high energy ions. UT = 8:00. K = 1 is the outermost inner edge. K = 7 is the innermost inner edge.

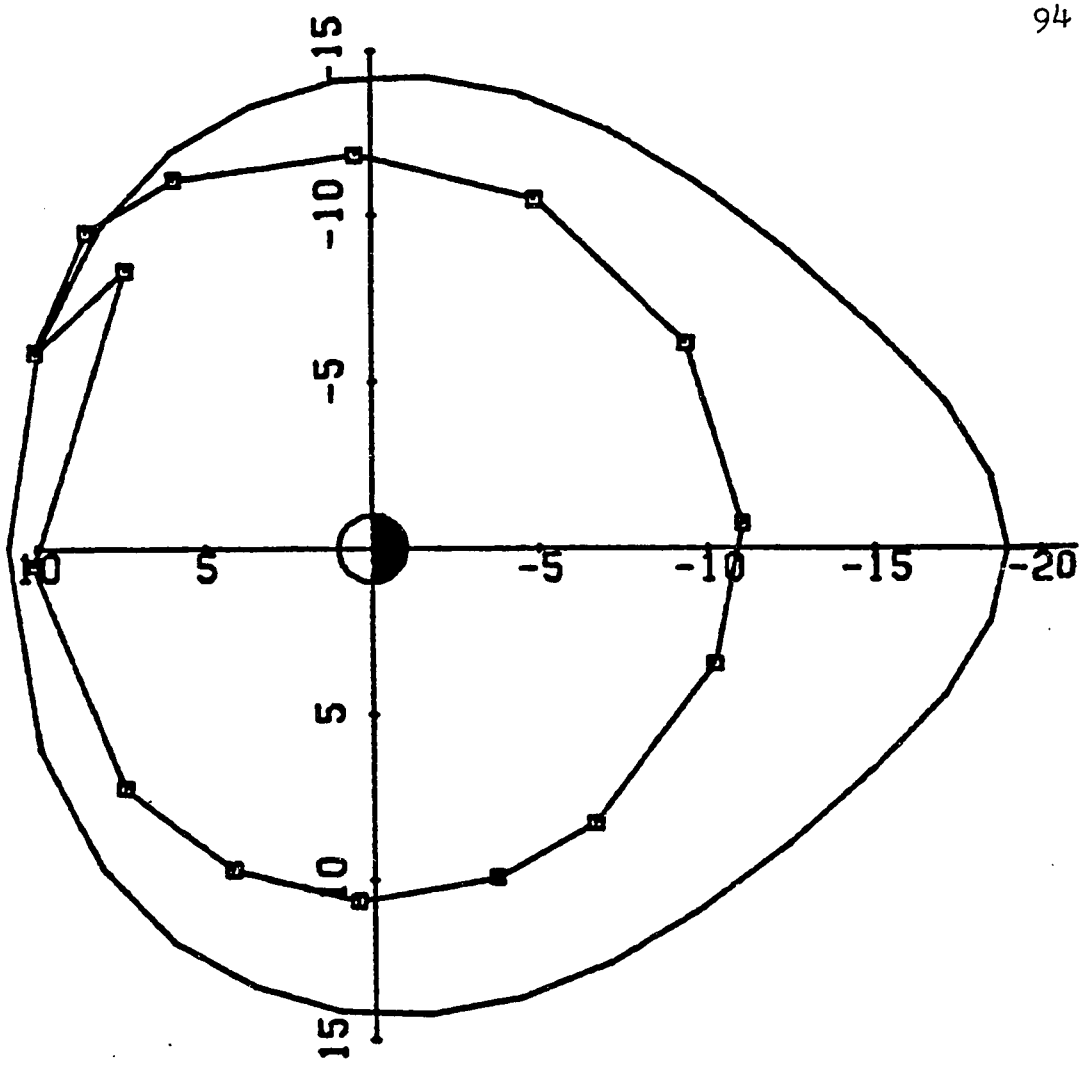

Figure 29(b). Location of inner edge computed three hours after the initial starting condition for high energy ion species K = 4. Inner edge shows tongue formation. UT = 8:00.

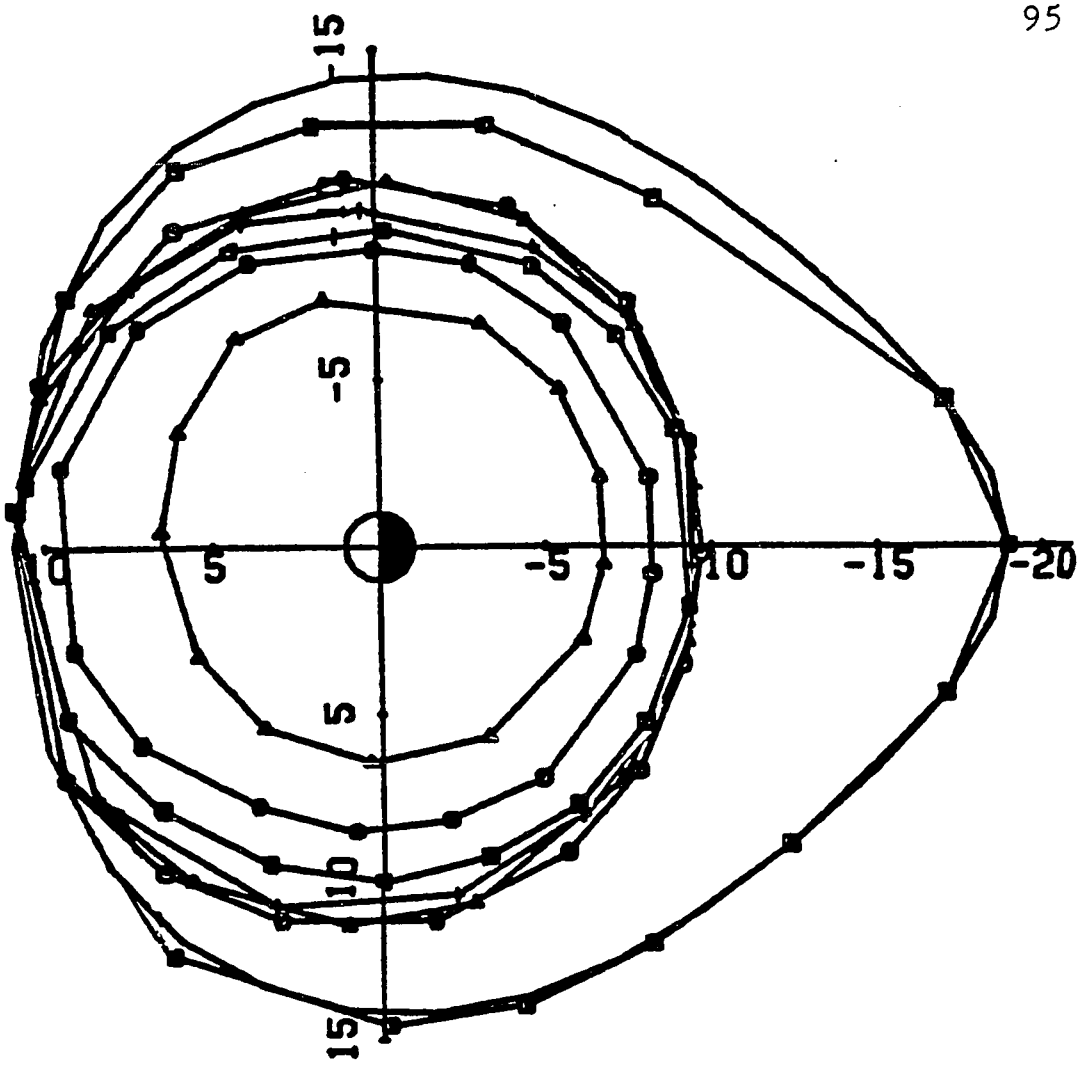

Figure 30. Location of inner edges computed three hours after the initial starting condition for the low energy ions. UT = 8:00. K = 8 is the outermost inner edge. K = 14 is the innermost inner edge.

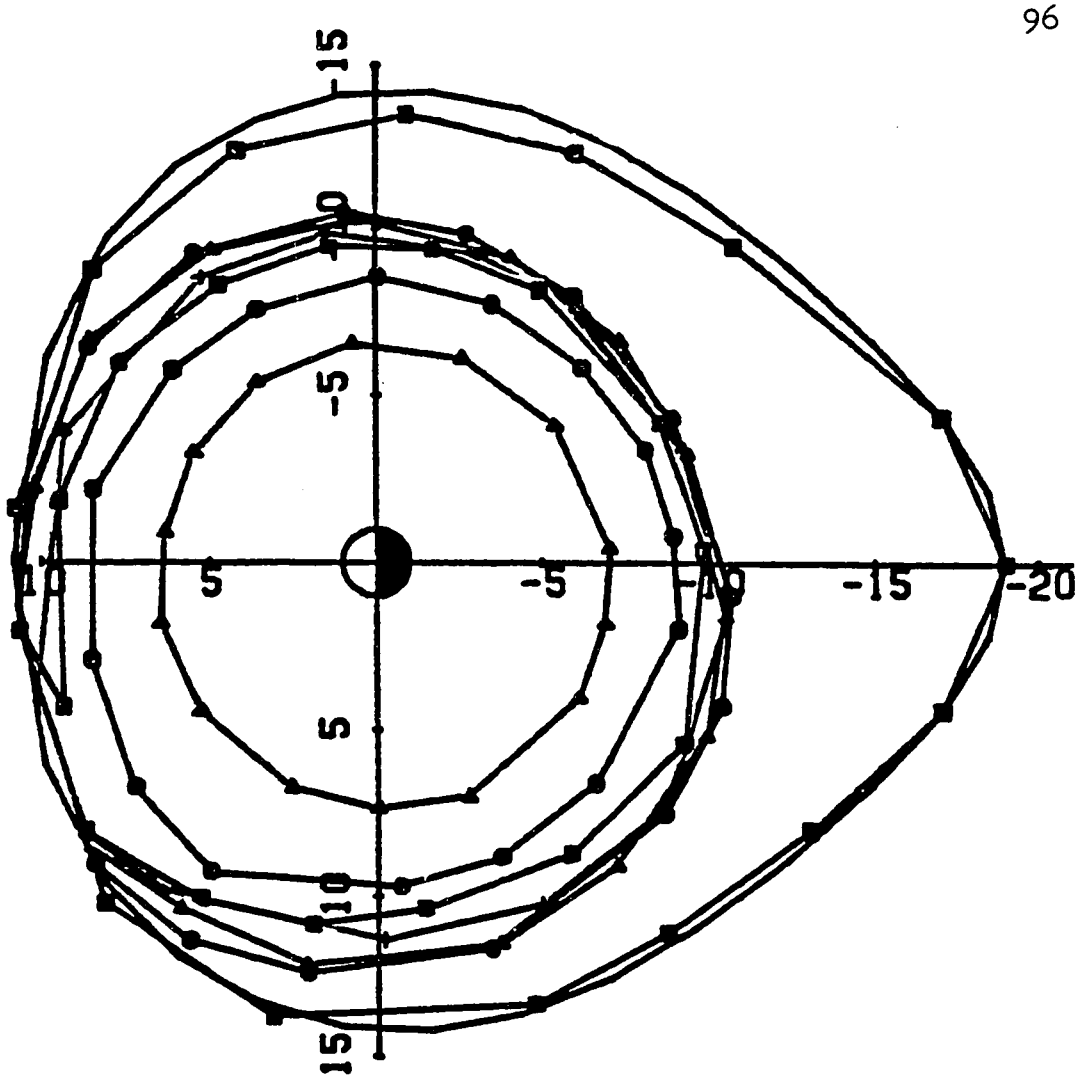

Figure 31(a). Location of inner edges computed three hours after the initial starting condition for the electrons. UT = 8:00. K = 15 is the outermost inner edge. K = 21 is the innermost inner edge.

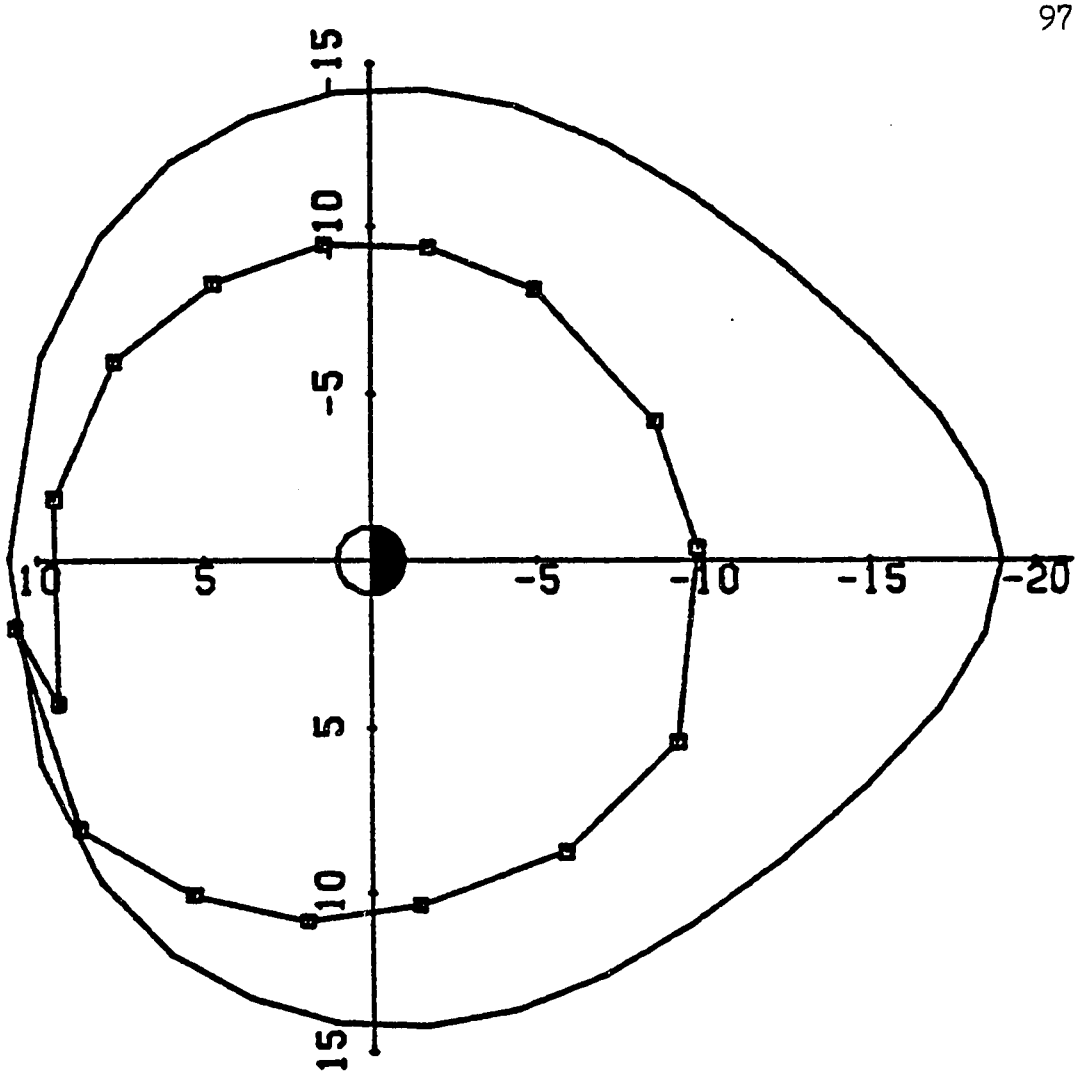

Figure 31(b). Location of inner edge computed three hours after the initial starting condition for electron species K = 19. Inner edge shows tongue formation. UT = 8:00.

of the seven different curves in Figure 29a refers to different population level "inner edges." In Figure 29a, the outermost inner edge (which is held at the boundary from MLT ≈ 22 to 2) displays a "skewing" due to westward gradient and curvature drift.

Figure 30 displays the low energy ions (λ = 3177) corresponding to an energy of 7.4 keV at ~10 R_E. The outermost "inner edge" does not come as close to the Earth near dawn as it did for the high energy ion channel, since the gradient and curvature drift are smaller as a result of the reduced energy invariant.

In Figure 31a, the inner edges for the electrons (λ = 1727), corresponding to an energy of 4.0 keV at ~10 R_E, are shown. For electrons, the gradient and curvature drifts are eastward. Since the energy invariant is relatively small, this effect is not dramatic, as it is in Figure 29a.

In Figures 29b and 31b, note the formation of inner edge forms resembling "tongues." The tongues of plasma or plasma "tails" persist throughout the simulated event. In Figure 31b, this tongue is just beginning to form. For electrons, there is a tongue of eastward-drifting particles (since gradient-curvature drift is eastward for electrons). In Figure 29b, this tongue is also just beginning to form. This is a westward-drifting tongue of particles (since for ions, gradient/curvature drift is to the west). Generally, inner edge forms are more complicated and form fastest for the high energy ions.

Note the formation of a clear "inner edge" at ~10 R_E in Figures 29a, 30, and 31a. The innermost, lowest-flux-tube-content

species (K = 6, 7 in Figure 29a, for example) remain separate, and represent rings of trapped ring-current plasma. The species representing higher flux tube content that are not held back (K = 2, 3, 4, 5 in Figure 29a, for example) approach each other and pile up at a well defined "inner edge" at R ~ 10 R_E, with a substantial density jump. The formation of well-defined inner edges has already been seen (Harel et al, 1981a; Wolf et al., 1982). For a certain species, the quantity $\lambda_k \eta_k$ is uniform anti-earthward of an inner edge, and is equal to zero earthward of an inner edge. It is reasonable that the higher energy, higher flux tube content particles tend to stay farther out than the lower energy, lower flux tube content particles. The held back species (K = 1 in Figure 29a, for example) remains at the modeling boundary in order to enforce a gradient in flux-tube content at the tailward boundary of the calculation.

Figures 32a,b,c display the inner edge locations at 1100 UT (10 minutes after the peak of the substorm) for run 1. Comparing this to Figures 29a, 30, and 31a, it can be seen that as time progresses, plasma sheet particles are injected close to the Earth. The inner edges continue to move sunward with time. The inner edges of the high and low energy ions drift around to the dusk flank. The inner edges of the electrons drift around to dawn. Thus, plasma sheet particles are being injected sunward and around the flanks to form a partial ring current at ≈ 6 to 8 R_E.

Along with inner edge plots, it is useful to also look at effective potential plots. We plot these since they show instan-

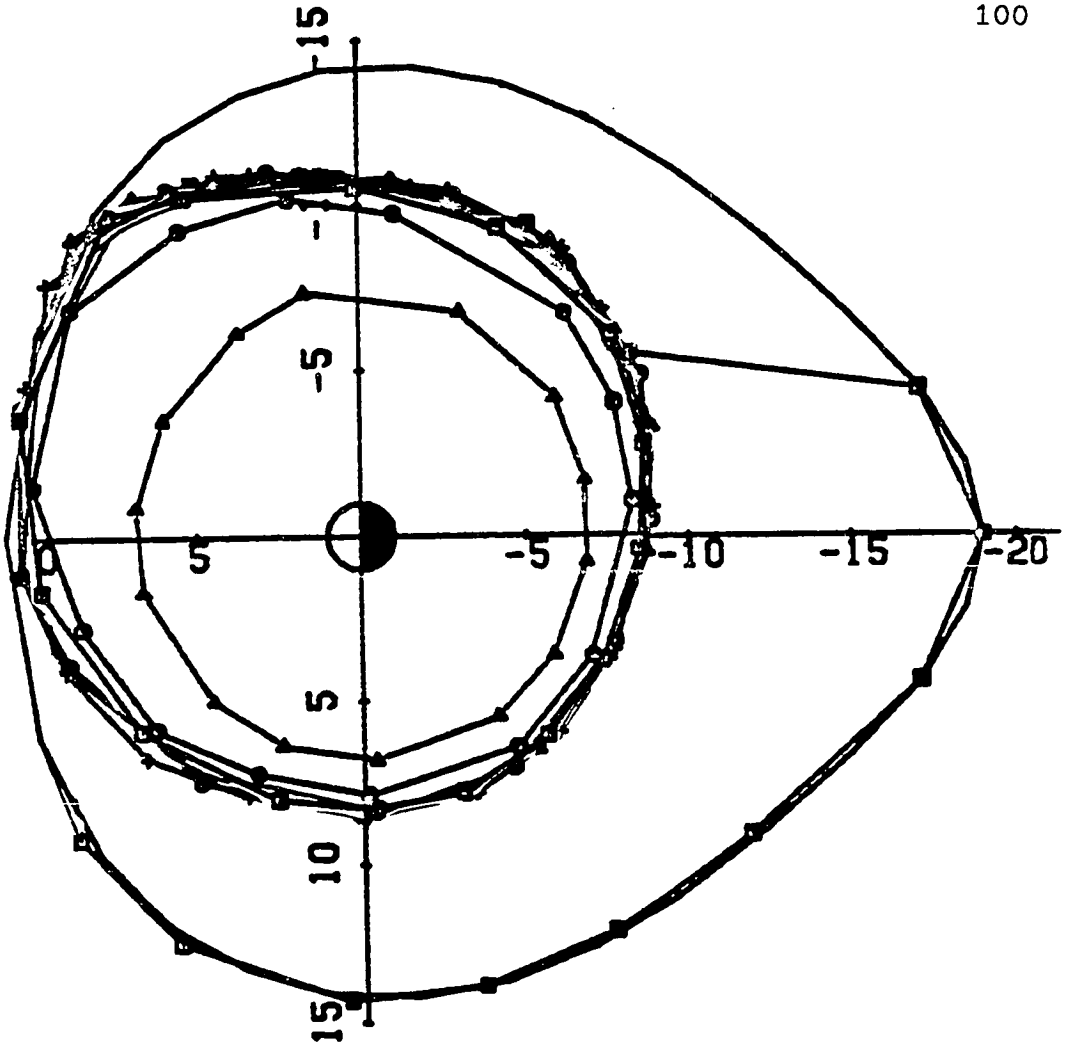

Figure 32(a). Location of inner edges computed ten minutes after the peak of the substorm for the high energy ions (run 1). UT = 11:00. K = 1 is the outermost inner edge. K = 7 is the innermost inner edge.

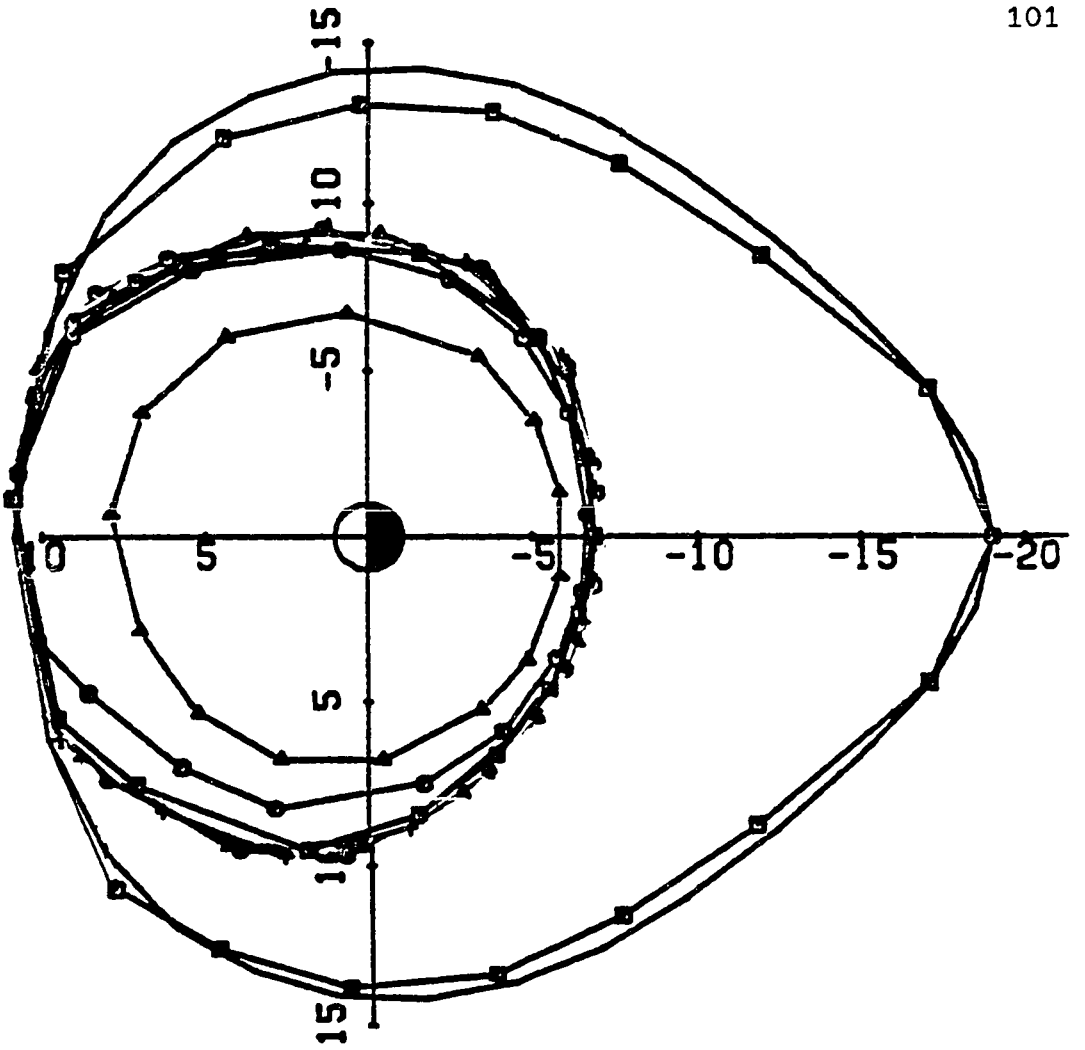

Figure 32(b). Location of inner edges computed ten minutes after the peak of the substorm for low energy ions (run 1). UT = 11:00. K = 8 is the outermost inner edge. K = 14 is the innermost inner edge.

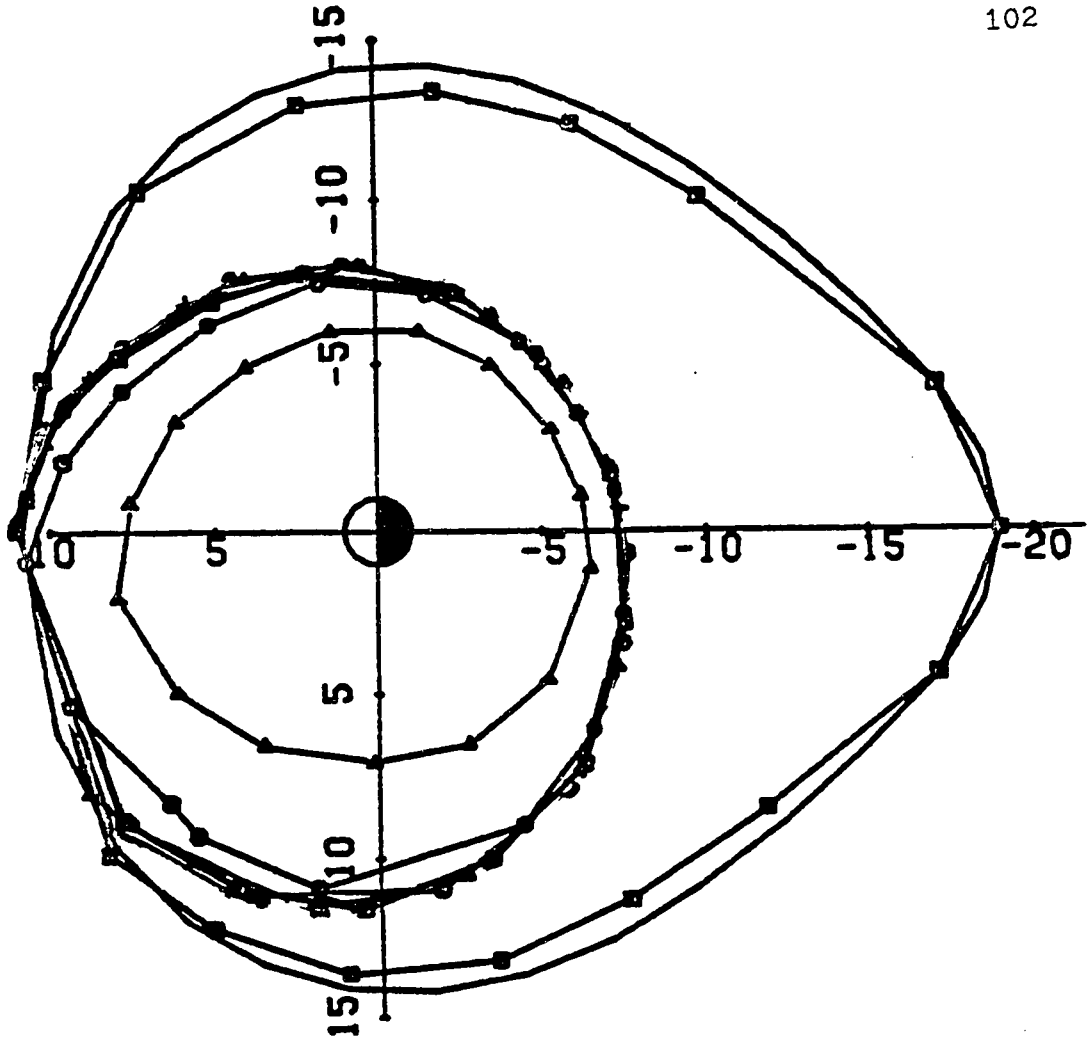

Figure 32(c) Location of inner edges computed ten minutes after the peak of the substorm for the electrons (run 1). UT = 11:00. K = 15 is the outermost inner edge. K = 21 is the innermost inner edge.

taneous trajectories. That is, we plot contours which result from a combination of corotation, gradient, and curvature drift, and the potential directly found from solution of the differential equations (i.e., $V_{cor} + (\lambda/q)\ (\int ds/B)^{-2/3} + V$).

All four of the runs previously mentioned are the same until substorm onset. In Figures 33a,b,c effective potential plots are shown for the three energy species for UT = 1050 (which is near the peak of the substorm) for run 1. Figure 33d shows potential contours, without corotation or gradient and curvature drift effects for UT = 1050 for run 1. Figures such as these (Figures 33a,b,c) showing effective potential contours are to be understood as a competition of the terms mentioned above. For example, the ion potential contours are more spread out near dawn, and closer together near dusk. This is a result of the competition between eastward convection and westward drift at dawn. At dusk, there is westward convection and westward drift. For electrons, the potential contours are more spread out near dusk, and closer together near dawn. This is a result of the competition between westward convection and eastward corotation at dusk. At dawn, there is eastward convection and eastward corotation.

The potential pattern (Figure 33d) at UT = 1050 shows some electric field shielding equatorward of the inner edges, which are at $\sim 10\ R_E$. This phenomenon and the general potential shape has been seen before in previous runs of the RCM (see, for example, Harel et al., 1981a).

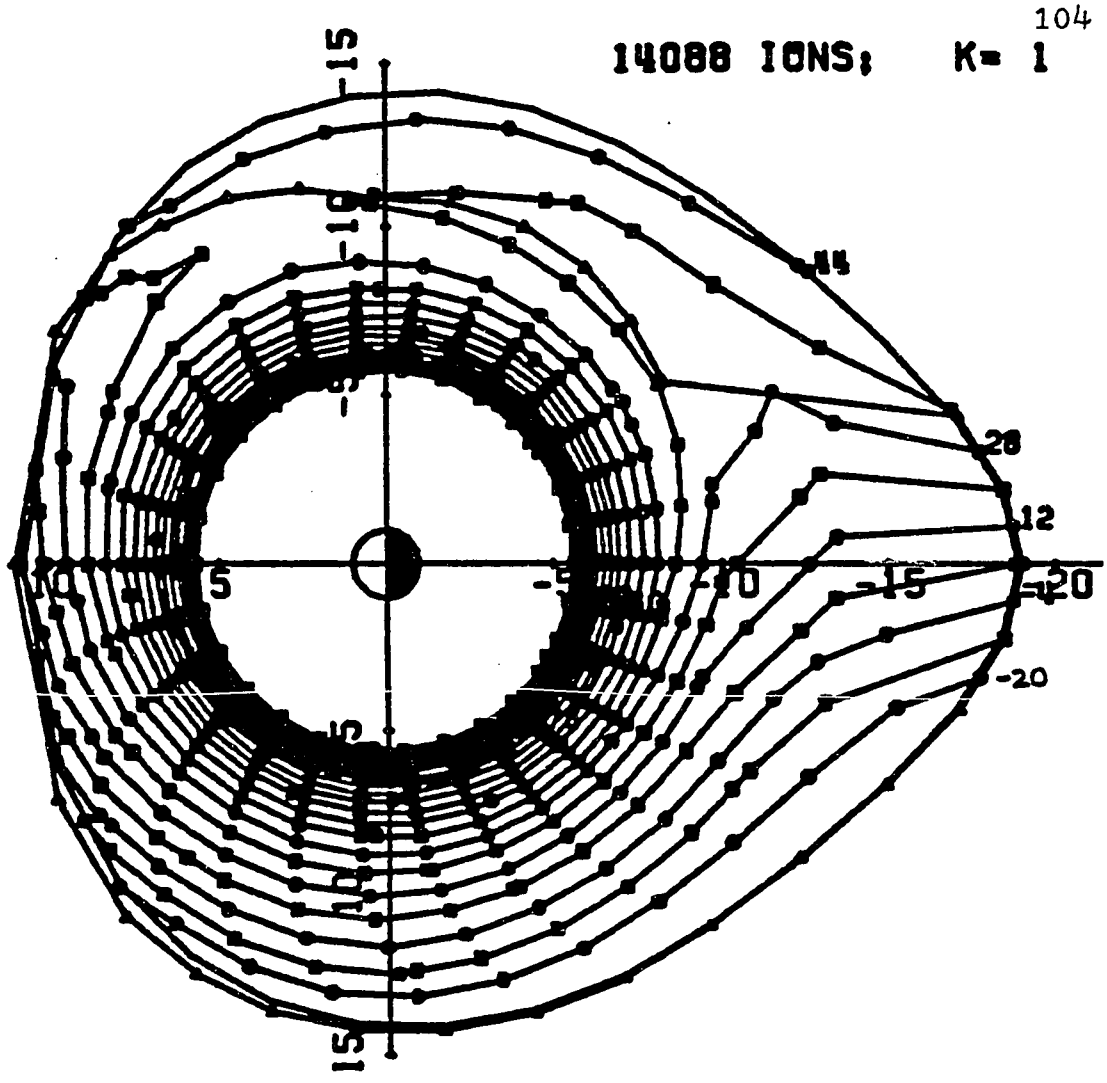

Figure 33(a). Effective potential contours (with corotation) in the equatorial plane at 10:50 UT for the high energy ions for run 1. Equipotentials are 8 kV apart.

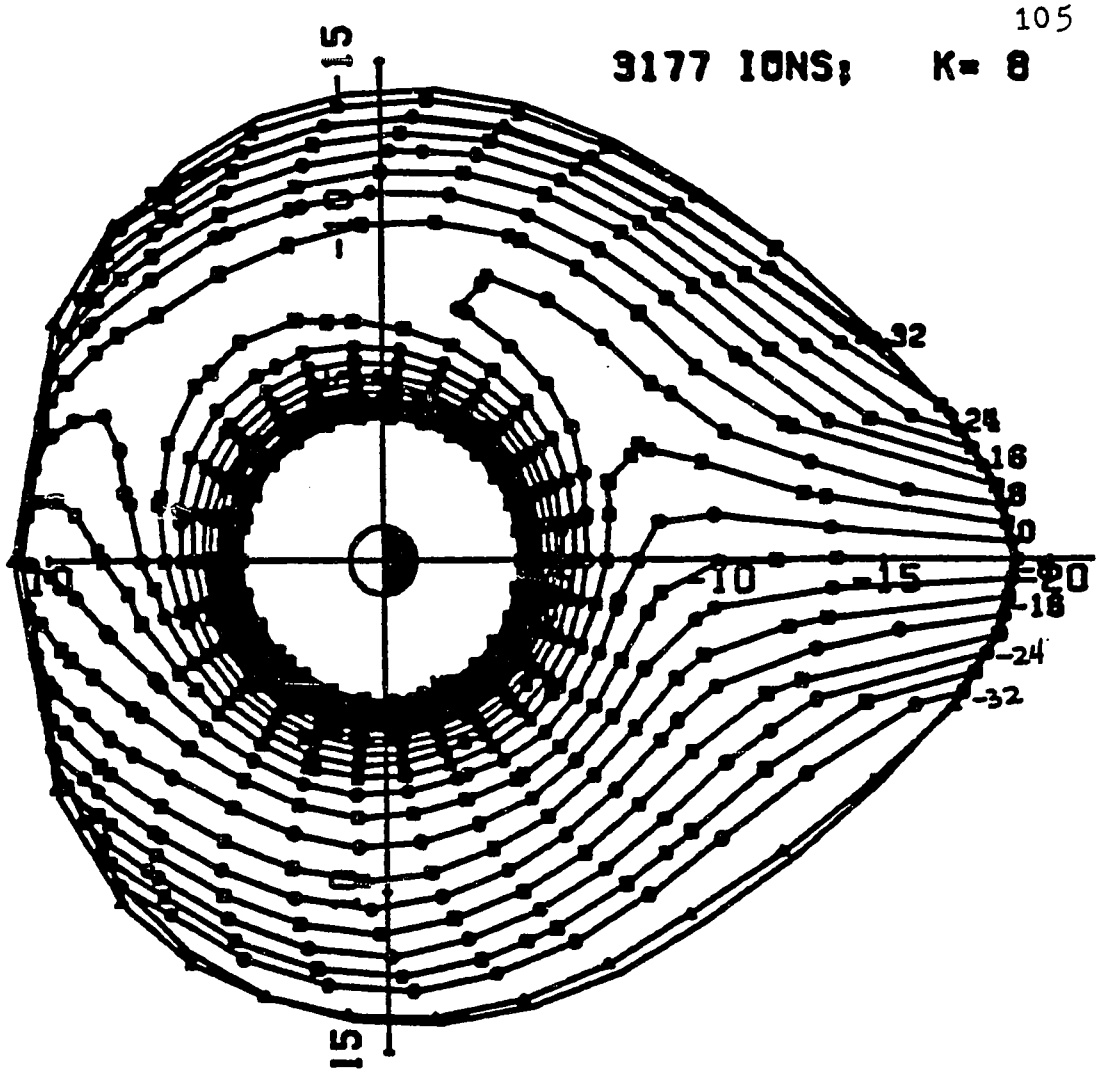

Figure 33(b). Effective potential contours (with corotation) in the equatorial plane at 10:50 UT for the low energy ions for run 1. Equipotentials are 4 kV apart.

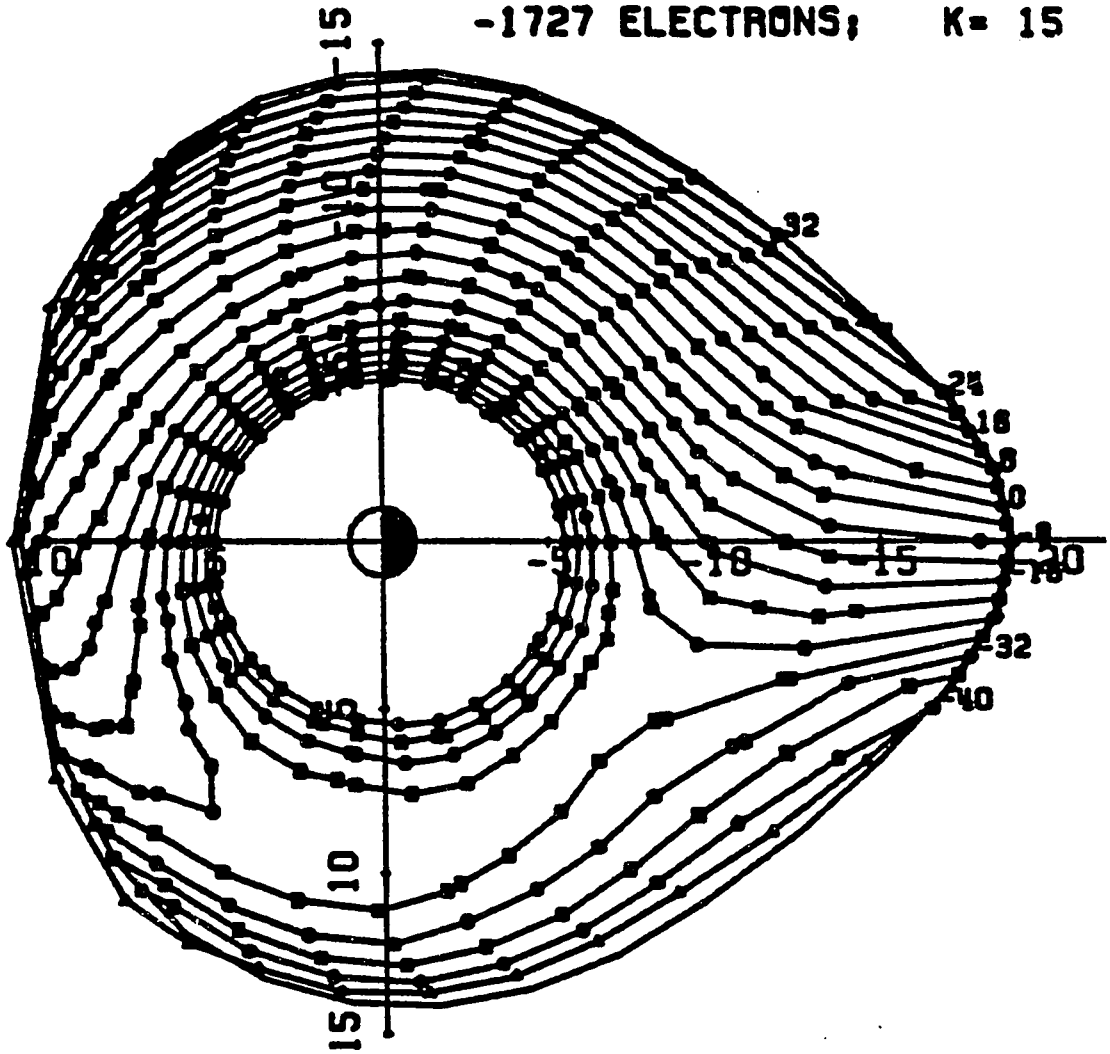

Figure 33(c). Effective potential contours (with corotation) in the equatorial plane at 10:50 UT for the electrons for run 1. Equipotentials are 4 kV apart.

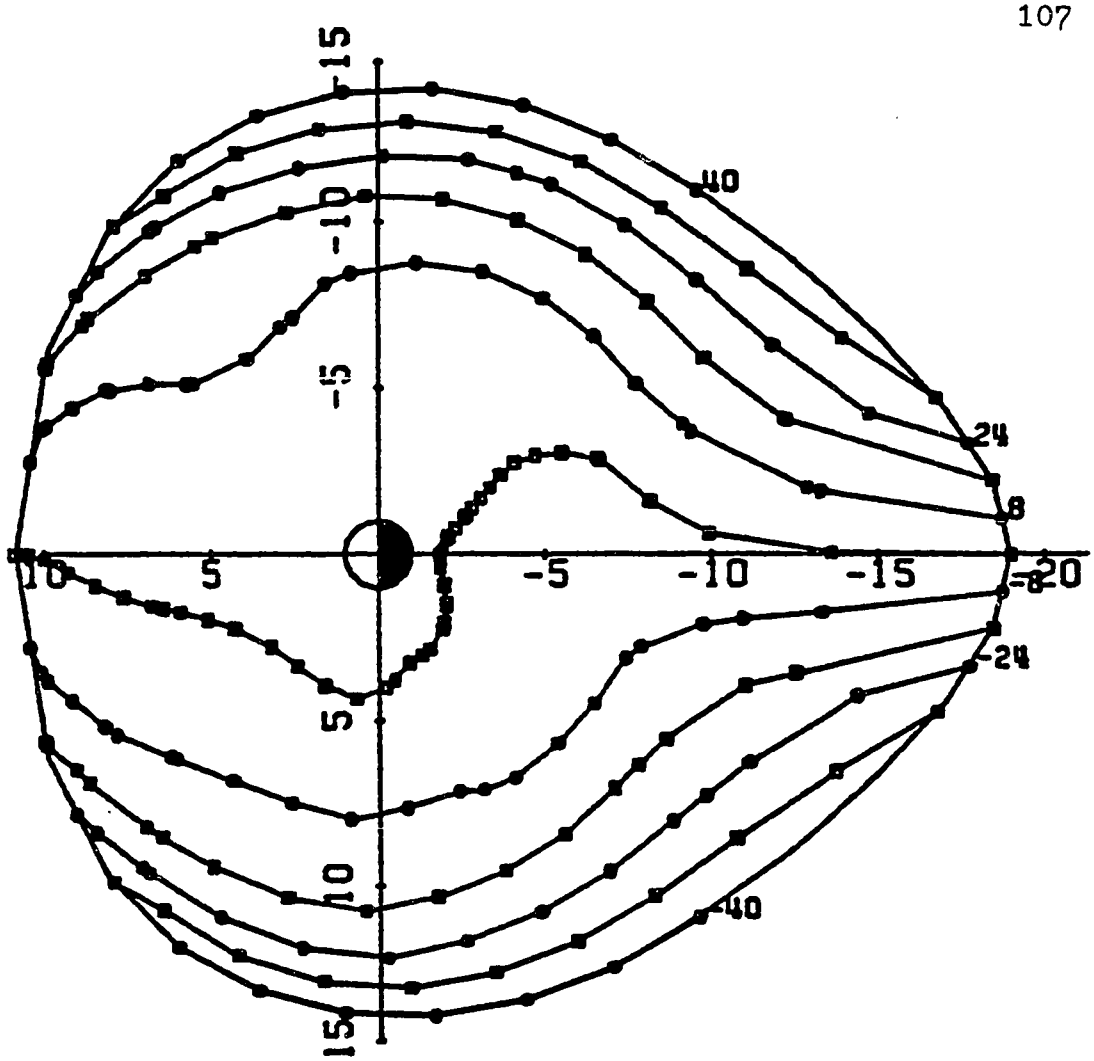

Figure 33(d). Potential contours (without corotation) in the equatorial plane at 10:50 UT for run 1. Equipotentials are 8 kV apart.

Figures 34a,b,c,d present potential contours for runs 1, 2, 3, and 4, respectively, for the high energy ions for 1300 UT, which is during partial recovery. Note that the different magnetic fields in runs 2 and 3 (Figures 34b and c) result in little difference in potential contour plots. Figure 34d (run 4) was a run with the hybrid field for an hour, and then back to the nominal field. The potential pattern for this run (4) is very similar to runs 2 and 3. Furthermore, Figures 34 a and b (runs 1 and 2) are also very similar. That is, potential contours look roughly alike, regardless of the additional 34% of plasma held back from 1000 + ε UT to 1100 UT for run 2. Figures 34e,f,g,h show potential contours, without corotation or gradient and curvature drift effects for UT = 1300, for runs, 1, 2, 3, and 4, respectively. The differences among the various runs seem to have had no appreciable effect on the electric field pattern. By 1300, the near-Earth shielding is apparent.

3) Comparison of Theoretical Birkeland Currents with Previous Results

Figures 35 to 37 show comparisons of theoretically computed transverse magnetic field variations with those observed by the satellite S3-2 in the auroral zone during the substorm of September 19, 1976. Birkeland current densities computed from the model are shown in Figures 36 and 37, averaged over latitude bins ~0.4°

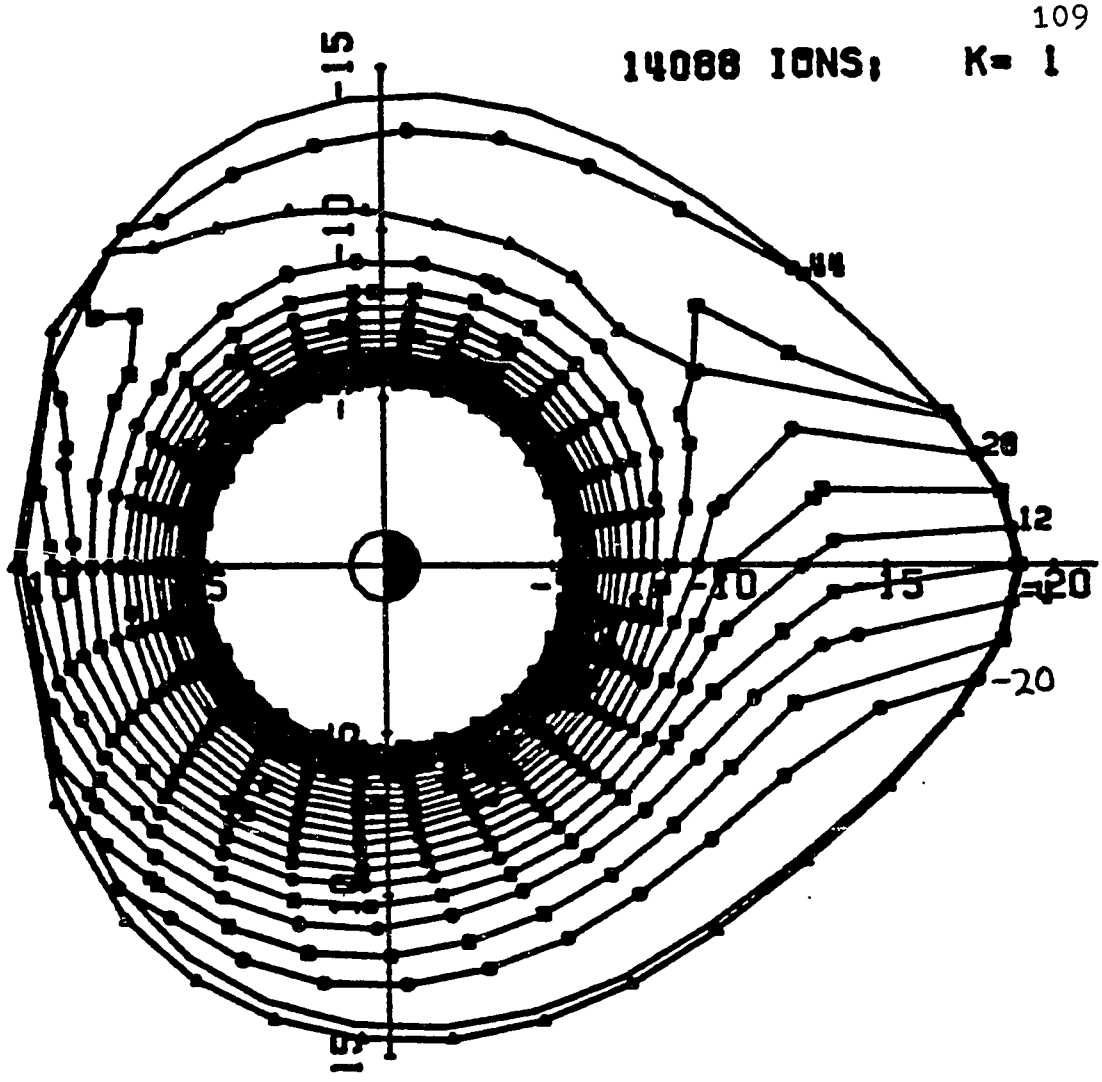

Figure 34(a). Effective potential contours (with corotation) in the equatorial plane at 13:00 UT for high energy ions for run 1. Equipotentials are 8 kV apart.

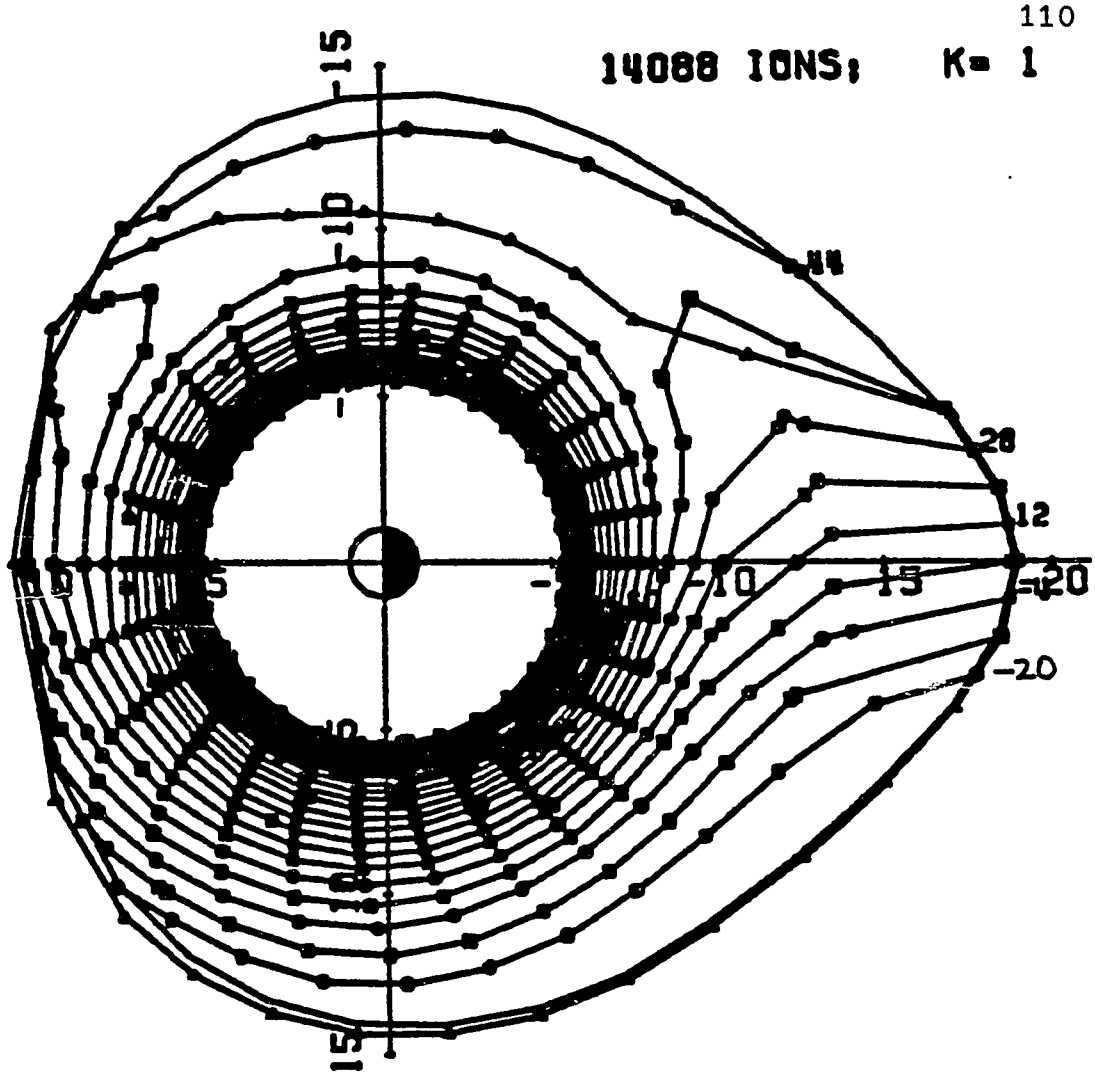

Figure 34(b). Effective potential contours (with corotation) in the equatorial plane at 13:00 UT for high energy ions for run 2. Equipotentials are 8 kV apart.

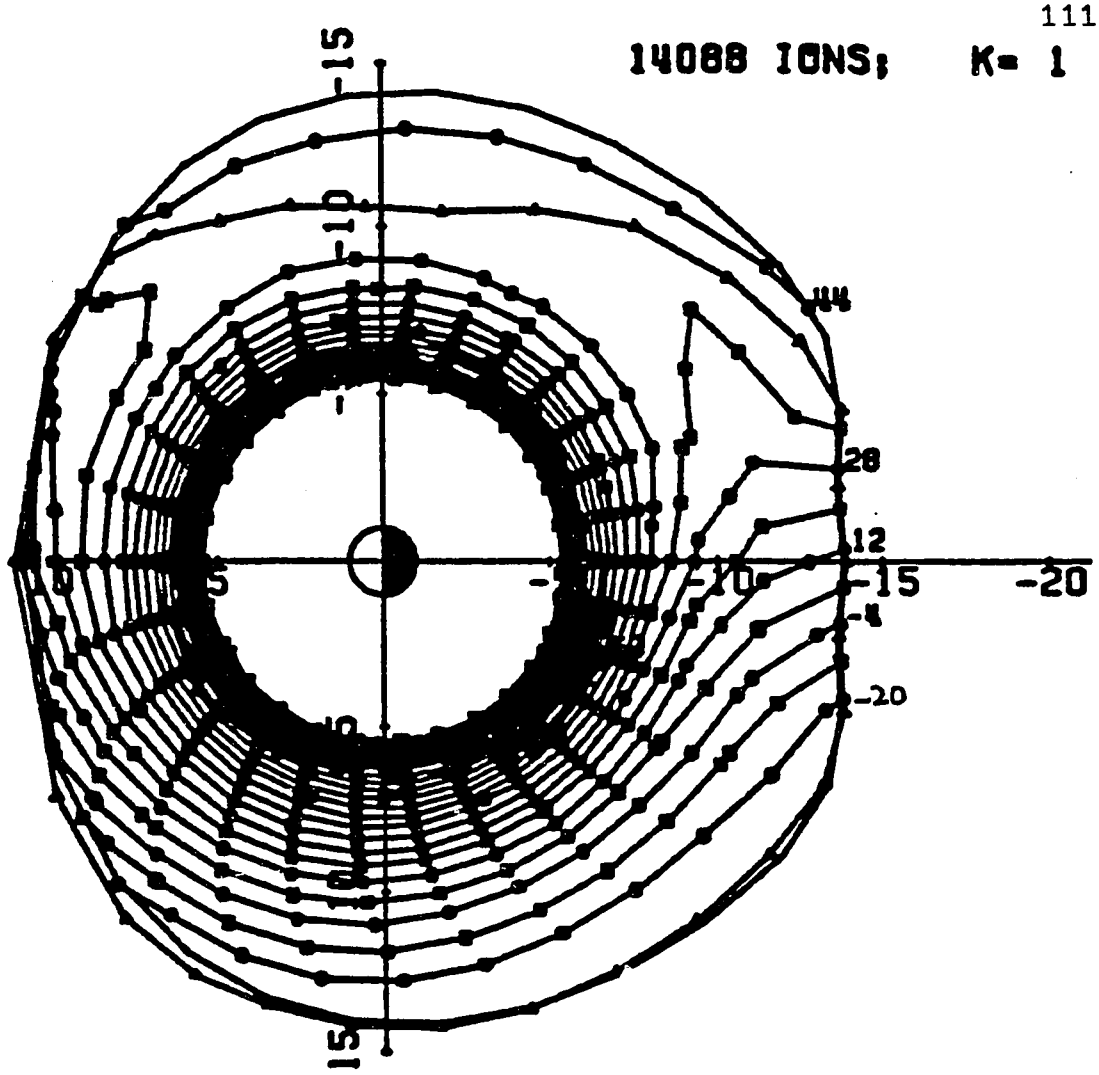

Figure 34(c). Effective potential contours (with corotation) in the equatorial plane at 13:00 UT for high energy ions for run 3. Equipotentials are 8 kV apart.

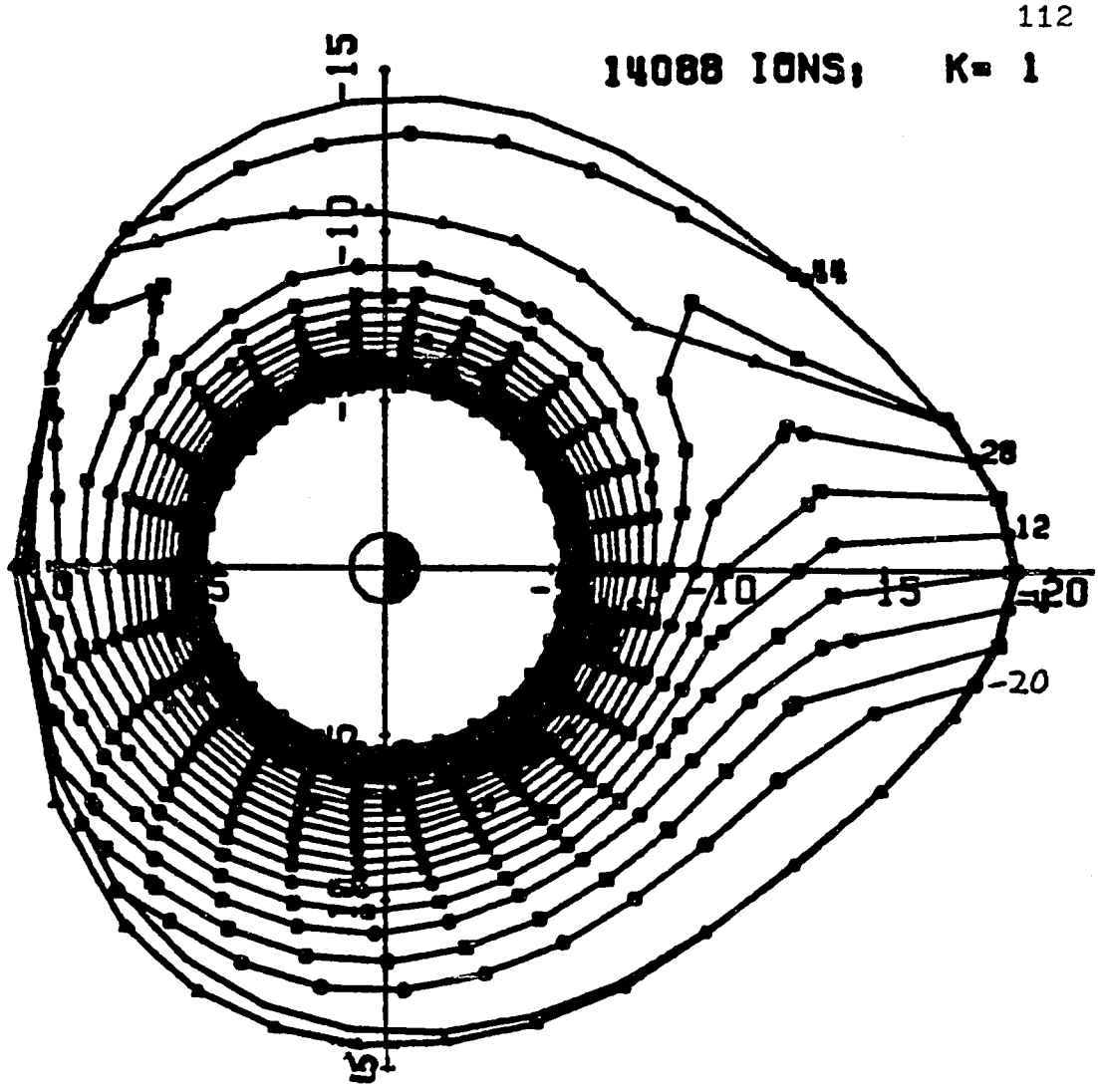

Figure 34(d). Effective potential contours (with corotation) in the equatorial plane at 13:00 UT for high energy ions for run 4. Equipotentials are 8 kV apart.

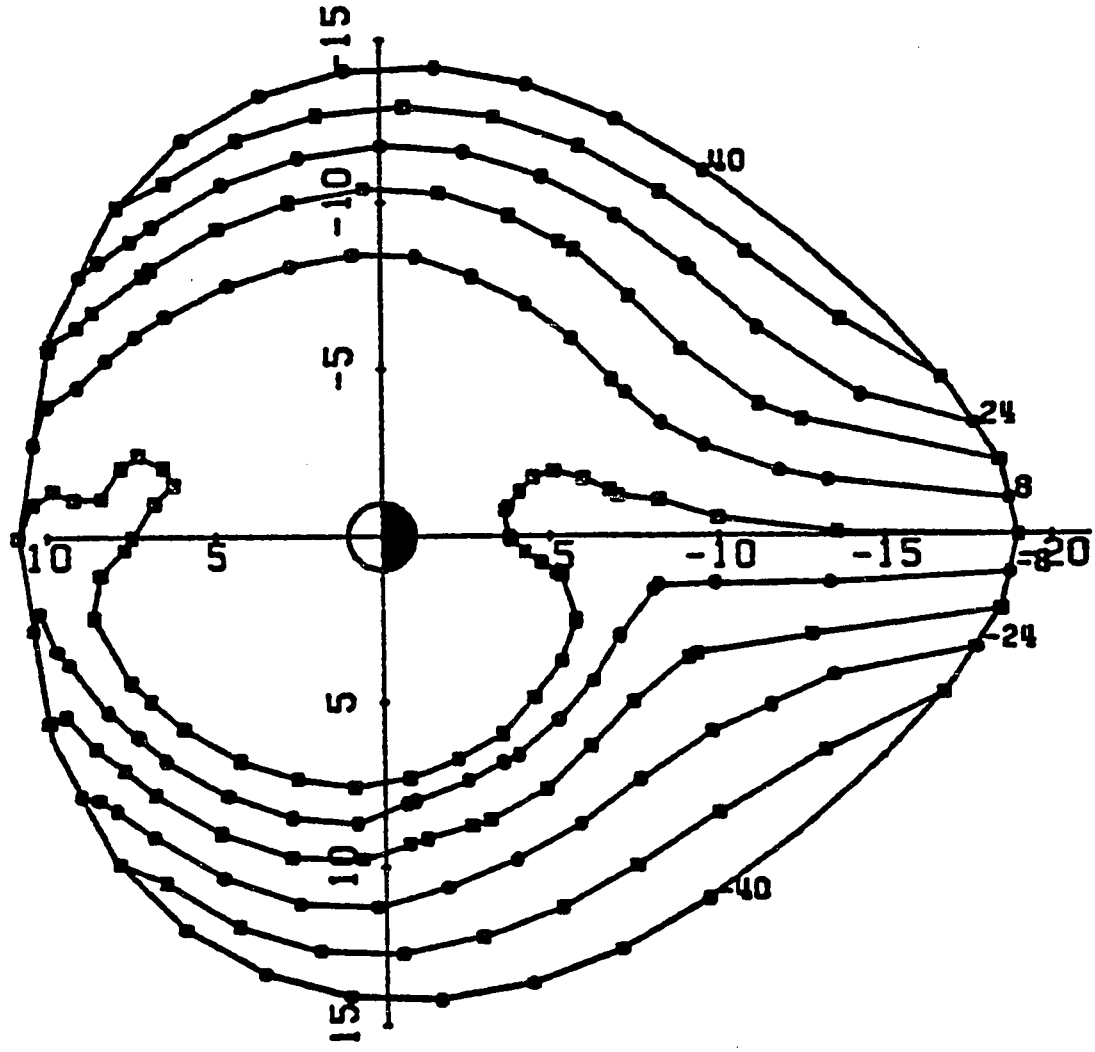

Figure 34(e). Potential contours (without corotation) in the equatorial plane at 13:00 UT for run 1. Equipotentials are 8 kV apart.

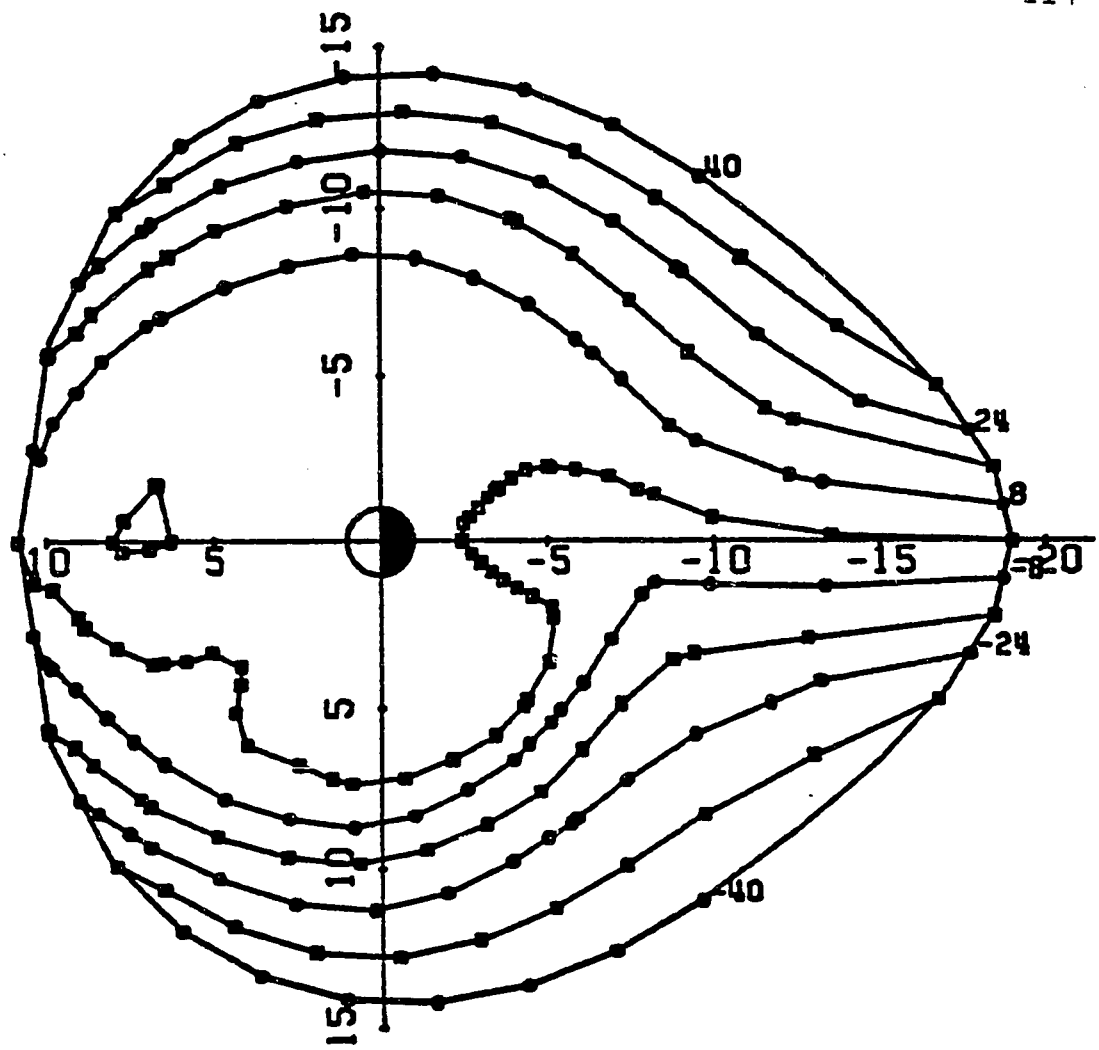

Figure 34(f). Potential contours (without corotation) in the equatorial plane at 13:00 UT for run 2. Equipotentials are 8 kV apart.

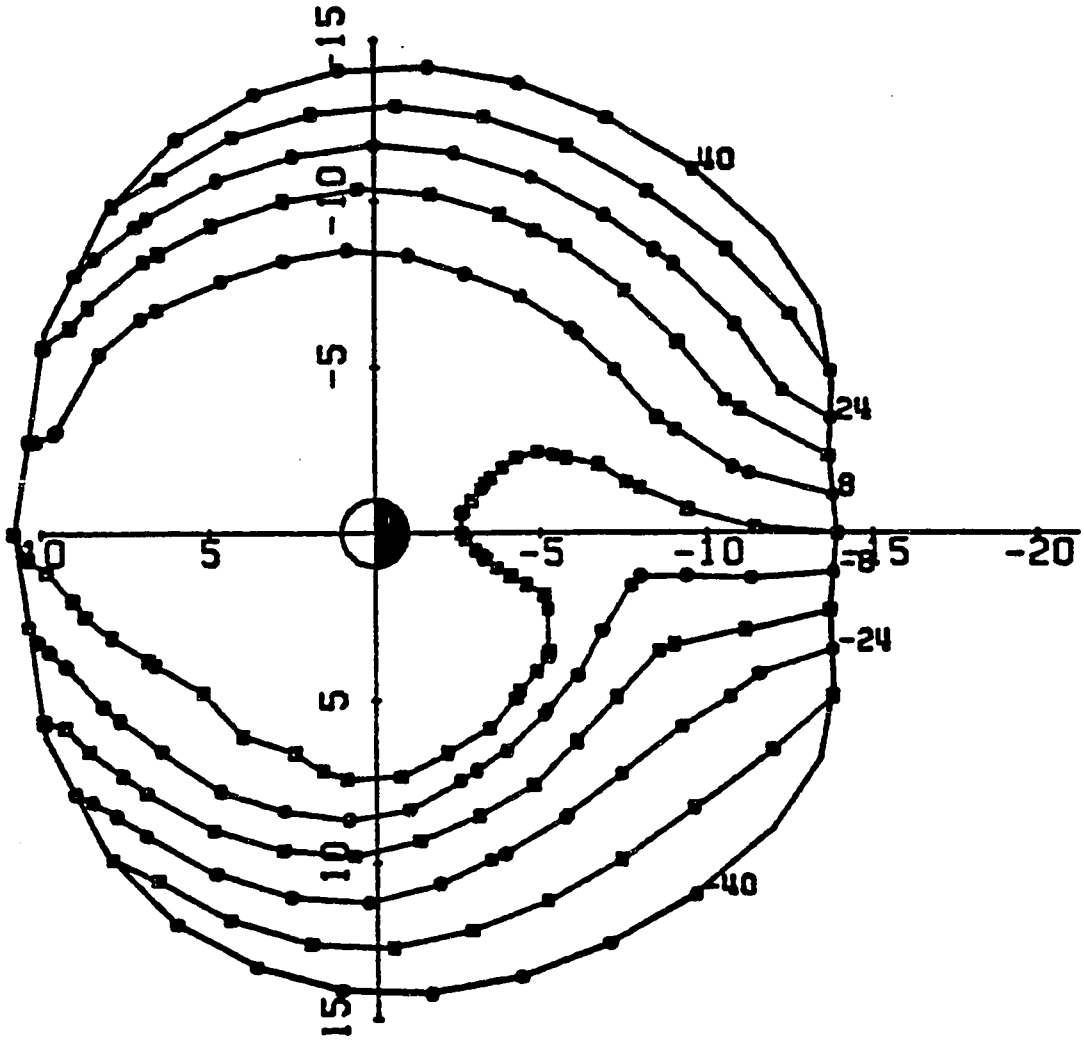

Figure 34(g). Potential contours (without corotation) in the equatorial plane at 13:00 UT for run 3. Equipotentials are 8 kV apart.

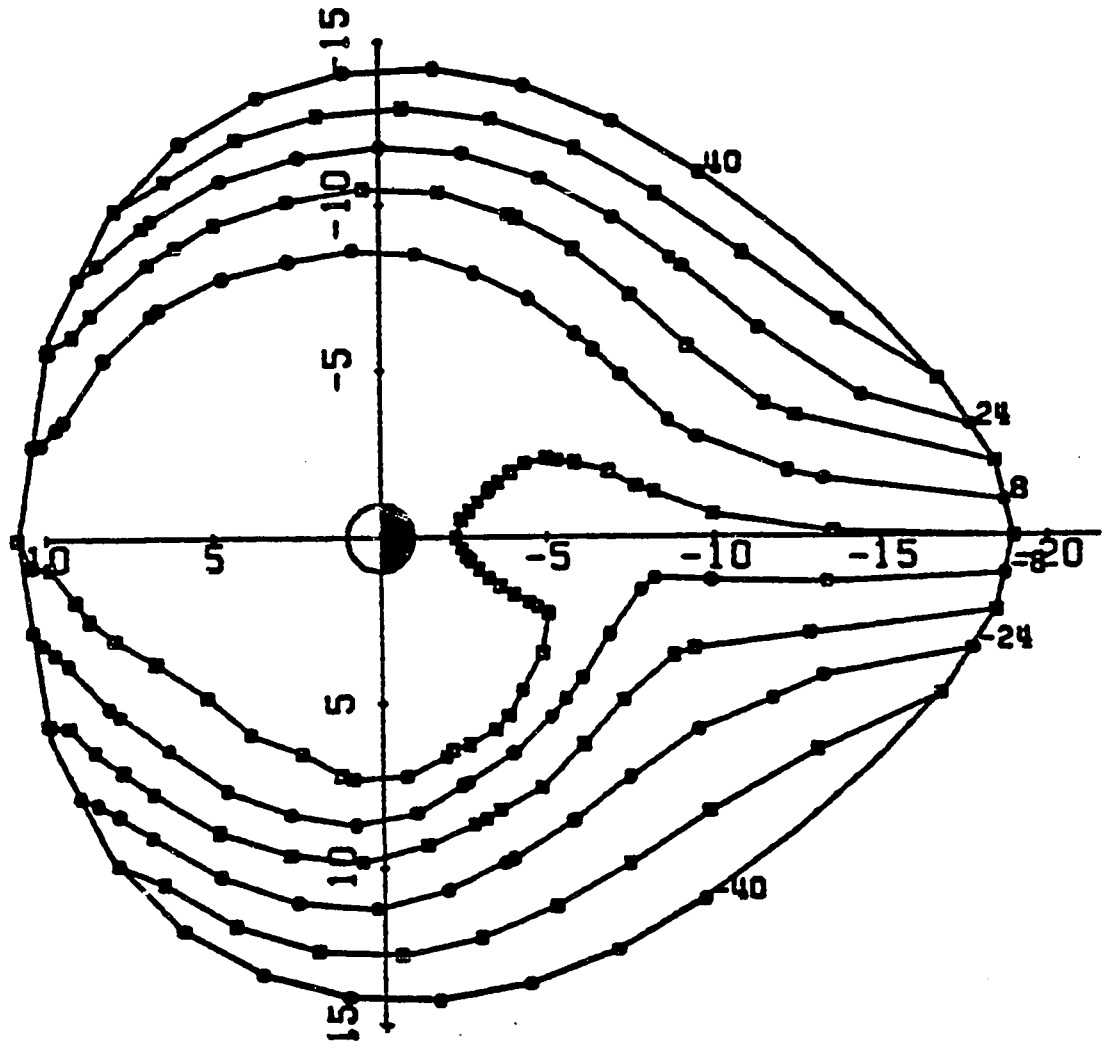

Figure 34(h). Potential contours (without corotation) in the equatorial plane at 13:00 for run 4. Equipotentials are 8 kV apart.

Figure 35. Data from various auroral crossings of the S3-2 satellite for magnetic field variations. The scales at the bottom show degrees invariant latitude from the boundary; satellite invariant latitude and magnetic local time; Greenwich Mean Time in hours, minutes, seconds and also in seconds.

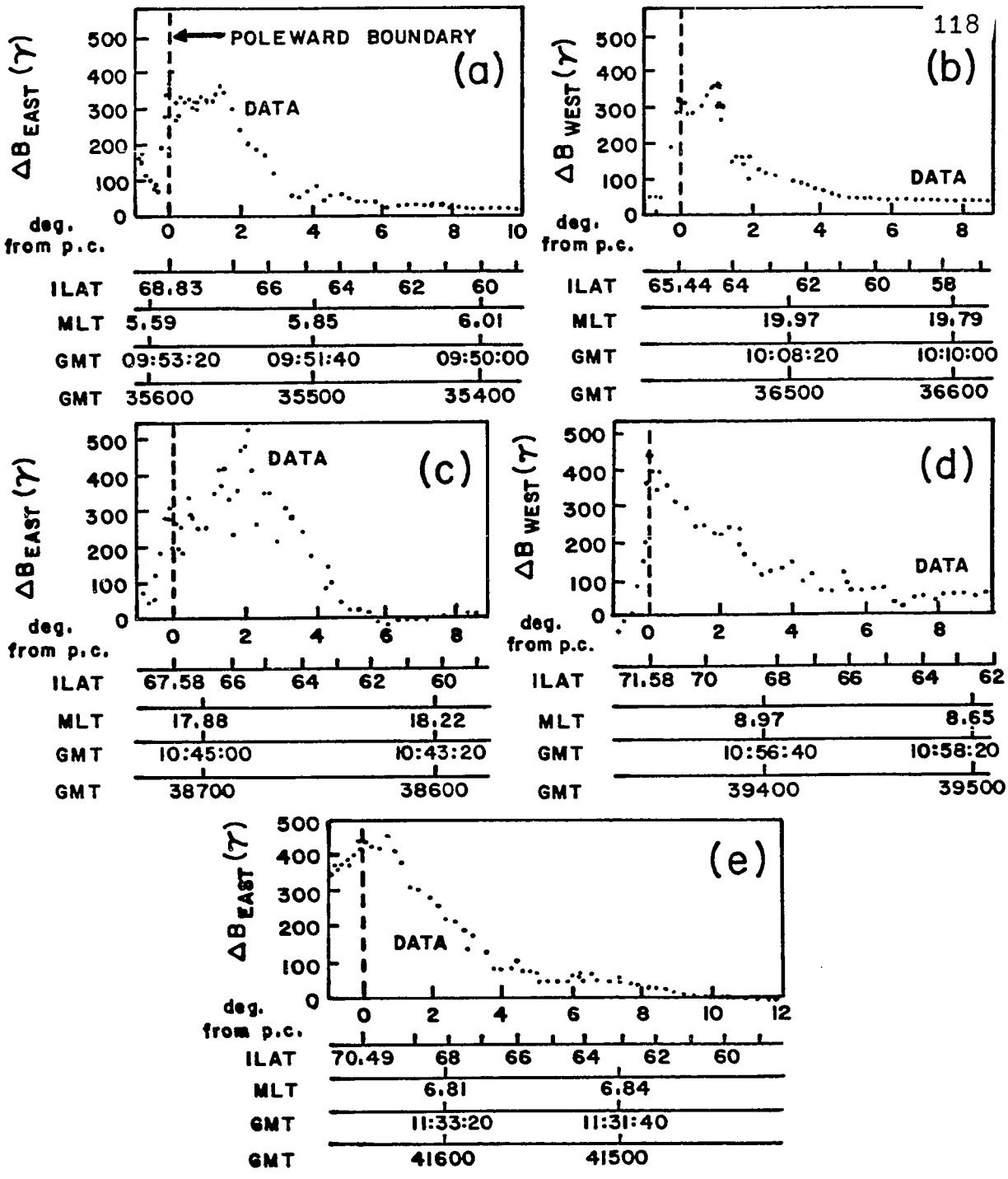

Figure 35(a). Dawnside auroral crossing of S3-2 satellite orbit 4079A (Southern hemisphere). UT ~ 10-E. (b). Duskside auroral crossing of orbit 4079A (Southern hemisphere). UT ~ 1010. (c). Duskside auroral crossing orbit 4079A (Northern hemisphere). UT ~ 1040. (d). Dawnside auroral crossing of orbit 4079A (Northern hemisphere). UT ~ 1100. (e). Dawnside auroral crossing of orbit 4079B (Southern hemisphere) UT ~ 1130.

Figure 36. Comparison of present and previous models for the same passes shown in Figure 35. Magnetic field variations are shown in the top panel. The bottom panel shows computed Birkeland currents for both models. Both theoretical curves are for UT and MLT listed for each individual figure. (a). UT = 10-ε, MLT≈4.8. (b). UT = 1010, MLT≈19.2. (Present model used was run 1.) (c). UT = 1040, MLT≈17.5. (Present model used was run 1). (d). UT = 1100, MLT≈9.2. (Present model used was run 2). (e). UT = 1130, MLT≈6.5. (Present model used was run 2.)

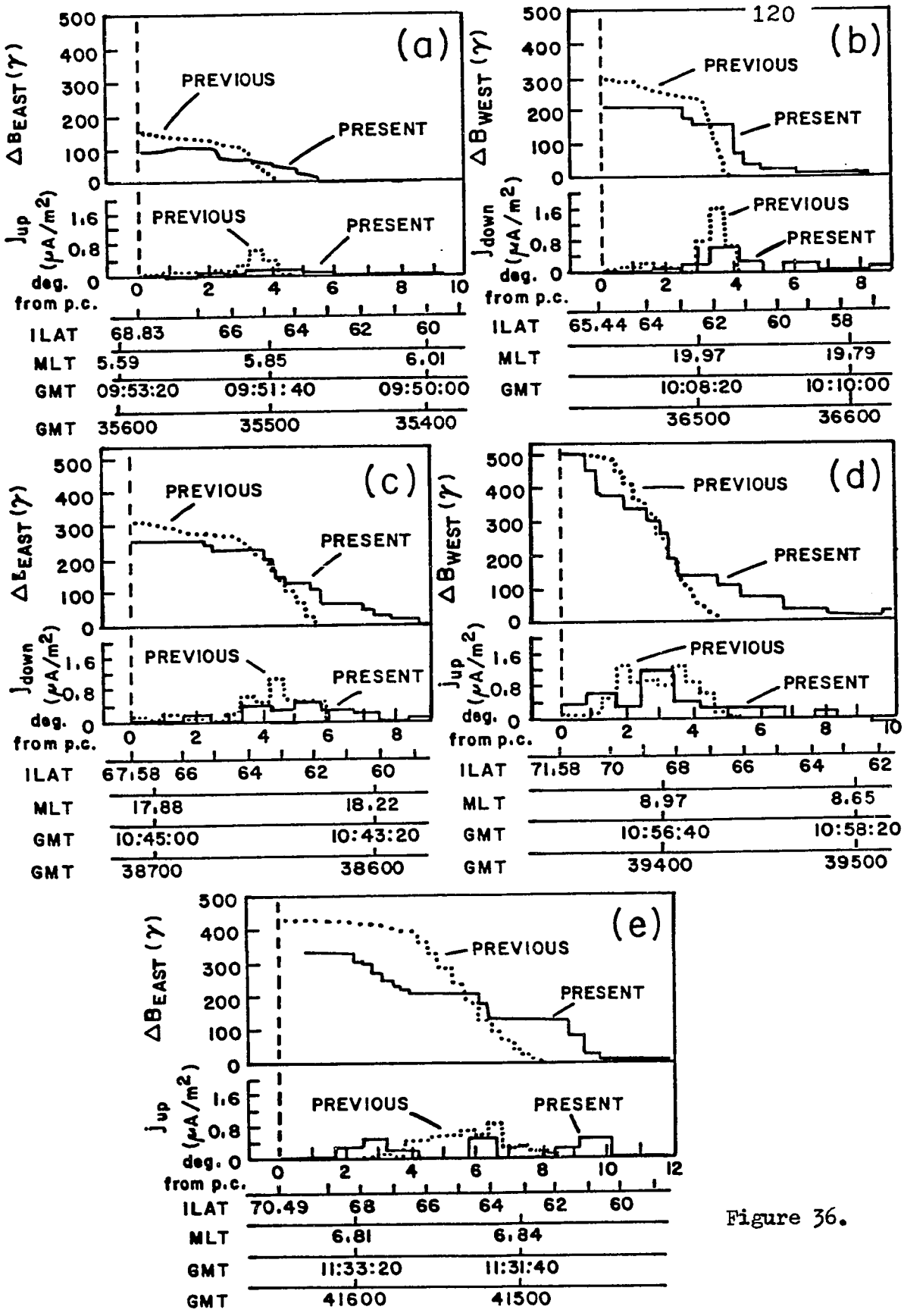
(a)
ΔBEAST (γ)
PREVIOUS
PRESENT
jup (μA/m2)
deg. from p.c.
ILAT 68.83 66 64 62 60
MLT 5.59 5.85 6.01
GMT 09:53:20 09:51:40 09:50:00
GMT 35600 35500 35400
(b)
ΔBWEST (γ)
jdown (μA/m2)
ILAT 65.44 64 62 60 58
MLT 19.97 19.79
GMT 10:08:20 10:10:00
GMT 36500 36600
(c)
ILAT 67.58 66 64 62 60
MLT 17.88 18.22
GMT 10:45:00 10:43:20
GMT 38700 38600
(d)
ILAT 71.58 70 68 66 64 62
MLT 8.97 8.65
GMT 10:56:40 10:58:20
GMT 39400 39500
(e)
ILAT 70.49 68 66 64 62 60
MLT 6.81 6.84
GMT 11:33:20 11:31:40
GMT 41600 41500

Figure 36.

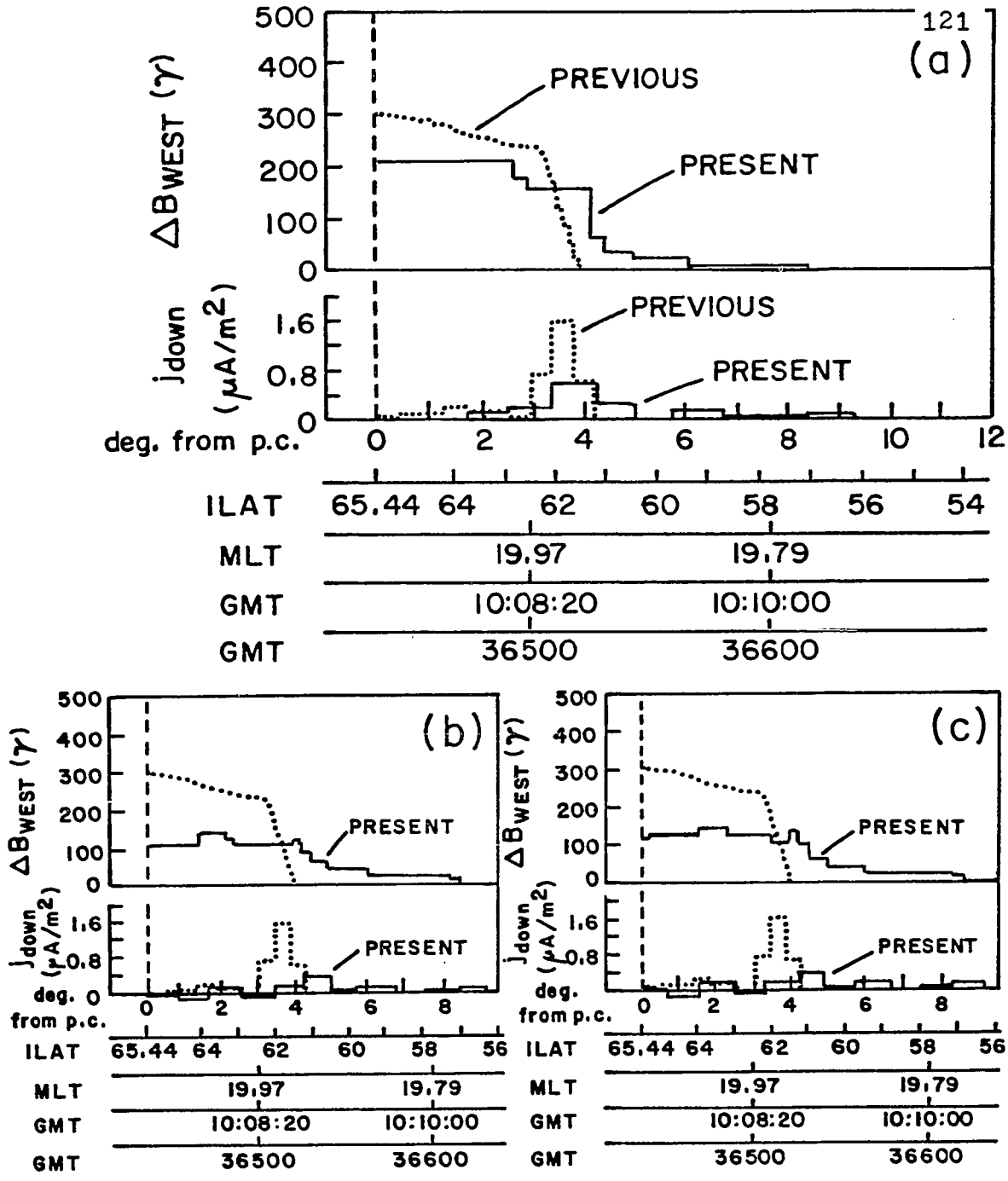

Figure 37. Comparison of runs 1, 2, and 3 for the present model for 1010. Format of the figures is the same as for Figure 36. (a). UT = 1010, MLT ≈ 19.2, run 1 (same as Figure 36(b)). (b). UT = 1010, MLT ≈ 19.2, run 2. (c). UT = 1010, MLT ≈ 19.2, run 3.

wide. Each display in Figures 36 and 37 also shows results from the previous Rice computer simulation of this event (Harel et al., 1981a,b). Only the "nominal" run from the previous results (referred to as "run 1" in Harel et al., 1981a,b) is considered here.

Several comments are necessary at this point:

1) The equation for finding magnetic field variations is given by

$$\Delta B_{\phi}(\Lambda) = \pm \mu_0 R_E \int_{\Lambda_0}^{\Lambda} j_{up}(\Lambda') \, d\Lambda' \qquad \text{(III.D.3-1)}$$

(Harel et al., 1981b) with ΔB_{ϕ} equal to the eastward magnetic variation, j_{up} equal to Birkeland current density, Λ equal to invariant latitude, and Λ_0 equal to the limit (in invariant latitude) of the calculation.

2) There was an approximate 1-6° difference between model boundary invariant latitude and the observed equatorward edge of region-1 currents for previous modeling of this event (Harel et al., 1981b). In the previous model, no region-1 currents were generated. Before, these two latitudes were taken to coincide by plotting "degrees from poleward boundary of calculation," where the observed boundary was used. In this present model, the theoretically computed values have been plotted in the same manner, although now there is some ambiguity as to how to mesh the highest latitude boundaries since the amount of region-1 Birkeland current included in the model varies with time throughout the event.

3) The conductivity model was an algorithm based on satellite S3-2 data, but it is known to be too large by as much as a factor of two in various locations (Harel et al., 1981b).

4) Based on comments 2) and 3) it is not expected that there should be detailed agreement between observations and model calculations. In Figures 35 to 37, the most important aspect to note is the comparison between previous and present model calculations.

Figures 35a,b,c,d,e show the observed magnetic field variations for various times throughout the substorm. Figures 36a,b,c, d,e show ΔB's and Birkeland currents for the same universal times through the event as shown in Figures 35a,b,c,d,e, for previous and present models. Note that the general shape of ΔB has improved. In the previous models, ΔB had a tendency to have a greater slope than data would indicate. The previous models are all flat-topped with an almost vertical, very quick drop-off. Thus, the latitudinal extent of Birkeland current previously predicted had a tendency to be too small.

There is a big improvement in the present theoretical curves since region-2 Birkeland currents are now more evenly spread out in latitude. This is probably mostly due to the fact that the energy of the highest energy ion channel has been almost doubled (λ = 8650 to 14088). The innermost inner edges of the more energetic ions have greater (westward) gradient and curvature drift, and thus connect to relatively large region-2 Birkeland currents further out in the tail. Thus, the region-2 currents are more evently spread out in latitude. This is a major improvement in

the model. Note that in these figures, the lowest latitude region-2 Birkeland current is also now better modeled. It connects mostly to closed rings of high and low energy ions. In the previous models, there was only one K species for each ion energy. There was no representation of trapped radiation (pre-existing quiet time ring current). The present model includes a pre-existing trapped ring current, and this substantially affects and improves the Birkeland current distribution. Figures 36c,d,e show, respectively, computed ΔB's and Birkeland currents for: 1040 UT, ten minutes before the peak of the substorm; 1100 UT, ten minutes after the peak of the substorm; and 1130 UT, at a time of very early recovery. The absence of appreciable region-1 Birkeland currents (due to the holding back) is because the local times of the passes are in the day sector. The generated Birkeland currents in this model are in the night sector (see section III.D.5).

Figures 37a,b,c show ΔB's and Birkeland currents for 1010 UT (ten minutes after onset) for runs 1, 2, and 3, respectively. They display the differences between three different runs for the present model. In comparing Figures 37a (run 1) and b and c (runs 2 and 3), it can be seen that the significant difference here can be discussed with analogy to the major difference between the present run 1 and previous runs. As more particles are held back (three times more held back in runs 2 and 3 than in run 1), the latitudinal spreading out in Birkeland current increases also. Note that in Figure 37a, there is a flat-top and then a vertical drop off in ΔB in the previous run. In the present run 1, there

is a flat-top, then a vertical drop-off, then another flat-top. In runs 2 and 3, there is no dramatic vertical drop off as in run 1. Recalling that run 1 was the one where there was 17% hold back of the particles and comparing this to runs 2 and 3, where there was 51% hold back of particles, we see that the additional particles that are held back contribute to higher latitude region-1 and region-2 Birkeland current now instead of lower latitude region-2 current. The difference between runs 2 and 3 was the magnetic field as previously discussed (see section III.B). General results concerning Birkeland currents are insensitive to whether the nominal or hybrid magnetic field model is used.

The next section discusses the global pattern of Birkeland currents. After this, there is a discussion of region-1 currents in the modeling region for other local times than those discussed here (see section III.D.5).

4) Birkeland Currents — Global Pattern

The next set of figures (Figures 38 to 41) are global plots of Birkeland currents. Figure 38 presents observational summaries by Iijima and Potemra (1978) both for weakly disturbed conditions and for active periods. These are to be compared with Figures 39 to 41 which are global plots of theoretical Birkeland currents throughout the event. These figures are views of the ionospheric auroral zone area. In these figures, a 2° offset from midnight of the model coordinate system can be seen (Harel et al., 1981a). The outermost circle is at 60°, and the inner cross is at the geo-

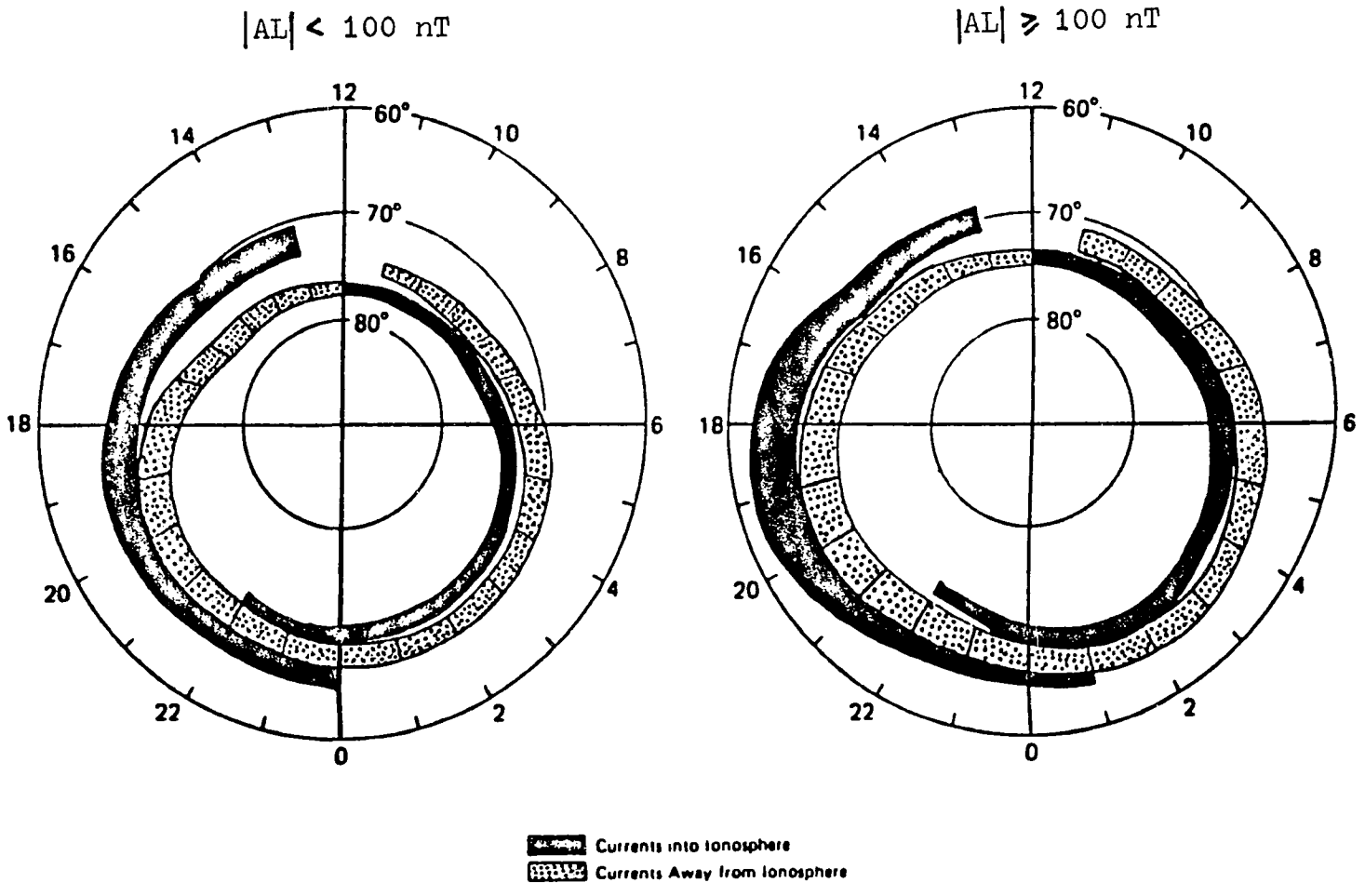

Figure 38. A summary of the distribution and flow directions of large scale field-aligned currents of magnitude greater than .25 $\mu A/m^2$. From Iijima and Potemra (1978).

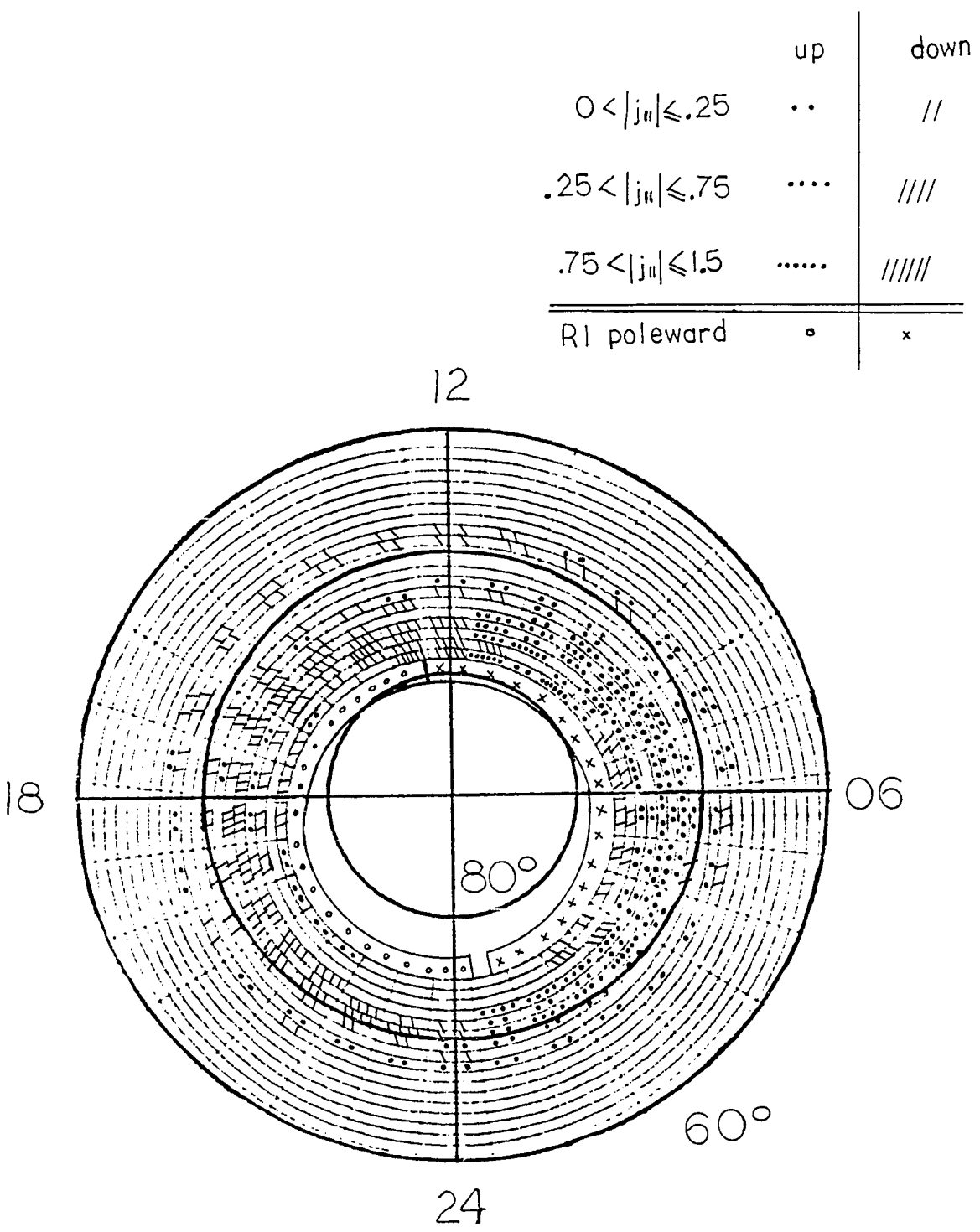

Figure 39. Global pattern of Birkeland currents, UT = 10 - ϵ, run 2. Units for legend at the top are $\mu A/m^2$. "R1 poleward" currents of strengths greater than .1 $\mu A/m^2$ are shown.

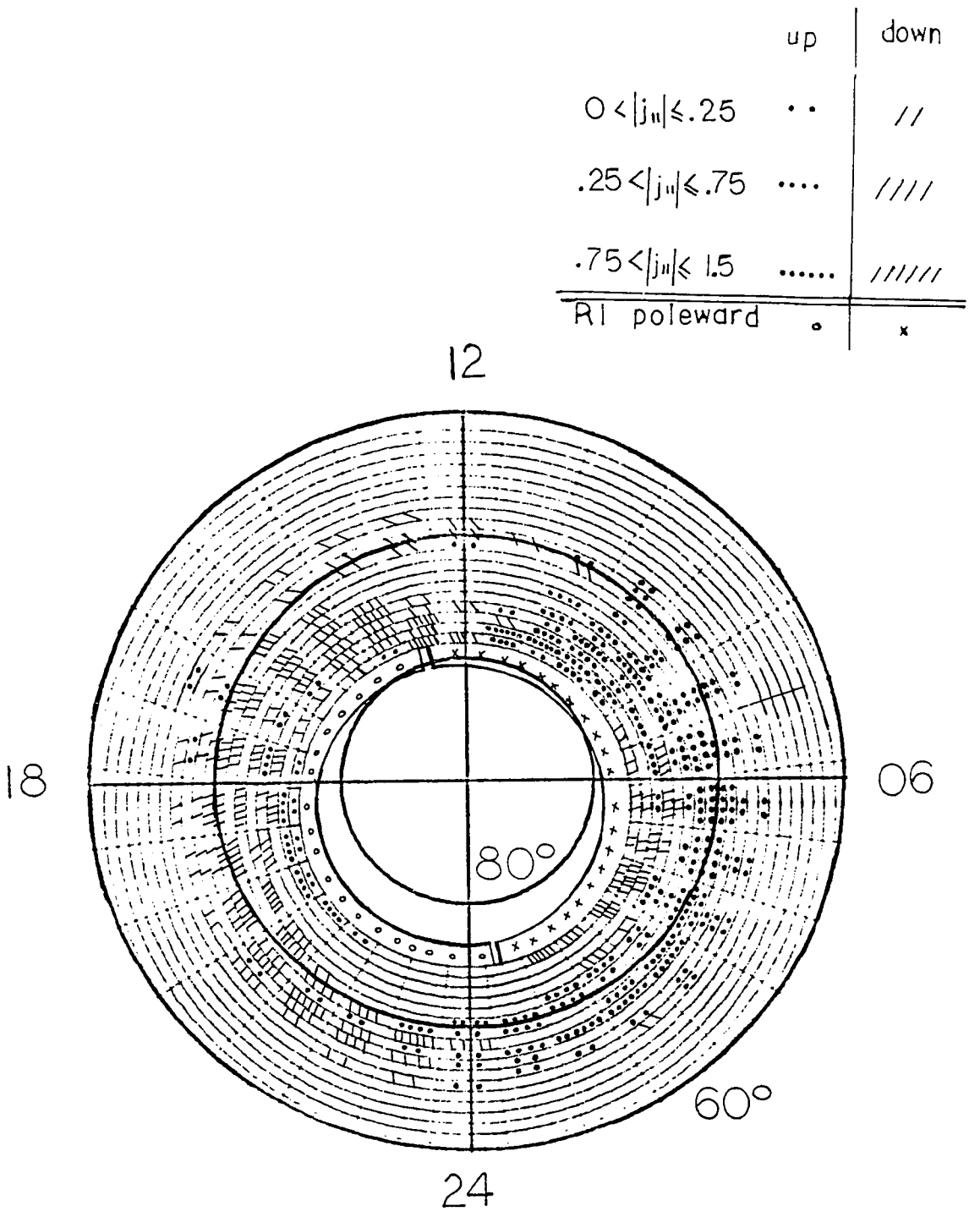

Figure 40. Global pattern of Birkeland currents, UT = 1040, run 2. Units for legend at the top are $\mu A/m^2$. "R1 poleward" currents of strengths greater than $.1\,\mu A/m^2$ are shown.

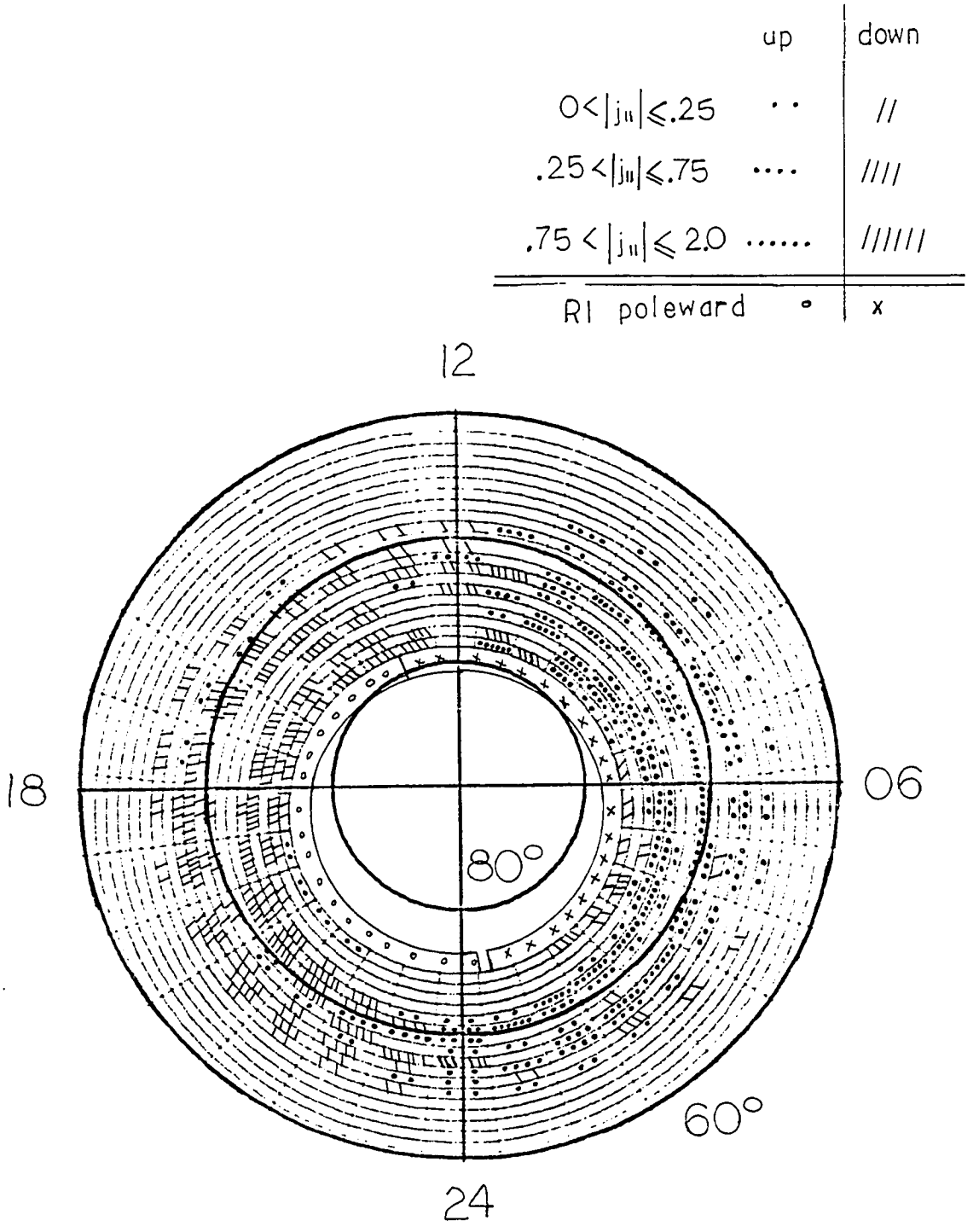

Figure 41. Global pattern of Birkeland currents, UT = 1130, run 2. Units for legend at the top are $\mu A/m^2$. "R1 poleward" currents of strengths greater than .1 $\mu A/m^2$ are shown.

magnetic north or south pole.

It must be remembered that this model can generate some of the region-1 Birkeland currents, specifically those region-1 currents connecting to sunward convecting, closed flux tubes in the modeled region. There are still some higher latitude region-1 Birkeland currents, which are represented by a latitudinal thickness of ~3.3° in latitude poleward of the high latitude boundary of the model in these figures. The region-1 Birkeland currents just poleward of the boundary of the calculation are estimated by the assumption that horizontal currents flowing into or out of the poleward boundary are completed only by Birkeland currents (Harel et al., 1981b). In Karty (1981), a more elaborate calculation was considered for region-1 currents poleward of the high latitude boundary for the previous model of this event. The simple assumption that horizontal currents which flow into or out of the poleward boundary are completed only by region-1 Birkeland currents provides a reasonable first approximation to the model of Karty (1981).

Figure 39 presents the global Birkeland current pattern for 10 - ε UT, which is at a time just before onset. (This is an hour after the cross-tail potential drop starts to increase for the modeled event.) There is little generation of region-1 Birkeland current in the modeled region. The majority of the region-1 current shown is from the additional band, attached to an area just poleward of the high latitude model boundary. Note the similarity between Figure 39 and the observed quiet time pattern in

Figure 38.

Figure 40 shows the global pattern for run 2 at 1040 UT, which is ten minutes before the peak of the substorm. By this time, there is a relatively large amount of generated region-1 current in the modeled region. This is the current directed upward (out of the ionosphere) from ~18:00 MLT to about an hour before midnight and directed downward (into the ionosphere) in the dawn-midnight sector. Note the similarity between Figure 40 and the observed pattern (in Figure 38) during active periods. There is an interesting asymmetry in the pattern in Figure 40. On the dusk side, there is a long "tongue" with relatively small current density and on the dawn side, there is a patch of relatively strong region-1 current at about 3:00 MLT, with small current densities at ~6 MLT. To understand this, the shape and location of the inner edges must be noted. The majority of the region-1 Birkeland currents in the modeling region connect to held back species. The high energy ions have large westward gradient and curvature drift, so that each inner edge that is held back has a dawn-dusk asymmetry such that the inner edge comes much closer to the Earth on the dawn side. (See this behavior in Figure 29a for the K = 1 species.) That is, there is more of a "kink" in the inner edge on the dawn side (in the dawn-midnight quadrant) rather than the dusk side. Thus, for times in the first hour after onset, there are large Birkeland currents connecting to the "kink" with the sense of region-1 Birkeland current (directed into the ionosphere on the dawn side). On the dusk side, for the high and

low energy ions, there are no dramatic bends in the inner edges, (except at ~1000 + ε when for runs 2 to 4, additional hold back starts), so that the connecting region-1 sense Birkeland current (directed upward from the ionosphere on the dusk side) is relatively weak, but spread out in local time. The region-1 Birkeland current on the dusk side extends further than the "held-back-particles" region, which ends at MLT ≈ 20:00 for run 2. The held back species, even in the region which is not held back, contributes to an area of region-1 current which is ~2 hours long in MLT. (The region-1 Birkeland currents in the modeled region generally connect to held back species.)

Figure 41 shows the situation for run 2 at 11:30 UT, in a period of very early recovery (~1 1/2 hours after the onset). The pattern is similar to the situation at 10:40 (Figure 40).

The next section discusses Birkeland current strength and the local time dependence of Birkeland current.

5) Magnitude of Region-1 Birkeland Current Generated in RCM Region

Figure 36, which compared Birkeland current computed in the new models with the old model values, showed little region-1 current within our modeling region. In Figures 36a,b, this is because UT = 10 - ε and 1010, respectively, which are both more than thirty minutes from the peak of the substorm. In Figures 36c,d,e, this is because the passes were in the day sector.

Figure 42 shows a plot of Birkeland current versus local time for UT = 10:40 for run 2. Note especially the curve labeled "'R1' in RCM region." The points around midnight (dashed part of curve) are not generated from the new mechanism discussed in this thesis, but probably result from the confusion around midnight as to what is region-1 and what is region-2. (It is not unusual for experimental plots of Birkeland current in the form of Figure 42 to exclude a small local time region around midnight.) The curve labeled "'R1' poleward of RCM boundary" was calculated by the estimate that horizontal currents flowing into or out of the poleward boundary are completed solely by Birkeland currents (see discussion in the previous section). It appears from Figure 42 that on the dusk side, the maximum region-1 current strength generated by "holding back particles" is about 25% of region-2 current, while on the dawn side, the maximum region-1 current strength is about 50% of region-2 current. Although the current strength is greater on the dawn side (as is expected by inner edge location, discussed in the previous section), the currents are more spread out in local time on the dusk side. It is probable that the region-1 current in the RCM region could be increased by using a more realistic conductivity model and smaller grid size.

Conductivity tends to be greatest in regions of upward Birkeland current. This is especially true in the dusk portion of region-1 current connecting to sunward convecting flux tubes, as can be seen, for example, in the observations shown in Figure 9. For these reasons, the hour from 10:00 + ε to 11:00 was rerun

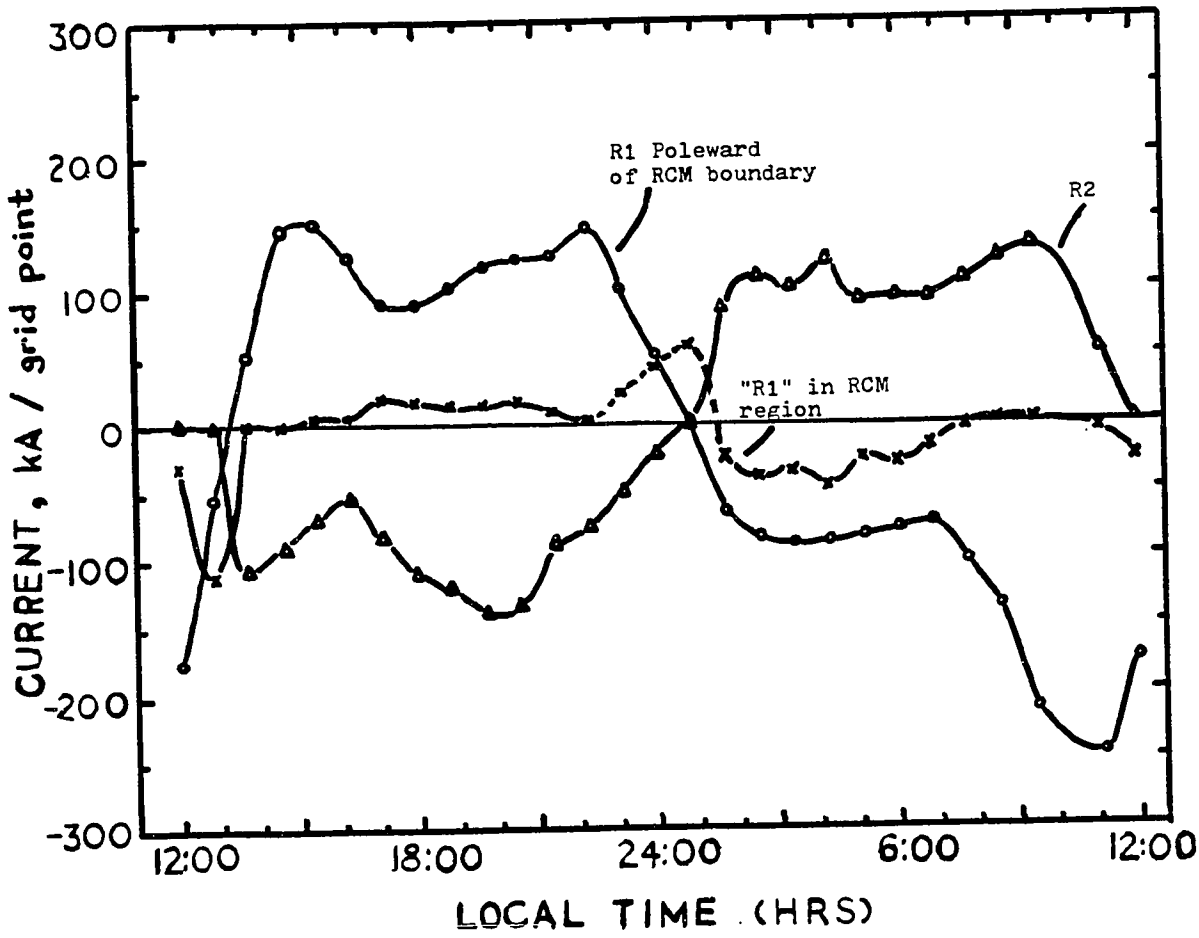

Figure 42. Three "types" of Birkeland current versus local time computed for UT = 10:40 for run 2. R1 is region -1 Birkeland current. R2 is region -2 Birkeland current. RCM is the Rice Convection Model.

using all the inputs as in run 2, but with a more realistic conductivity (discussed below) and a polar boundary potential distribution previously used in Harel et al. (1981a) (see section II.C.4).

Figures 43a and b show the conductivity model used as input for runs 1 to 4, for UT = 10:40. This conductivity model is discussed in section III.A. In order to provide a more realistic conductivity model for the high latitudes associated with region-1 current, the conductivity model previously used in Karty et al. (1982) (e.g., Figure 2c) was used here. From ~70° and equatorward the previous model was used. Poleward conductivities were found by integration of satellite data over a distance defined by electron flux enhancement, and then fitting the data to a trigonometric function of local time. Conductivities in this higher latitude region are dominated by auroral enhancement. Actual measurements are at dawn and dusk. At all other local times, conductivity was obtained by extrapolation. The lower latitude and higher latitude conductivity models were then meshed together to provide a somewhat smoothed model. Figures 44a and b show the modified conductivity model. Note the region-1 dusk conductivity enhancement.

Figure 45a shows the global pattern of Birkeland currents at UT = 10:40 for run 2, but with the modified conductivities of Figure 44, and the previous boundary potential model. This should be compared with Figure 40. Note the increase in extent and strength of region-1 current in regions centered around ~21:00 MLT

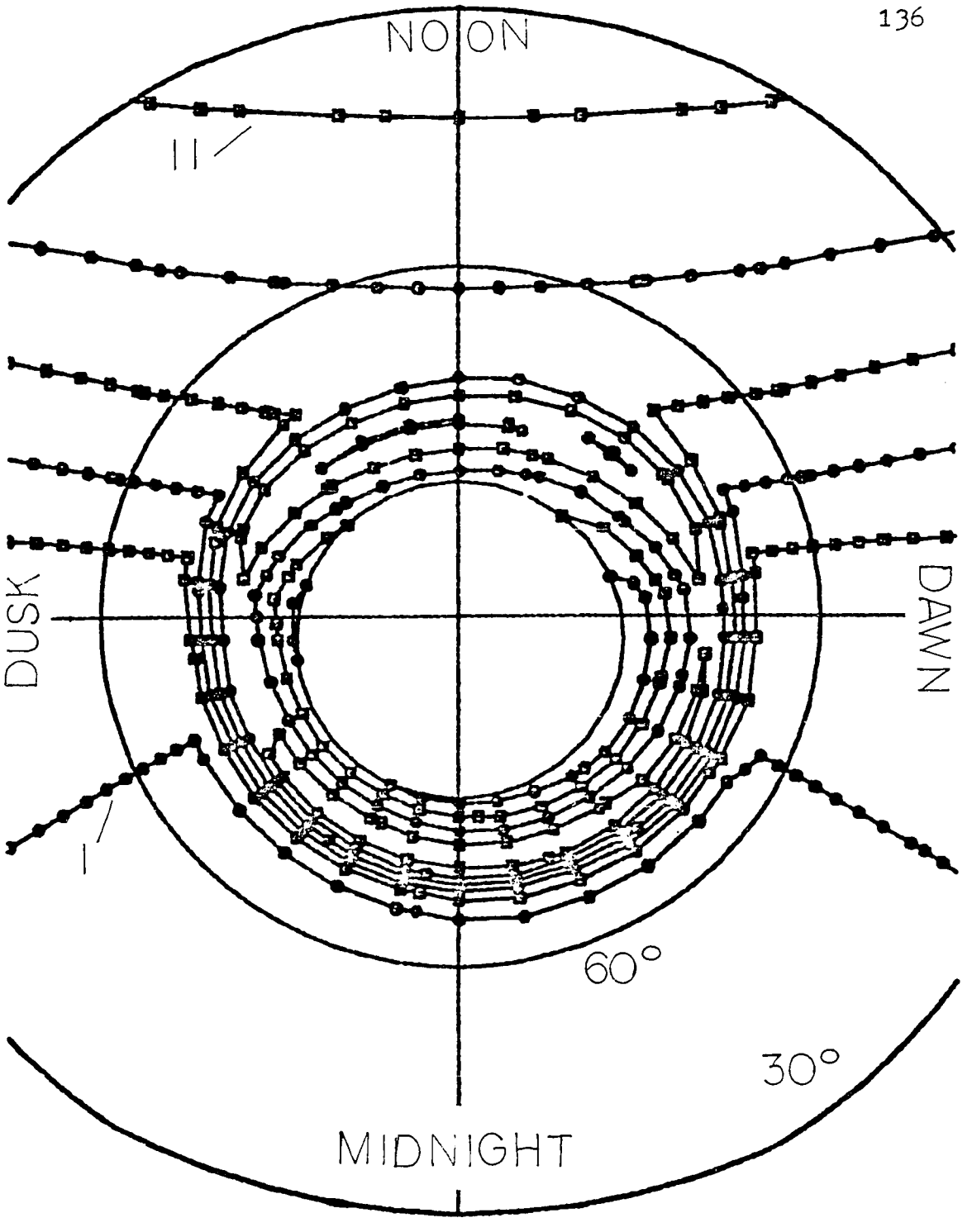

Figure 43a. Pedersen conductivity (in mhos) used as input for runs 1 to 4. The interval between contours is 2 mhos. UT = 10:40.

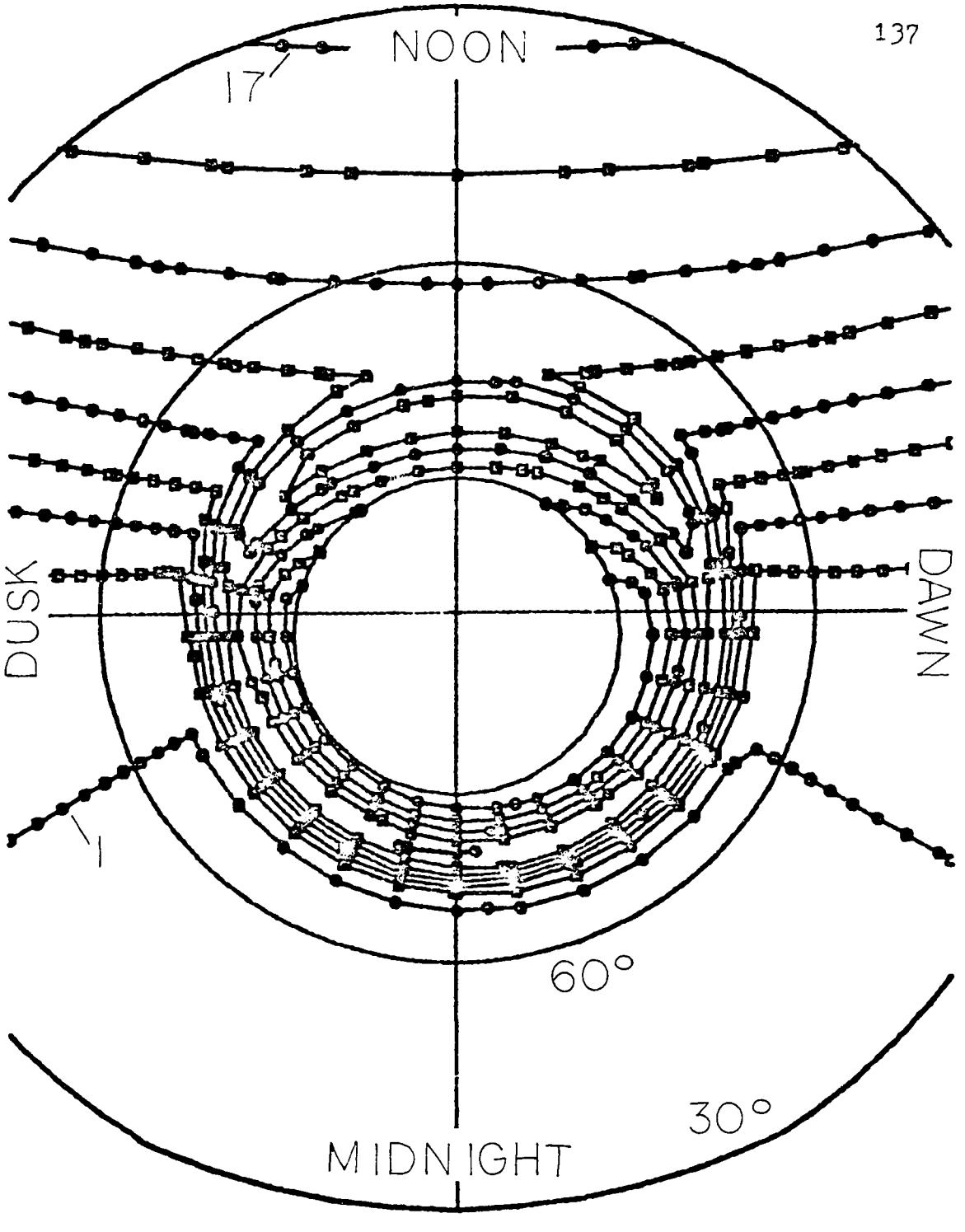

Figure 43b. Hall conductivity (in mhos) used as input for runs 1 to 4. The interval between contours is 2 mhos. UT = 10:40.

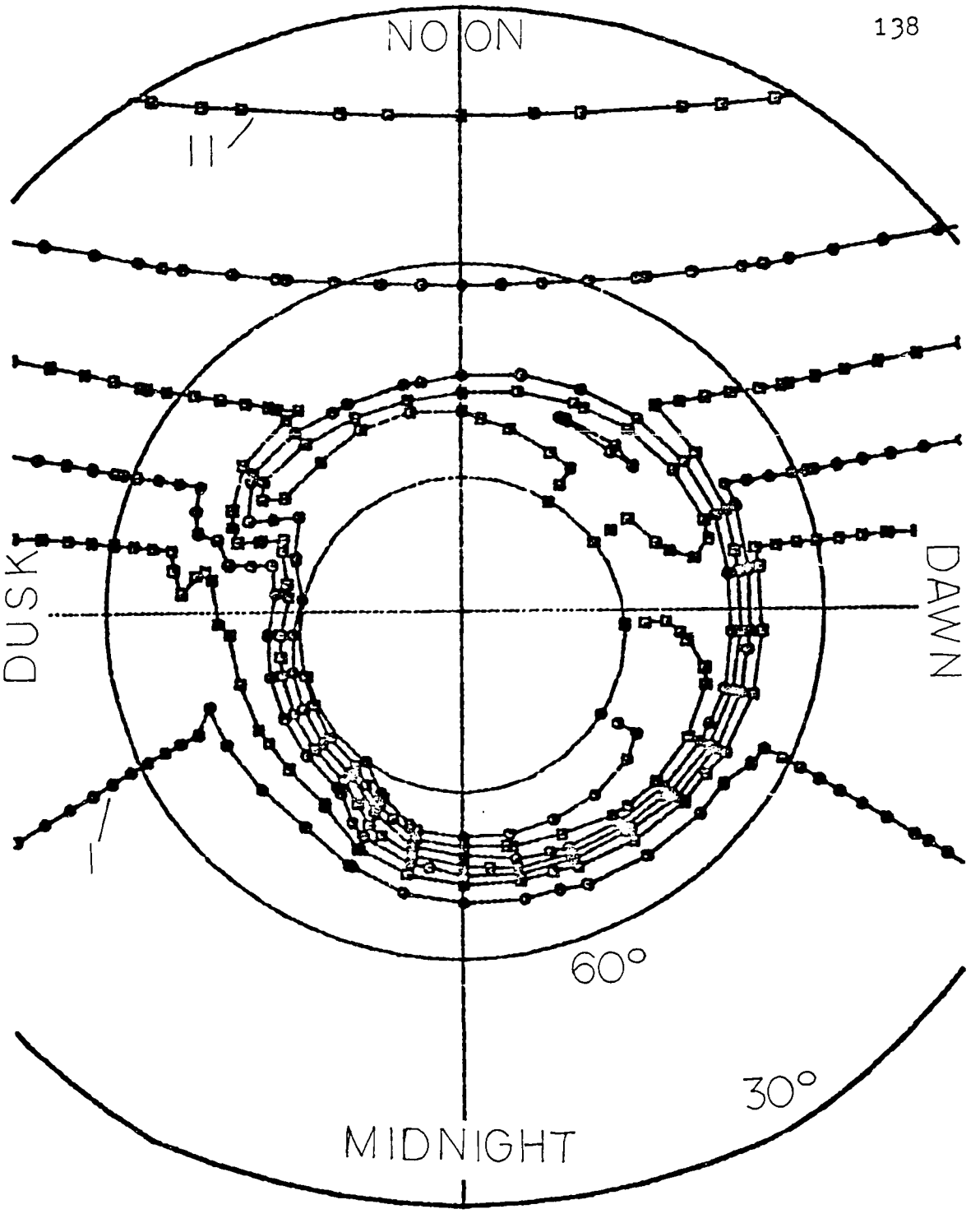

Figure 44a. Modified Pedersen conductivity (in mhos) used as input for 10:00+∈ to 11:00 UT of run 2, but with increased region -1 conductivity. The interval between contours is 2 mhos. UT = 10:40.

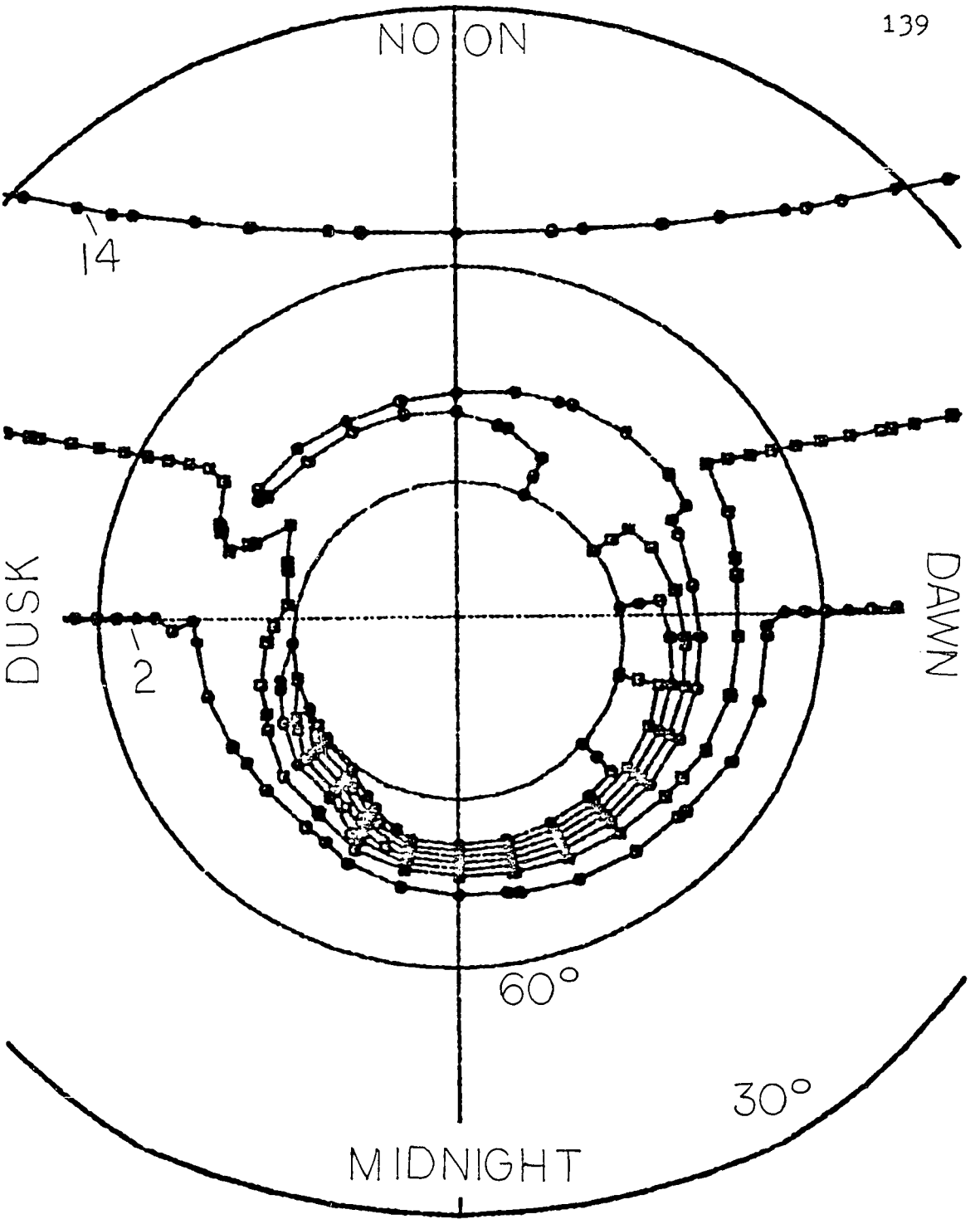

Figure 44b. Modified Hall conductivity (in mhos) used as input for 10:00+∈ to 11:00 UT of run 2, but with increased region -1 conductivity. The interval between contours is 6 mhos. UT = 10:40.

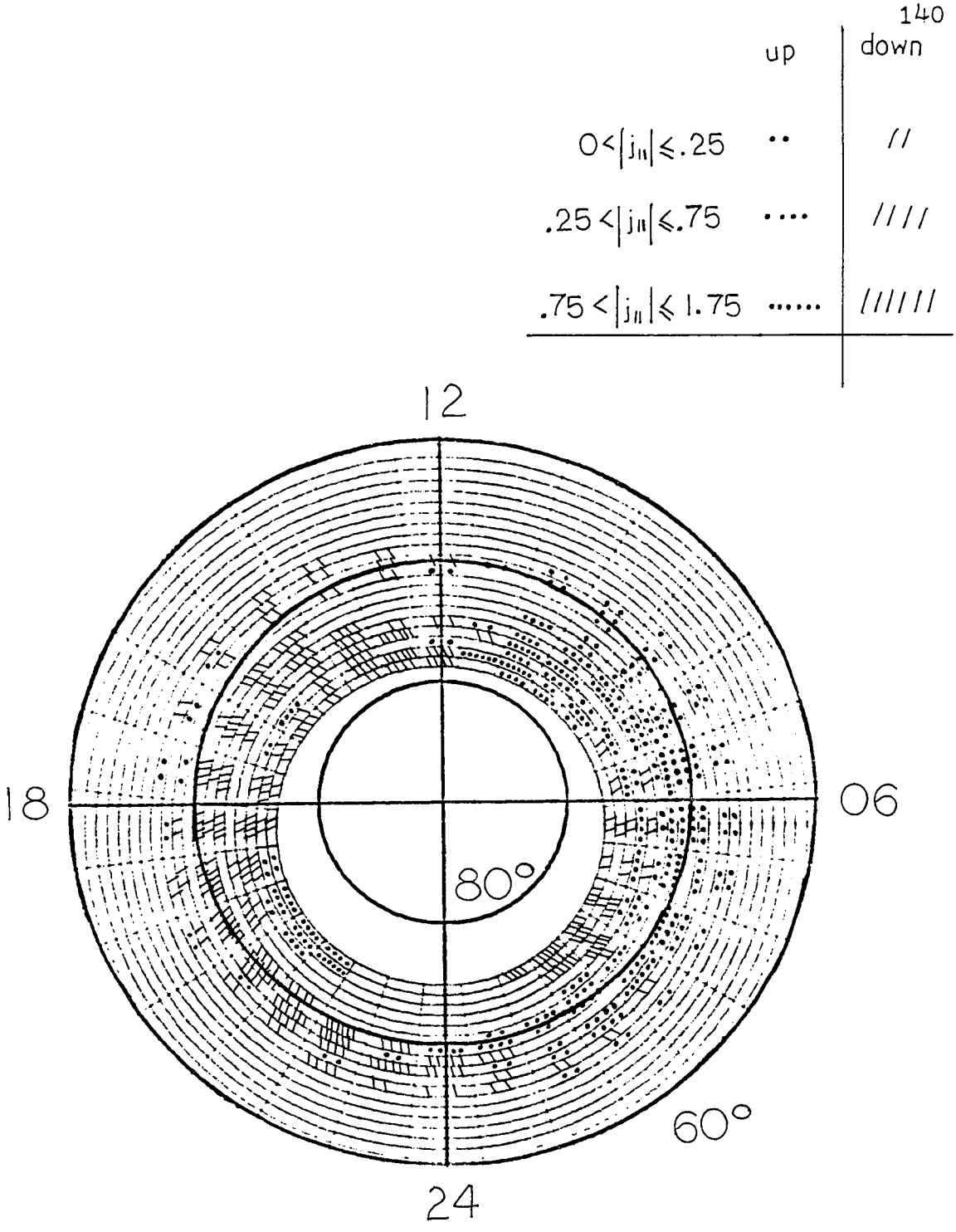

Figure 45a. Global pattern of Birkeland currents, UT = 10:40, for run 2, but with increased region -1 Pedersen and Hall conductivities (as shown in Figure 44) and previous polar boundary potential (Harel et al., 1981a) Current strengths are in units of $\mu A/m^2$.

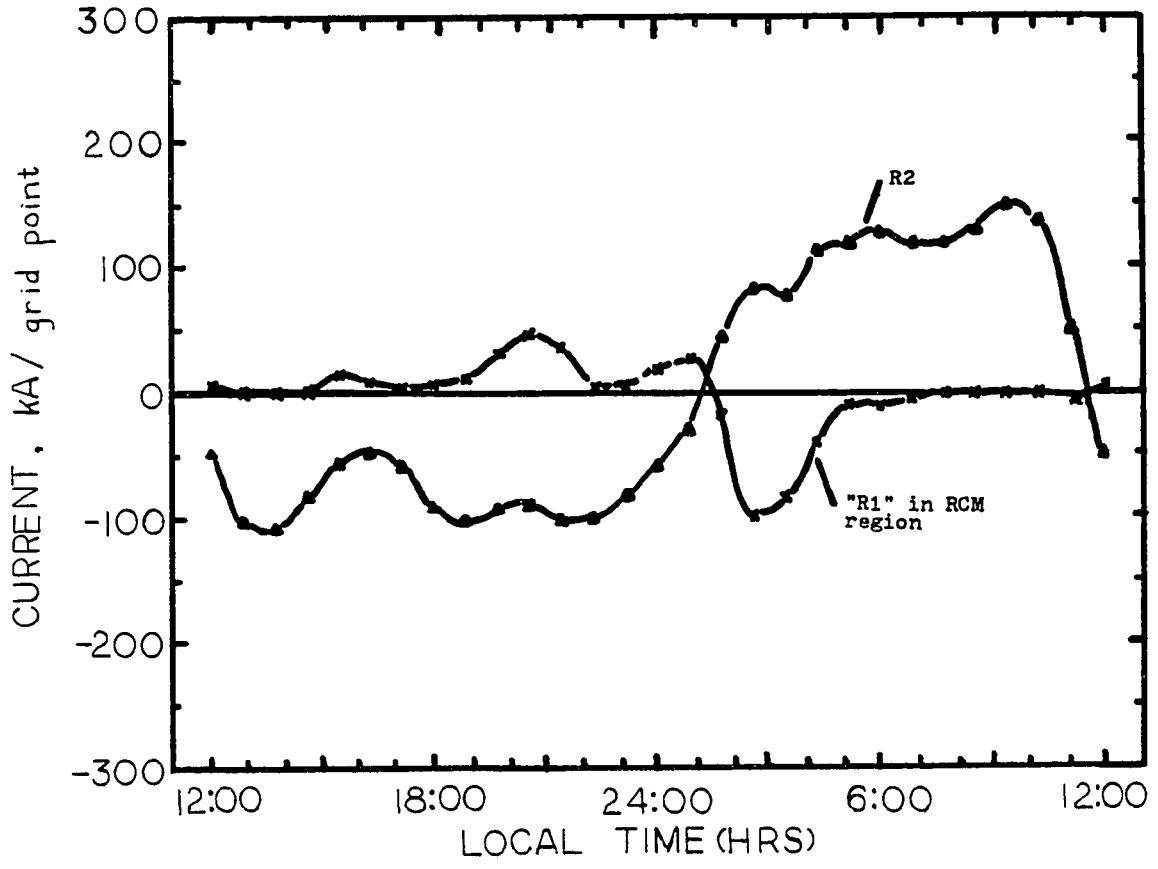

Figure 45b. Region -1 and region -2 Birkeland current versus local time, computed from the RCM for UT = 10:40, for run 2 but with increased region -1 Pedersen and Hall conductivities, as shown in Figure 44, and previous polar boundary potential (Harel et al, 1981a).

and ~3:00 MLT.

Figure 45b shows region-1 Birkeland current versus local time calculated from the RCM for the same conditions as Figure 45a. This should be compared to Figure 42. Note that the region-1 currents computed by the RCM have approximately doubled in both the dawn and dusk regions.

The next section further discusses the dawn-dusk asymmetry in current strengths apparent in Figures 42 and 45b.

6) General Comments

This model has only considered the amount of current generated from R ~ 20 R_E earthward. The RCM cannot reliably be extended past ~20 R_E since the assumptions of steady convection and "slow-flow" do not hold much further out than ~20 R_E. Using equation (II.A.2-5), we can estimate the current which should be generated in the region of ~20 R_E to 50 R_E. Approximate values for flux tube volumes which are needed for this estimate are provided by Erickson and Wolf (1980). We consider the amount of current generated by the held back species of high and low energy ions and electrons in the equatorial plane from ~20 R_E to 50 R_E. Doing this, we get $J_{\parallel i} \approx 356$ kAmps. The maximum amount of region-1 current generated inside the modeling region (see Figure 45b) is ~(100 kA/grid point) × 4 gd pts on the dawn side and ~(50 kA/gd pt) × 5 gd pts on the dusk side. Assuming the same amount of current is outside the modeling region on the dawn and dusk sides, we get that ~47% of the current is outside the modeling region on the

dawn side and ~59% of the current is outside the region of the dusk side.

Figure 11 shows that the observed average region-1 current equatorward of the polar cap boundary on the dawn side is greater than on the dusk side. This figure thus shows less region-1 current strength (connecting to sunward convecting flux tubes) on the dusk side than the dawn side. These S3-3 satellite observations show that although it is true that the phenomenon of region-1 current connecting to regions of sunward convecting flux tubes occurs more often on the dusk side than the dawn side, integrated current densities are largest on the dawn side. This qualitatively agrees with the somewhat modest dusk side current strengths seen in the model (see Figures 42 and 45b, for example).

Furthermore, the observations of Table 2 from Iijima and Potemra (1978) report average characteristics of large-scale field-aligned currents. They report an average of ~2.7 MA total region-1 current on both the dawn and dusk sides for active times. Roughly 28% of the total region-1 current is therefore estimated here to be generated (by the mechanism discussed in this thesis) on the dawn side and ~22% on the dusk side. However, this value of ~2.7 MA on each side includes an average estimate of the total dusk side (afternoon to midnight) or total dawn side (midnight to forenoon) region-1 current. The mechanism discussed in this thesis is most important in the local time regions of ~3:00 to 6:00 and ~18:00 to 21:00 (see Figures 42 and 45b, for instance). Typically, data sets do not statistically look in detail at these

regions exclusively. The greatest active time region-1 currents usually occur in the day side regions of ~7:00-8:00 MLT, and ~14:00-15:00 MLT (Iijima and Potemra, 1978).

Although the mechanism discussed here may be the main source of region-1 current flowing on areas of sunward convecting flux tubes in the MLT regions indicated here, it is possible that another generating mechanism exists causing region-1 currents to flow on sunward convecting flux tubes in other local time regions.

IV. DISCUSSION

A. General Comments on Current Systems

In previous chapters the addition of a new current is discussed. This current connects to some of the region-1 FAC, specifically that portion of the region-1 FAC which is on sunward convecting flux tubes. Before outlining the new view of magnetospheric current systems, a discussion of the "traditional" view of magnetosphere-ionosphere current systems is presented. The first part of the discussion in this section follows the approach of Atkinson (1978, 1979).

There are three general categories of large-scale currents in the Earth's magnetosphere and ionosphere which are cross magnetic field current. There are magnetopause currents, ionospheric Pedersen and Hall currents, and currents associated with drift within the magnetosphere and tail. Atkinson identifies seven types of current systems from the three general categories:

(1) The Chapman-Ferraro currents are due to particles of solar wind incident on the magnetopause. The currents close on the surface of the magnetosphere.

(2) Ring current closes exclusively by particle drifts in the magnetosphere.

(3) Divergence-free ionospheric current closes in the ionosphere.

(4) The partial ring current system is composed of drifting

particles in the magnetosphere and closes by region-2 FAC connecting to ionospheric currents.

(5) The "line-tying current" system involves some magnetopause current closing by FAC to the ionosphere. "Line-tying" current connects magnetopause current to ionospheric current via day-side region-1 FAC on antisunward convecting flux tubes.

(6) There exists a system of magnetopause currents which close by particle drifts in the magnetosphere and magnetotail. This is called the magnetotail current system.

(7) The "short-circuited tail current" system involves magnetopause currents, drift currents, FAC, and ionospheric currents.

The "line-tying current" in (5) and the short-circuited tail current in (7) constitute the traditional type region-1 currents.

The observed properties of substorms imply that tail current is diverted along magnetic field lines to the ionosphere. There is a significant redistribution of plasma, with tail current assumed to be due to ion drifts and FAC carried by electrons. The behavior of the coupled ionosphere-magnetosphere system during a substorm can be described by means of an equivalent electric circuit (Boström, 1974). In this substorm current system there is a short circuiting of cross tail current, as described below.

In the expansive phase of a substorm, the tail field lines change from a tail-like to a dipolar configuration (see Section

I.A.3). This a change in field topology. The usual neutral sheet current disappears. The current which enclosed the tail lobe is redirected; it flows along field lines to the ionosphere and closes there forming the westward electrojet (Atkinson, 1979). See Figure 46. The formation of the slot should be equivalent to the addition of an eastward tail current. This eastward tail current, FAC, and auroral electrojets are believed to be the current system responsible for the expansive phase of the substorm. Though the collapse of the tail-like field line to dipolar field lines may start in a limited local time slot, it is probable that this slot configuration spreads both azimuthally and radially during the substorm.

B. Field Aligned and Connecting Currents

This section considers how the current discussed in this dissertation could connect to the generally accepted magnetosphere-ionosphere current systems.

Sonnerup (1980) studied the low-latitude plasma boundary layer. He assumed that the high latitude (region-1) FAC were associated with the boundary layer region, and that region-2 FAC were associated with the region of sunward return flow adjacent to the boundary layer. (This is the conventional view as discussed in Sections I.A.1 and I.A.2.) This boundary layer is supposed to exist over most of the magnetopause surface, with flowing plasma near the boundary layer assumed to be of magnetosheath origin.

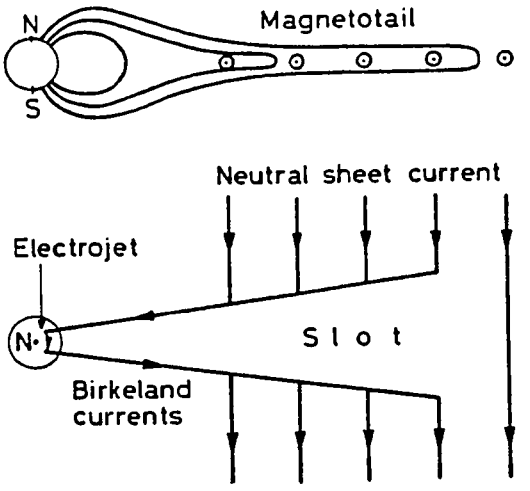

Figure 46. Substorm currents caused by magnetotail current interruption.
Top panel: The sun is to the left. The view is the noon-midnight meridian plane.
Bottom panel: The sun is to the left. The view is looking down on the north geomagnetic pole and equatorial plane. Field-aligned currents and remnants of the "old" neutral current sheet are shown. From Boström, 1974.

Figure 47 is an adaptation of Sonnerup's model. "R2" indicates region-2 current. "R1-A" refers to region-1 current flowing on antisunward convecting flux tubes. "R1-S" refers to region-1 current flowing on sunward convecting flux tubes. "R0" indicates a possible sheet of Birkeland current poleward of region-1 current, and "R3" indicates a possible sheet of Birkeland current equatorward of region-2 current (Doyle et al., 1981). In the equatorial plane, only the component of gradient and curvature current in the dawn-dusk meridian plane is shown. This current component in the $\hat{y}$-direction is shown divided into two parts. The part designated as $\underset{\sim}{j}_{0y}$ is a constant current, which gives $F_x = j_{0y} B$, the sunward directed force, helping to drive the return flow. The currents designated as j_y are nonconstant and close the field aligned currents. This figure shows a possible configuration whereby the "outer $\nabla_e \eta$" current connects to the region-1 current flowing on sunward convecting flux tubes. (This "outer $\nabla_e \eta$" current is also shown in Figure 23 of section II.B.2.)

Recent observations indicate that the convection electric field is generated on closed field lines (Heelis et al., 1980). These closed field lines supposedly connect in the magnetosphere to the low latitude boundary layer. The electric field reversal (and thus the convection reversal) does not define the boundary between open and closed field lines. Although sunward convection is confined to closed field lines, observations indicate that antisunward convection may be associated with closed as well as open field lines (Heelis et al., 1980; Doyle et al., 1981; Bythrow

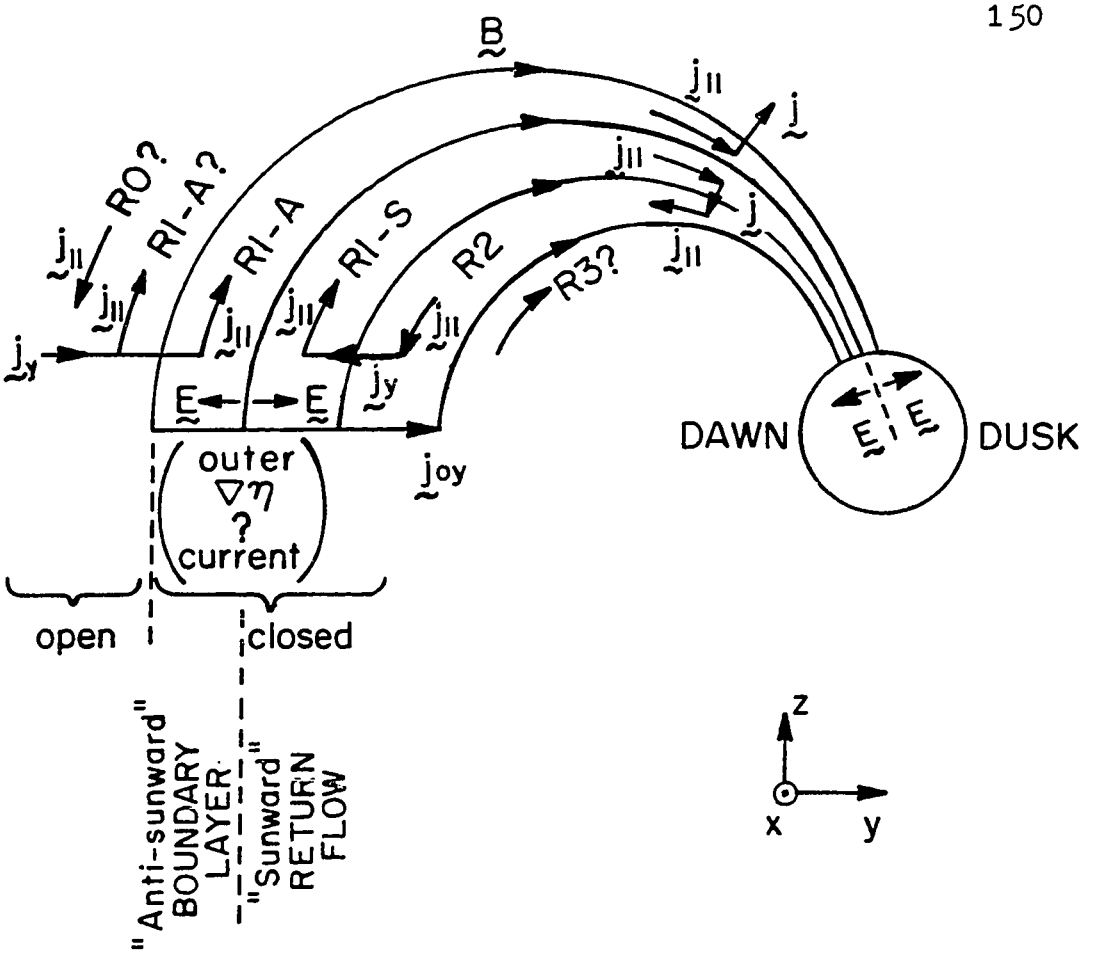

Figure 47. View from the sun of the morningside magnetosphere and its coupling to the ionosphere. The current $\underset{\sim}{j}_{oy}$ remains in the equatorial plane flowing around the magnetosphere as part of the ring current to the evening sector. Notations on figure: A = antisunward, S = sunward, R1 = Region -1 Birkeland current, R2 = Region -2 Birkeland current. RO, R3 are discussed in text. Adapted from Sonnerup (1980).

et al., 1981; Smiddy et al., 1980). Heelis et al. (1980) define two regions of the closed field line region:

1) The Boundary Plasma Sheet (BPS) is characterized by latitudinally structured precipitation. The gross convection reversal occurs in this region.

2) The Central Plasma Sheet (CPS) is a region of relatively uniform morphology.

In the BPS, there is a movement sunward and antisunward. Figure 48, which is a view of the equatorial plane, illustrates these two definitions, along with proposed linkage to field aligned currents for various regions. (This figure does not include region-1 FAC that connects to open field lines.) In Figure 48, the region-1 currents connecting to sunward convecting plasma are of most interest to this dissertation. In this picture, antisunward flow in the ionosphere poleward of the reversal results from a viscously driven convection pattern. According to Heelis et al. (1980), the convection electric field is generated in the low-latitude boundary layer by a viscous interaction between solar wind and magnetospheric plasma. This schematic is not consistent with a completely open magnetosphere. A hybrid magnetosphere is implied (Bythrow et al., 1981). However, Smiddy et al. (1980) question the closed field line boundary layer. Still, Doyle et al. (1981) assume that the single generator for the lowest latitude region-1 FAC and region-2 FAC is to be contained solely in the closed field line portion of the magnetosphere.

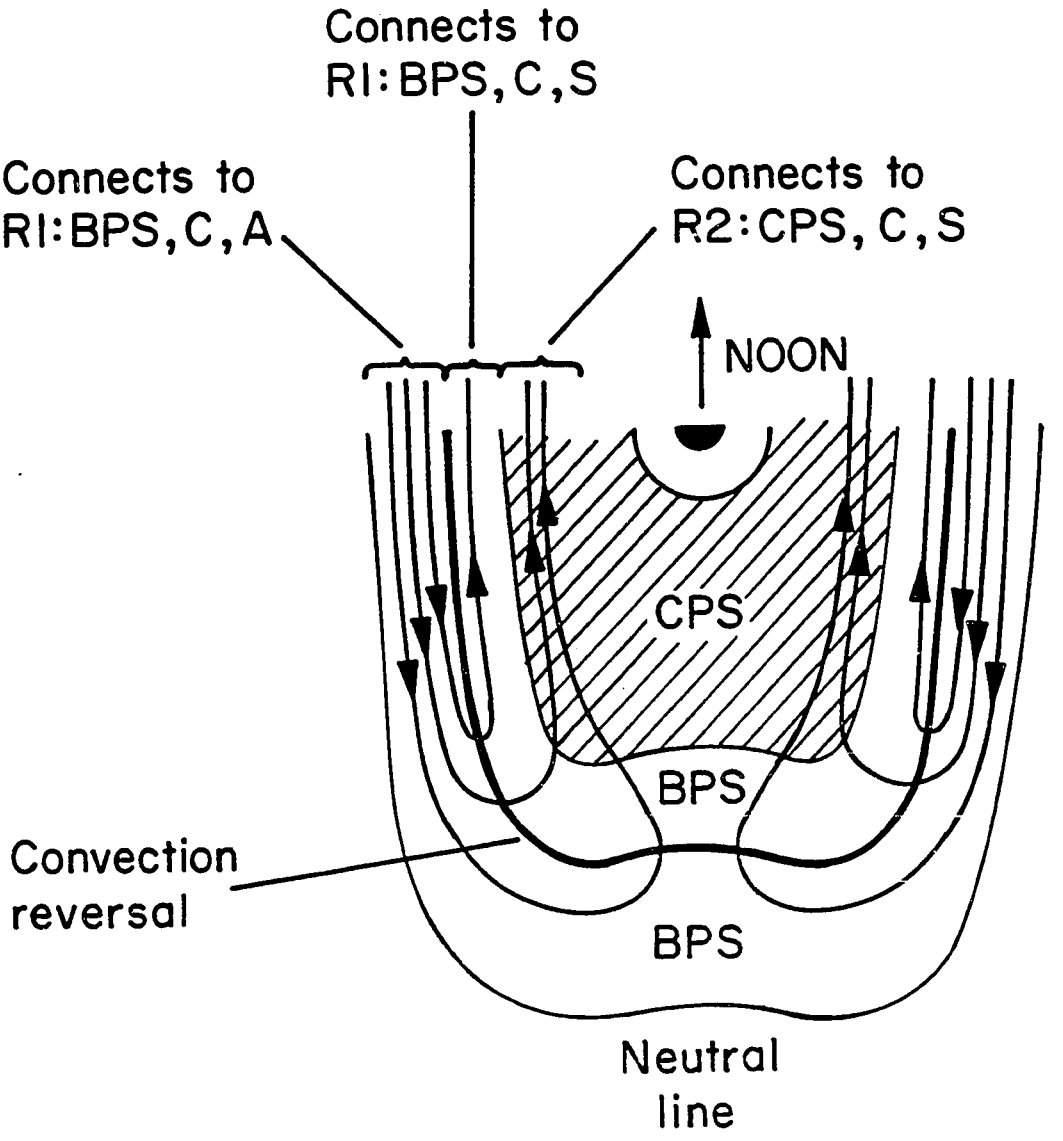

Figure 48. Equatorial plane view. Schematic configuration of magnetospheric particle and flow regions. Notations on figure: C = closed, A = antisunward, S = sunward, BPS = Boundary plasma sheet, CPS = Central plasma sheet, R1 = Region -1 Birkeland current, R2 = Region -2 Birkeland current. Adapted from Heelis et al., 1980.

Chen et al. (1982) discuss a needed change in the traditional view of the substorm two-current loop picture (see Figure 16a of Chen et al., 1982). They conclude that while the traditional tail-current interruption loop is probably correct, a westward partial ring current centered near dusk is not consistent with observed region-2 currents. (The traditional loop is 90° out of phase with observations.) A loop made up of region-1 FAC and region-2 FAC and ring current is shown in Figure 16b of Chen et al. (1981), as a correction to the dusk-centered loop. An adapted form of the figure from Chen et al. is suggested in Figure 49 here.

It should be noted that this a figure illustrating the notions of several endeavors mentioned in this section. It is a supposed configuration combining the two current systems of Figure 16b of Chen et al. (1982) with the "outer $\nabla_e n$ current" discussed in this dissertation. The "outer $\nabla_e n$ current" is probably associated with the cross-tail current interruption discussed in the previous section of this chapter.

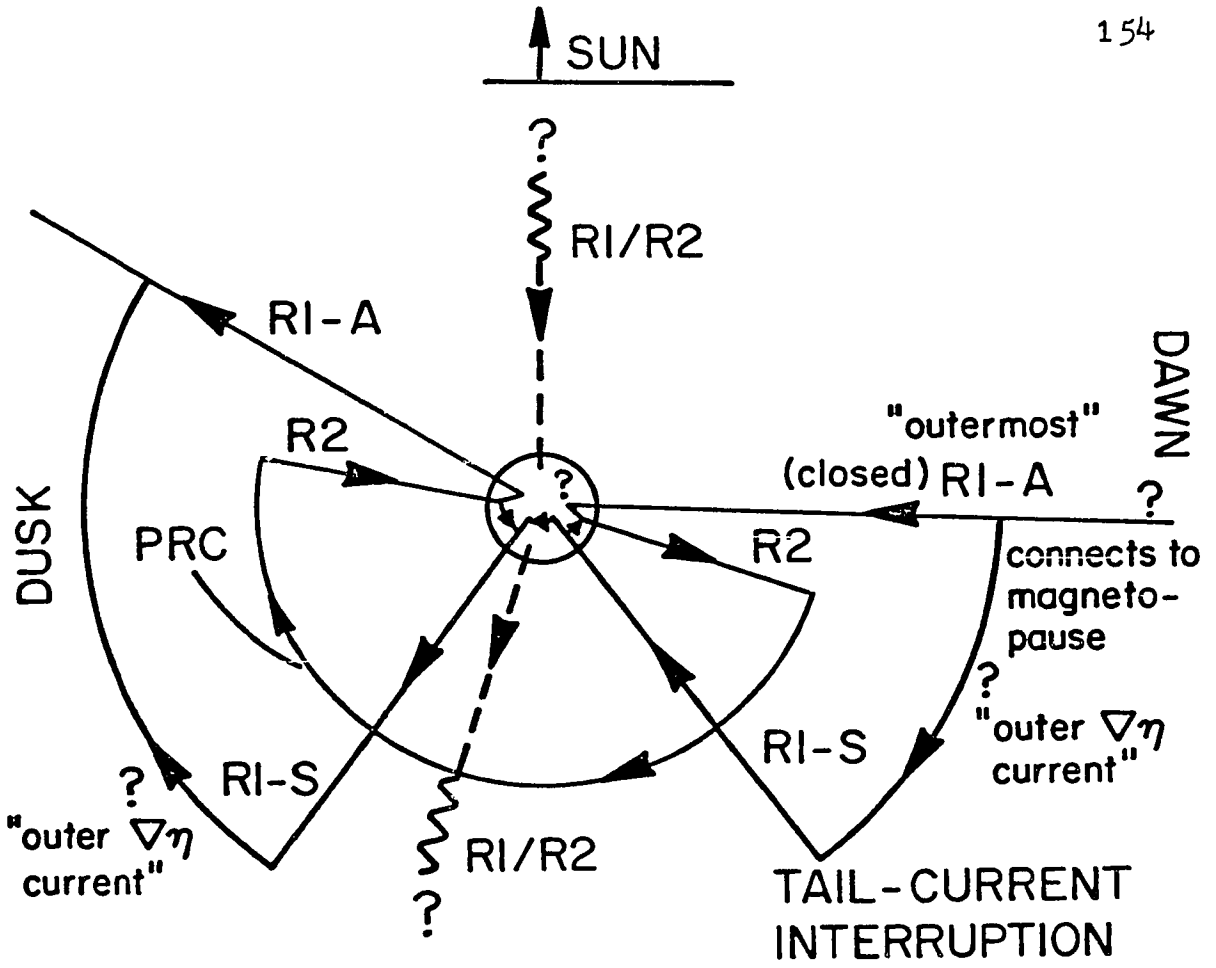

Figure 49. Schematic of current system connecting to open and closed field lines. "R1-A" means Region -1 Birkeland current connecting to antisunward convecting flux tubes. "R1-S" means Region -1 Birkeland current connecting to sunward convecting flux tubes. "R2" is Region -2 Birkeland current connecting to sunward convecting flux tubes. "PRC" is partial ring current. Adapted from Chen et al., 1981.

V. CONCLUSION

A. Summary

The following are conclusions that can be inferred from this work.

1. A configuration in which small flux tubes have higher particle content than large flux tubes tends to be magnetostatically unstable, but can exist stably in the presence of steady convection.

2. A magnetotail channel-like configuration would be stable if it formed.

3. A magnetotail channel-like configuration causes region-1 currents to be generated on sunward convecting flux tubes.

4. There are apparently at least two different types of region-1 Birkeland currents, connecting to phyiscally different regions of the magnetosphere.

5. In S3-3 satellite observations, the generation of region-1 current on sunward convecting flux tubes is most prominent on the dusk side, but the current strength is greatest on the dawn side. The model also predicts greatest current strength on the dawn side.

6. The new model presented here agrees, better than its predecessors did, with the general shape of the magnetic field variations observed by the S3-2 satellite data. This is due to an approximate doubling in the highest ion energy considered and to

consideration of a trapped ring current.

7. Basic results of the model seem insensitive to the specific magnetic field model chosen.

8. Results of the model show that the generated current in the RCM region can account for approximately all the region-1 current on the dawn side and approximately 50% of the region-1 current on the dusk side. A theoretical estimate predicts that an additional 50% of the current generated by the mechanism discussed in this thesis exists outside of the modeling region on the dawn side and an additional 60% exists on the dusk side. The mechanism discussed in this thesis contributes to current in regions of ~18:00 LT to 21:00 LT and ~3:00 LT to 6:00 LT. In other local time regions, it is possible that yet another mechanism exists that causes some region-1 current to flow on sunward convecting flux tubes.

B. New Concepts

The investigation into the nature of region-1 current on sunward flowing flux tubes has led to new concepts and new physics learned about the magnetosphere. Traditional ideas of the magnetosphere may have to be modified to assimilate them with the channel-like region discussed here. The new type of region 1 current generation discussed in the thesis could lead to a new interpretation. It is possible that a substorm is the process which allows plasma-sheet flux tubes in a limited local-time sector

to lose some of their content, becoming depleted. After a substorm expansion phase, plasma could again start to "fill" in the depleted area by injection of ionospheric plasma into the magnetosphere or by convection from the tail. (This could be the recovery phase.) When plasma returns, higher plasma content flux tubes tend to stay further away from the Earth than the lower plasma content flux tubes (as was shown in the bubble analysis). It was shown in Chapter II that a magnetotail channel configuration would be stable. Flows would be greatest in the middle of the tail (Hones et al., 1981). Convected plasma might start "filling" in so rapidly that too many high plasma content flux tubes are getting close to the Earth causing an instability. (This "filling-in time" could be the growth phase.) Then, the area is "swept" by a nonadiabatic release of plasma (Erickson and Wolf, 1980) and a substorm occurs. Onset of the instability could be associated with the onset of the expansive phase. When enough plasma is released from the channel-like region, then the magnetosphere relaxes back to its pre-substorm configuration (i.e., recovery phase). The different amounts of channel depletion at various times could account for the observation that the relative location of most of the region-1 FAC and electric field reversal vary considerably. That is, at times of greater depletion, there may be more region-1 FAC connecting to the sunward convecting region-equatorward of the electric field reversal. Here, the triggering mechanisms for the expansive phase involve some instability relating to the amount of plasma "allowed" in near-Earth flux tubes. The triggering

mechanisms for a substorm are believed to start at ~5 to 20 R_E (McCormac, 1972), but not as far out as 100 R_E. The variable flux tube content "mechanism" would be relevant in the appropriate region.

C. Future Work

This thesis represents a first attempt at understanding the generation of night time region-1 currents on sunward convecting flux tubes. Obviously, more complicated boundary conditions for η should be investigated. Also, on the second generation of runs, a more complicated input conductivity pattern could be used to answer the question: If a midnight-centered channel is depleted at the onset of a substorm, what would happen if the ionospheric conductivity in the same region was enhanced by substorm-associated precipitation? (This would be the feedback system that is discussed by Atkinson (1979).)

With access to better input data (i.e., conductivity, polar boundary potential, plasma sheet energy spectra) and a more elaborate time dependent magnetic field model, this adaptation of the RCM could be improved.

This work has demonstrated that some region-1 Birkeland currents can flow on sunward-convecting non-boundary-layer field lines. At some time in the future, the observed relative locations of FAC and electric field reversal should be monitored so that the time dependence of the depleted magnetotail channel could

be better defined and modeled.

REFERENCES

Akasofu, S.-I., Polar and Magnetospheric Substorms, D. Reidel, Dordrecht, Netherlands, 1968.

Akasofu, S.-I., E. W. Hones, Jr., S. J. Bame, J. R. Asbridge, A. T. Y. Lui, Magnetotail and boundary layer plasmas at a geocentric distance of ~18 R_E: Vela 5 and 6 observations, J. Geophys. Res., 78, 7257, 1973.

Anderson, H. R., and R. R. Vondrak, Observations of currents at auroral latitudes, Rev. Geophys. Space Phys., 13, 243, 1975.

Atkinson, G., Energy flow and closure of current systems in the magnetosphere, J. Geophys. Res., 83, 1089, 1978.

Atkinson, G., The expansive phase of the magnetospheric substorm, in Dynamics of the Magnetosphere, edited by S.-I. Akasofu, p. 461, D. Reidel, Dordrecht, Netherlands, 1979.

Aubry, M. P., A short review of magnetospheric substorms, in Earth's Magnetospheric Processes, edited by B. M. McCormac, p. 357, D. Reidel, Dordrecht, Netherlands, 1972.

Axford, W. I., Magnetospheric convection, Rev. Geophys. Space Phys., 7, 421, 1969.

Axford, W. I., and C. O. Hines, A unifying theory of high-latitude geophysical phenomena and geomagnetic storms, Can. J. Phys., 39, 1433, 1961.

Birkeland, K., The Norwegian Aurora Polaris Expedition 1902-1903; On the Cause of Magnetic Storms and the Origin of Terrestrial Magnetism, Vol. 1, sect. 1 and 2, H. Aschehoug, Christiania,

Norway, 1908.

Boström, R., Currents in the ionosphere and magnetosphere, Ann. Geophys., 24, 681, 1968.

Boström, R., Ionosphere-magnetosphere coupling, in Magnetospheric Physics, edited by B. M. McCormac, p. 45, D. Reidel, Dordrecht, Netherlands, 1974.

Bythrow, P. F., R. A. Heelis, W. B. Hanson, R. A. Power, and R. A. Hoffman, Observational evidence for a boundary layer source of dayside region-1 field-aligned currents, J. Geophys. Res., 86, 5577, 1981.

Cattell, C., R. Lysak, R. B. Torbert, and F. S. Mozer, Observations of differences between regions of current flowing into and out of the ionosphere, Geophys. Res. Lett., 6, 621, 1979.

Chen, C.-K., R. A. Wolf, M.Harel, and J. L. Karty, Theoretical magnetograms based on quantitative simulation of magnetospheric substorm, J. Geophys. Res., 87, 6137, 1982.

Cloutier, P. A., and H. R. Anderson, Observations of Birkeland currents, Space Sci. Rev., 17, 563, 1975.

Cole, K. D., On solar-wind generation of polar geomagnetic disturbance, Geophys. J., 6, 103, 1961.

Doyle, M. A., F. J. Rich, W. J. Burke, and M. Smiddy, Field-aligned currents and electric fields observed in the region of the dayside cusp, J. Geophys. Res., 86, 5656, 1981.

Dungey, J. W., Interplanetary magnetic field and the auroral zones, Phys. Res. Lett., 6, 47, 1961.

Eastman, T. E., E. W. Hones, Jr., S. J. Bame, and J. R. Asbridge,

The magnetospheric boundary layer: Site of plasma, momentum and energy transfer from the magnetosheath into the magnetosphere, Geophys. Res. Lett., 3, 685, 1976.

Erickson, G. M., and R. A. Wolf, Is steady convection possible in the Earth's magnetotail?, Geophys. Res. Lett., 7, 897, 1980.

Frank, L. A., and D. A. Gurnett, Distribution of plasmas and electric fields over the auroral zones and polar caps, J. Geophys. Res., 76, 6829, 1971.

Fukushima, N., Equivalence in ground geomagnetic effect of Chapman-Vestine's and Birkeland-Alfvén's electric current-systems for polar magnetic storms, Rep. Ionos. Space Res. Jap., 23, 219, 1969.

Gurnett, D. A., Satellite measurements of DC electric fields in the ionosphere, in Particles and Fields in the Magnetosphere, edited by B. M. McCormac, p. 239, D. Reidel, Dordrecht, Netherlands, 1970.

Gurnett, D. A., and L. A. Frank, Observed relationships between electric fields and auroral particle precipitation, J. Geophys. Res., 78, 145, 1973.

Gurnett, D. A., and L. A. Frank, Thermal and suprathermal plasma densities in the outer magnetosphere, J. Geophys. Res., 79, 2355, 1974.

Hardy, D. A., P. H. Reiff, and W. J. Burke, Response of magnetotail plasma at lunar distance to changes in the interplanetary magnetic field, the solar wind plasma, and substorm activity, J. Geophys. Res., 84, 1382, 1979.

Harel, M., and R. A. Wolf, Convection, in Physics of Solar-Planetary Environments, Vol. II, edited by D. J. Williams, p. 617, AGU, Washington, D.C., 1976.

Harel, M., R. A. Wolf, P. H. Reiff, R. W. Spiro, W. J. Burke, F. J. Rich, and M. Smiddy, Quantitative simulation of a magnetospheric substorm, 1. Model logic and overview, J. Geophys. Res., 86, 2217, 1981a.

Harel, M., R. A. Wolf, R. W. Spiro, P. H. Reiff, C.-K. Chen, W. J. Burke, F. J. Rich, and M. Smiddy, Quantitative simulation of a magnetospheric substorm, 2. Comparison with observations, J. Geophys. Res., 86, 2242, 1981b.

Heelis, R. A., J. D. Winningham, W. B. Hanson, and J. L. Burch, The relationships between high-latitude convection reversals and the energetic particle morphology observed by Atmospheric Explorer, J. Geophys. Res., 85, 3315, 1980.

Heppner, J. P., Electric field variations during substorms: OGO-6 measurements, Planet. Space Sci., 20, 1475, 1972.

Hones, E. W., Jr., J. R. Asbridge, S. J. Bame, and S. Singer, Energy spectra and distributions of particles in the plasma sheet and their comparison with rocket measurements over the auroral zone, J. Geophys. Res., 76, 63, 1971.

Hones, E. W., Jr., J. R. Asbridge, S. J. Bame, M. D. Montgomery, S. Singer, and S.-I. Akasofu, Measurements of magnetotail plasma flow made with Vela 4B, J. Geophys. Res., 77, 5503, 1972.

Hones, E. W., Jr., S. J. Bame, and J. R. Asbridge, Proton flow

measurements in the magnetotail plasma sheet made with Imp 6, J. Geophys. Res., 81, 227, 1976.

Hones, E. W., Jr., J. Birn, S. J. Bame, J. R. Asbridge, G. Paschmann, N. Sckopke, and G. Haerendel, Further determination of the characteristics of magnetospheric plasma vortices with ISEE 1 and 2, J. Geophys. Res., 86, 814, 1981.

Iijima, T., and T. A. Potemra, Large-scale characteristics of field-aligned currents associated with substorms, J. Geophys. Res., 83, 599, 1978.

Jaggi, R. K., and R. A. Wolf, Self-consistent calculation of the motion of a sheet of ions in the magnetosphere, J. Geophys. Res., 78, 2852, 1973.

Karty, J. L., The interaction of horizontal ionospheric and region one Birkeland currents, M.S. thesis, Rice University, Houston, TX, 1981.

Karty, J. L., C.-K. Chen, R. A. Wolf, M. Harel, and R. W. Spiro, Modeling of high-latitude currents in a substorm, J. Geophys. Res., 87, 777, 1982.

Krall, N. A., and A. W. Trivelpiece, Principles of Plasma Physics, p. 251, McGraw-Hill, New York, 1973.

McCormac, B. M., Summary and conclusions, in Earth's Magnetospheric Processes, edited by B. M. McCormac, p. 409, D. Reidel, Dordrecht, Netherlands, 1972.

Mozer, F. S., C. A. Cattell, M. Temerin, R. B. Torbert, S. Von Glinski, M. Woldroff, and J. Wygant, The dc and ac electric field, plasma density, plasma temperature, and field-aligned

current experiments on the S3-3 satellite, J. Geophys. Res., 84, 5875, 1979.

Mozer, F. S., C. A. Cattell, M. K. Hudson, R. L. Lysak, M. Temerin, and R. B. Torbert, Satellite measurements and theories of low altitude auroral particle acceleration, Space Sci. Rev., 27, 155, 1980.

Nishida, A., Geomagnetic Diagnosis of the Magnetosphere, Springer-Verlag, New York, 1978.

Richmond, A. D., Self induced motions of thermal plasma in the magnetosphere and the stability of the plasmapause, Radio Sci., 8, 1019, 1973.

Rishbeth, H., and O. K. Garriott, Introduction to Ionospheric Physics, Academic Press, New York, 1969.

Shuman, B. M., R. P. Vancour, M. Smiddy, N. A. Saflekos, and F. J. Rich, Field-aligned current, convective electric field, and auroral particle measurements during a major magnetic storm, J. Geophys. Res., 86, 5561, 1981.

Smiddy, M., W. J. Burke, M. C. Kelley, N. A. Saflekos, M. S. Gussenhoven, D. A. Hardy, and F. J. Rich, Effects of high-latitude conductivity on observed convection electric fields and Birkeland currents, J. Geophys. Res., 85, 6811, 1980.

Sonnerup, B. U. O., Theory of low-latitude boundary layer , J. Geophys. Res., 85, 2017, 1980.

Spiro, R. W., M. Harel, R. A. Wolf, and P. H. Reiff, Quantitative simulation of a magnetospheric substorm, 3. Plasmaspheric electric fields and evolution of the plasmapause, J. Geophys.

Res., 86, 2261, 1981.

Stern, D. P., Large-scale electric fields in the Earth's magnetosphere, Rev. Geophys. Space Phys., 15, 156, 1977.

Stern, D. P., XXIV Cospar abstract, from 24th "Plenary Meeting" (Committee on Space Research), STP III, 3.13, p. 37, 1982.

Swift, Daniel W., The possible relationship between the auroral breakup and the interchange instability of the ring current, Planet. Space Sci., 15, 1225, 1967.

Voigt, G.-H., A mathematical magnetospheric field model with independent physical parameters, Planet. Space Sci., 29, 1, 1981.

Wolf, R. A., The quasi-static (slow-flow) region of the magnetosphere, lecture presented at the Solar-Terrestrial Theory Institute, Boston College, August, 1982, to be published, 1983.

Wolf, R. A., and R. W. Spiro, The role of the auroral ionosphere in magnetospheric substorms, to be published in proceedings of Nobel Symposium No. 54, Problems in High Latitude Magnetospheric/Ionospheric Plasma Physics and Strategies for their Solution, Kiruna, Sweden, March, 1982.

Wolf, R. A., M. Harel, R. W. Spiro, G.-H. Voigt, P. H. Reiff, and C.-K. Chen, Computer simulation of inner magnetospheric dynamics for the magnetic storm of July 29, 1977, J. Geophys. Res., 87, 5949, 1982.

Zmuda, A. J., and J. C. Armstrong, The diurnal flow pattern of field-aligned currents, J. Geophys. Res., 79, 4611, 1974a.

Zmuda, A. J., and J. C. Armstrong, The diurnal variation of the

region with vector magnetic field charges associated with field-aligned currents, J. Geophys. Res., 79, 2501, 1974b.

Zmuda, A. J., J. H. Martin, and F. T. Heuring, Transverse magnetic disturbances at 1100 kilometers in the auroral region, J. Geophys. Res., 71, 5033, 1966.